Generative Design Procedure for Embedding Complex Behaviour in Pneumatic Soft Robots

by

David Rostin Ellis

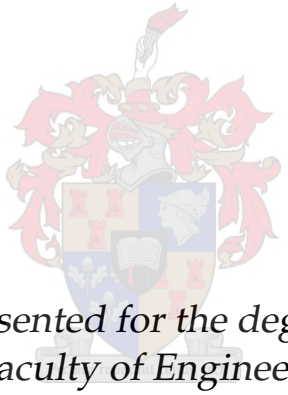

Dissertation presented for the degree of Doctor of Philosophy in the Faculty of Engineering at Stellenbosch University

Supervisors: Dr M.P. Venter
Prof G. Venter

March 2020

Declaration

By submitting this dissertation electronically, I declare that the entirety of the work contained therein is my own, original work, that I am the sole author thereof (save to the extent explicitly otherwise stated), that reproduction and publication thereof by Stellenbosch University will not infringe any third party rights and that I have not previously in its entirety or in part submitted it for obtaining any qualification.

This dissertation includes two original papers published in peer-reviewed conference proceedings. The development and writing of the papers (published and unpublished) were the principle responsibility of myself and, for each of the cases where this is not the case, a declaration is included in the dissertation indicating the nature and extent of the contribution of co-authors.

Date: March 2020 .....

Abstract

Generative Design Procedure for Embedding Complex Behaviour in Pneumatic Soft Robots

D.R. Ellis

Dissertation: PhD (Mech)

March 2020

Soft pneumatic actuators form part of the growing field of soft robots being used in areas not suited to conventional hard-linked robots. Applications include low-cost automation, wearable technology, and the handling of easily damaged produce/goods. Typically these actuators are manufactured as cast silicone bodies and are powered by compressed air. This research set out to develop methods whereby these actuators can be designed to best represent a desired behaviour and behavioural responses not previously possible.

A bimodal actuator was developed where the bending direction can be altered by changes to the internal pressure. This allows non-trivial behaviour whilst using a single pressure source. A layer of a specially developed bilinear material facilitates this response. This bilinear material utilises a strain limiter crimped to an initial condition. As the paper layer decrimps, the response becomes stiffer and approximates that of the reinforcing paper layer. This change in stiffness allows for the preferential bending direction of the actuator to change.

An additional stream of research focused on a modular actuator construction made up of smaller articulating units in series. These units are constructed to have a preferential bending direction. By changing the orientation of each unit, a different deformed actuator shape can be made. A

design tool was developed where a genetic algorithm was coupled with a nonlinear finite element solver. This design tool optimises the design using the genetic information available in the initial population over multiple generations and presents a candidate that best resembles a desired profile specified as the objective function. A 2D reduced-order model was developed that reduces the time for each function evaluation from ≈ 20 min for a 3D numerical analysis, to ≈ 45 s. The design tool was tasked to solve design targets ranging from sin and cos functions of various amplitudes to final actuator tip positions. In each case, the inflated actuator resembled the desired profile.

Five of these designs were manufactured using an aluminium mould with ± 0.02 mm tolerances. The inflated actuators were 3D scanned and qualitatively compared to their numerical counterparts. The overall deformation shape of the physical models closely resembled that of the numerical models.

Uittreksel

Generatiewe Ontwerpprosedure om Komplekse Gedrag in Pneumatiese Sagte Robotte te Voeg

D.R. Ellis

Proefskrif: PhD (Meg)

Maart 2020

Sagte pneumatiese aktueerders vorm deel van die groeiende veld van sagte robotika wat gebruik word in gebiede wat nie geskik is vir konvensionele hardkoppelde robotte nie. Toepassings sluit in laekoste-outomatisering, drabare tegnologie en die hantering van maklik beskadigde gewasse/goedere. Tipies word hierdie aktueerders vervaardig as gegote silikoonliggame en word aangedryf deur saamgeperste lug. Hierdie navorsing is gemik daarop om metodes te ontwikkel waarmee hierdie aktueerders ontwerp kan word om gewenste gedrag te verteenwoordig sowel as gedrag wat nie voorheen moontlik was nie te behaal.

'n Bimodale aktueerder was ontwikkel waar die buigrigting verander kan word deur veranderinge aan die interne druk. Dit laat nie-triviale gedrag toe terwyl 'n enkele lugdrukbron gebruik word. 'n Spesiaal ontwikkelde bilineêre materiaal vergemaklik hierdie gedrag. Hierdie bilineêre materiaal maak gebruik van 'n vervormingsbeperker wat na 'n aanvanklike toestand gekrimp is. Soos die materiaal belas word en vervorm, neem die krimp in the papierlaag af en word die algehele respons van die materiaal stywer. Hierdie verandering in styfheid laat die voorkeurbuigrigting van die aktueerder verander.

'n Bykomende stroom navorsing het gefokus op 'n modulêre aktueerderkonstruksie wat bestaan uit kleiner eenhede gekoppel in serie. Hierdie een-

hede is ontwerp om ’n voorkeurbuigrigting te hê. Deur die oriëntasie van elke eenheid te verander, kan ’n verskillende vervormde aktueerdervorm gemaak word. ’n Ontwerpinstrument was ontwikkel waar ’n genetiese algoritme gekoppel word aan ’n nie-lineêre eindige elementoplosser. Hierdie ontwerpinstrument optimeer die ontwerp deur gebruik te maak van genetiese inligting wat beskikbaar is in die aanvanklike bevolking oor verskeie generasies en bied ’n kandidaat aan wat die beste ooreenstem met ’n gewenste profiel wat as die objektiewe funksie gespesifiseer is. ’n Verminderde-orde 2D-model is ontwikkel wat die tyd vir elke funksie evaluasie van $\approx$ 20 min vir ’n 3D-numeriese analise, tot $\approx$ 45 s verminder. Die ontwerpinstrument het die opdrag gehad om ontwerpteikens op te los, wat wissel van sin- en cos-funksies van verskillende amplitudes tot finale aktueerderpuntposisies. In alle gevalle het die aktueerder gelyk soos die gewenste profiel.

Vyf van hierdie ontwerpe was geproduseer met behulp van ’n aluminiumvorm wat vervaardig was met ± 0.02 mm toleransies. Die werkende aktueerders, opgepomp tot die benodigde druk, is geskandeer om ’n 3D model van die fisiese part te skep. Hierdie 3D model was kwalitatief vergelyk met hul numeriese eweknie. Die algehele vervormingsvorm van die fisiese modelle het baie soos die numeriese modelle gelyk.

Acknowledgements

The following people and organisations played a large role in this project:

Andre and Dianne

Michael and Sonja

Jannie, Una, Digby, and Tammy

Gerhard and Martin

CSIR and the Department of Mechanical and Mechatronic Engineering for their funding.

Staff in the departmental workshop, most notably Anton, for the meticulous detail in manufacturing my parts.

Technical support engineers at Esteq and Simteq, specifically Gerrit Visser for MSC Marc and Juan Coetzer for Siemens NX.

Off-road motorcycles for shaping my life and persistently occupying my mind from before I even started school.

Table of Contents

List of Figures

List of Tables

Chapter 1

Introduction and Project Outline

1.1 Background of Soft Robotics

Soft robots are fundamentally different from their more traditional, hard-linked namesakes (Trivedi *et al.*, 2008) and cannot necessarily build upon the knowledge gathered from traditional robot design (Laschi and Cianchetti, 2014). Where traditional robots excel at working in well defined, structured workspaces with every precision move manipulated from a central control system, the control of soft robots can rather be reduced to a simpler means (Mosadegh *et al.*, 2014) to yield actuators better suited to unstructured environments (Martinez *et al.*, 2013). This reduced control requirement stems from a reduction in the compliance of the topology leading to a system that is more tolerant of small deviations. Deformation behaviour can therefore be pre-programmed into the morphological architecture of the actuator during design as a limited substitute for a central control system. Some of the control loops are thereby substituted for by the soft materials (Yang *et al.*, 2016) and the mechanical passive dynamics of the actuators are then utilized to achieve the desired behaviours (Iida and Laschi, 2011).

The desire to automate tasks for increased flexibility and adaptability has led the way for the creation of aptly named soft robots. Applications that require, for example, low cost expendable hardware for use in risky situations, compliance that matches that of a human workforce for safe real-time human-machine collaboration, or simplified control systems whilst maintaining flexibility in its use are ideally suited to soft robot technology. These soft actuators are designed to perform tasks whilst receiving simple

inputs; their behaviour effectively being pre-programmed into their morphology. To date, this design process has largely been dictated by the physical inputs of their designers. Tools that aid this process have been empirical experimentation, deducing analytical equations that describe the motion of previously conceived morphologies, and the use of numerical tools in finite element (FE) analyses to investigate behaviour and performance of untested designs. The relatively unconstrained fabrication methods and use of multiple materials and material distributions result in a vast design space that is difficult to rapidly explore by means of such traditional and trial-and-error design paradigms (Hiller and Lipson, 2012*a*).

Generative design is loosely defined as a design exploration process resulting in a number of outputs that meet certain constraints. Generative design methods of automating the design process by evolving and optimising designs over many generations have been proposed and presented. As of yet, these have enjoyed limited exploration in comparison to the manual design methods. Further, existing research into such generative design processes has focussed on volumetrically actuated materials (materials that react to external pressure changes) and have avoided morphologies with internally distributed voids for pressurisation means. To realise the potential that can be achieved by embedding behaviour into the design of actuators it is necessary to further investigate and develop new materials and evolutionary-inspired design processes.

1.2 Motivations

Soft robots have shown potential to be used in applications where hard-linked robots are either unsuited or too complex for their use to be justified. By further investigating new composite materials and processes whereby these robots are designed for, specific behaviour could ultimately be beneficial to the field. Research into the use of an evolutionary design procedure to generate candidates for internally pressurised soft pneumatic actuators has not been undertaken to date. The specific research objectives are pursued to lay a foundation for generating non-trivial behaviour in these actuators. A design methodology could assist with the development of soft robotic grippers for the handling of delicate goods and produce, or wearable devices for

assisted living or rehabilitation that are both cost effective and best suited to the intended application.

1.3 Research Question and Objectives

The overarching research question that will be addressed in this dissertation can be stated as:

To what extent can specified, predictable, or non-trivial behaviour be incorporated and pre-programmed in soft pneumatic actuators?

This research question is formulated as three objectives:

1. Develop a soft pneumatic actuator (SPA) capable of changeable bi-modal behaviour driven by a linear pressure source.
2. Develop a SPA of modular construction comprising individual articulating units, or building blocks, of pneumatically actuated soft materials that can be connected in series to form an actuator.
3. Develop a computationally efficient process that can determine the modular candidate actuator that best matches a given desired inflated profile.

1.4 Project Scope

The project scope attempts to set restrictions on the research performed to remain aligned with the overarching research question.

1. Design an actuator that can sustain a 270° – 360° bending shape when all articulating units are aligned in the same direction without rupturing. The specific articulating unit and series quantity that facilitate this will then form the backbone of the research. The aim is not to perform an exhaustive study that investigates units with varying parameters and the designs that can be achieved with them.
2. The performance of the design algorithm must be established for a variety of different design targets. Application specific problems will not be investigated.

3. The design algorithm must easily be adaptable for varying materials, articulating unit dimensions, and unit quantities. The development of multiple different units will not be undertaken.

1.5 Outline

Chapter 2 provides a literature review of current methods used for designing pneumatic soft actuators. Sections of Chapter 3 are based on a conference paper and details a predictable and tunable bilinear composite material that was developed using numerical tools for use in SPAs and provides an application for this composite during the development of bimodal actuators. Chapter 4 describes the automated design procedure as well as the construction of the modular SPA. A reduced-order modelling technique that reduces a full 3D model to a representative 2D case is provided in Chapter 5. Chapters 4 and 5 include work originally published as a conference paper. Chapter 6 covers the performance of the design procedure when tasked to solve different design objectives and finds a correlation between physical and numerical models. The project is concluded in Chapter 7 and recommendations for future work are made in Chapter 8.

Chapter 2

Silicone Rubber and Exploring Design Spaces in Soft Robotics

Soft pneumatic actuators (SPAs) are of interest in several fields from medicine (Polygerinos *et al.*, 2013; Yap *et al.*, 2015; De Greef *et al.*, 2009) and manufacturing (Shintake *et al.*, 2016; Deimel and Brock, 2013) to potential applications in search and rescue (Füchslin *et al.*, 2013; Moseley *et al.*, 2016; Rus and Tolley, 2015). These devices have a more organic actuation than conventional rigid, hinged actuators making them potentially more suitable for human-robot interfaces (Yang *et al.*, 2015; Landkammer *et al.*, 2016). Additional advantages include low weight, efficient use of materials and an inherent compliance that is highly desirable when designing for cases with unpredictable loading (Moseley *et al.*, 2016; Shepherd *et al.*, 2013; Nishioka *et al.*, 2012). This chapter focuses on the materials and methods typically used with soft pneumatic actuators (SPAs).

2.1 Overview of Silicone Rubber

A study pertaining to the design of SPAs requires that a description of the building material thereof be supplied. The integral part that the material forms in the behaviour of each actuator demands that it be understood sufficiently. Curing parameters that affect final material properties need to be known for consistent manufacturing results. The expected stress-strain response must be grasped and represented in mathematical material modelling. The elastomer silicone rubber has proven to be the best suited,

most widely used soft material in this field and is available over a large range of stiffnesses. This research uses three readily available silicones that cover a range of different stiffness values: the Smooth-On (2019) products Ecoflex 0030, Mold Star 15, and Smooth-Sil 950. These silicones have been used extensively in soft robotic literature (Case *et al.*, 2015; Elsayed *et al.*, 2014; Moseley *et al.*, 2016; Martinez *et al.*, 2012; Paez *et al.*, 2016; Deimel and Brock, 2013; Agarwal *et al.*, 2016; Ilievski *et al.*, 2011; Shepherd *et al.*, 2011; Marchese *et al.*, 2014). This section introduces the material and covers the testing and characterisation processes followed. Reliable material response data was not available for these materials and required that experimental characterisation be done.

Soft actuators are required to undergo repeated large elastic deformations when pressurised and de-pressurised while performing tasks. In addition, the intricate shapes often required for the desired actuation must be achievable. Few materials are suited to such loading conditions without showing material degradation or immediate failure.

2.1.1 Characteristics

Silicone rubber has properties ideally suited to soft actuators. Being a polymer consisting of predominately silicone along with hydrogen, carbon and oxygen it is intrinsically soft and deformable. Characteristics further extend to high temperature resistance, being inert with most chemicals as well as being hydrophobic. This inert characteristic is exploited for medical applications. One of the few materials that silicone can reliably adhere to is itself; this trait is often exploited in mould making and casting procedures.

Figure 2.1 shows the Young's modulus of these silicones in comparison to other widely known materials. In its uncured state it resembles a gel-like substance with high adhesion characteristics. This viscous fluid can be cast into intricate moulds when done under vacuum.

Silicone-rubber typically has an isotropic, nonlinear, hyperelastic response to tensile loading with negligible visco-elasticity and hysteresis (Meunier *et al.*, 2008). Rey *et al.* (2014) investigated the effect of temperature on the mechanical response of silicones and found an appreciable change in stiffness as temperature was varied from -60°C to 150°C. Interpolating their

presented data over a range of 10°C around room temperature the effect becomes insignificant.

Hardness of polymers, elastomers, and rubbers is measured using the Shore durometer in Shore hardness. This test caters for twelve different scales and follows the same methodology as many other hardness testers; the indentation depth is measured on a sample using a prescribed force and standardised presser foot geometry. Durometer is a dimensionless quantity and as such no relationship exists between the materials' hardness in different scales. The silicones typically used in soft robotics research vary in Shore Hardness from 10 on the 00-scale to 50 on the A-scale (Ecoflex 0010 to Smooth-Sil 950 (Smooth-On, 2019)) and are available as two-part mixtures. Figure 2.2 shows the Shore hardness of various objects on different scales.

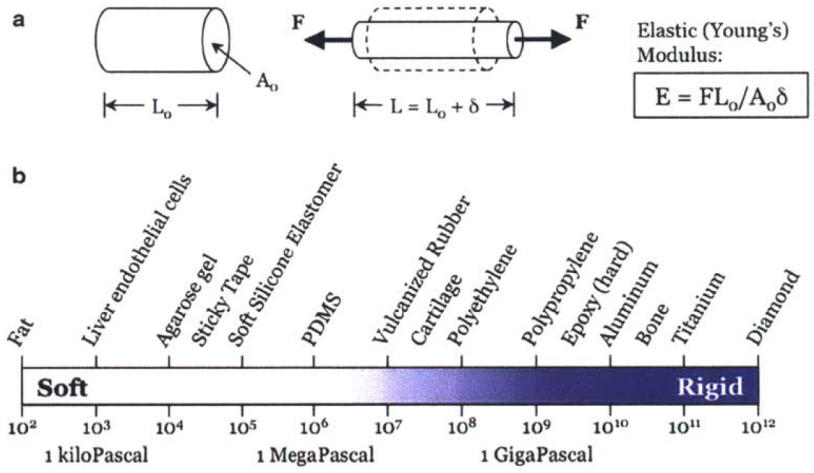

Figure 2.1: Young's modulus for various materials (Majidi, 2014)

2.1.2 Curing

In order to solidify, the uncured silicone must undergo a non-reversible curing, catalisation or vulcanisation process depending on the specific material. The material used in soft robotic research is primarily a platinum cure based silicone-rubber.

The platinum curing process commences when the two-part solution that constitutes the material is mixed together. As per ASTM the gel time,

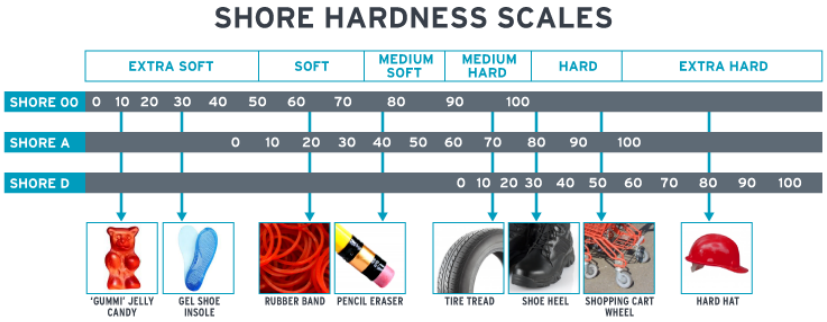

Figure 2.2: Shore hardness for various scales and objects showing the relative hardness to each other (Seals Unlimited, 2019)

also referred to as the pot-life, is the time available before curing has progressed sufficiently for solidification to hamper easy pouring and casting. As an indication, the pot-life for Ecoflex 0030 is 45 min. This can be extended to in excess of 120 min by using Smooth-On Slo-Jo (2019) specifically for platinum cured silicones which allows for increased preparation whilst busy with the casting process. This cure retarder does however affect the final material properties. Further, platinum cured silicones are the only branch of silicones where the cure time can be decreased by either increased pressure or temperature. Cure temperature does however largely affect final material stiffness of these materials (Johnston *et al.*, 2014) and should therefore not be varied between different manufactured batches.

The introduction of air bubbles during mixing and the high viscosity of the prepolymer will lead to large voids and inconsistent casting results. To circumvent this issue the thoroughly mixed prepolymer must be degassed in the mixing cup. This degassed pre-polymer can then be poured into the mould where an additional degassing step is required. This additional step aids in drastically reducing the void percentage and facilitates the removal of the trapped air bubbles in the various features of the mould.

2.2 Preface to Design Methodologies

Research to date has used an assortment of techniques and methodologies for the design of soft robots, covered in further detail throughout this chapter. These designs have mainly been used to demonstrate the novelty of the field as well as showcase applications where traditional hard-linked robots

cannot be utilised without a high degree of complexity in their design and control. The methodologies pertaining to the design phase of these actuators remain a source for further advancement in the field.

Functionality of these soft robots can be pre-programmed into their morphology by essentially embedding behaviour into the architecture of the body that manifests as mechanics under controlled loading. Designing soft robots thus requires methodologies that cannot be sourced from those already devised for hard-linked robots. Robust design methodologies for soft robots will allow research focus to shift from manual design approaches to those that facilitate the development of actuators that utilise the entire available design space. Such designs will exhibit complex locomotion and articulation paths, morphologies better suited to soft materials and improved repeatability amongst samples whilst maintaining simplicity in their means of actuation through simple fluidic pressure changes.

A non-technical review of the field was performed by Shen (2016) and detailed investigations are presented by Wang *et al.* (2015), Marchese *et al.* (2015), Rus and Tolley (2015), Manti *et al.* (2016) and Lee *et al.* (2017). The present work provides a broad review of the current state-of-the-art in soft robotic design methodologies. The various design methodologies followed to date are classified into three main categories according to the approach taken and technology used. Each methodology is substantiated by means of examples and the benefits and drawbacks are discussed.

The three widely used actuation means for soft robots were identified by Lee *et al.* (2017) as variable length tendons, fluidic actuation, and electroactive polymers (EAP). This review article is directed at fluidic actuation of soft robots. Fluidic actuation includes soft pneumatic actuators (SPAs), Figure 2.3a, and fibre reinforced elastomeric enclosures (FREEs and PneuFlex (Deimel and Brock, 2013)), Figure 2.3b. Continuum actuators, which are manipulated by rigged-assistance such as cables or wires, are excluded.

2.3 Existing Design Methodologies

Researchers from different groups have approached the soft robotic design problem with different tools. Consequently, different methodologies have been developed which enable the investigation into what each one has to

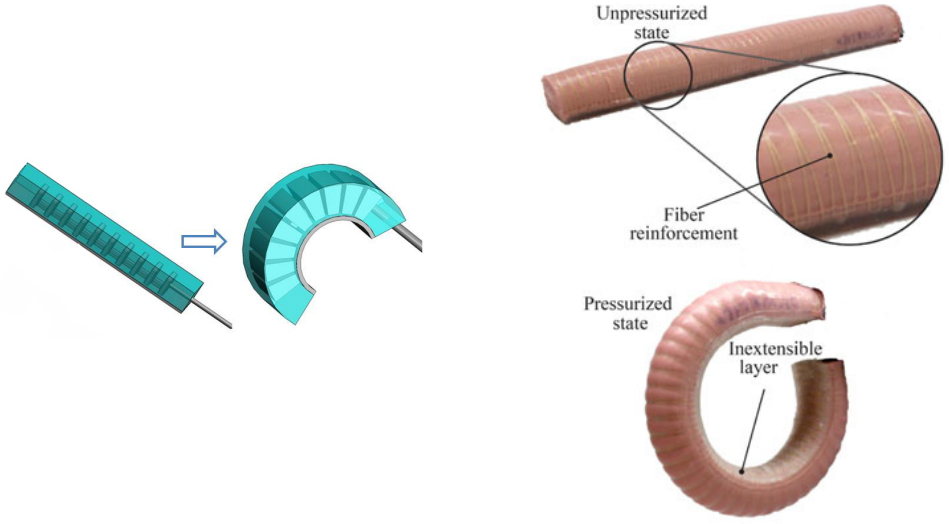

(a) Soft pneumatic actuator (SPA) shown in the unpressurised (left) and pressurised (right) states (Sun *et al.*, 2013)

(b) Fibre-reinforced elastomeric enclosure (FREE) shown in the unpressurised (top) and pressurised (bottom) states (Polygerinos *et al.*, 2015)

Figure 2.3: Two different configurations of soft pneumatic actuators

offer. These methodologies include outcomes-based trial-and-error empirical approaches (that either require the manufacturing of multiple physical robots or the investigation into the results of numerical simulations), and deductions of analytical relationships from first principles.

Final detail design of these moulds is done using computer aided design (CAD) software (Rus and Tolley, 2015). Soft robots are typically manufactured by casting silicone prepolymer into moulds created by 3D printing, or similar technology. Current literature shows that the various design methodologies explored thus far each has a distinct characteristic. These characteristics, as well as their pros and cons, are discussed next.

2.3.1 Empirical Design Methodologies

The empirical design methodology is an approach where conclusions are drawn from either physical or numerical experimentation and then used to improve subsequent iterations. It does not allow for deterministic design. The performance of actuators can only be established once manufactured or modelled. This approach has proven ideal for demonstrating the capabilities of soft actuators and conceiving practical designs. Initial work done

in the field was exploratory and pioneering in nature. The empirical approach allows for the extrapolation of knowledge gathered from various fields in a rapid manner. The appropriateness of a design can be evaluated through experimentation, before spending time devising intricate mathematical models to aid in the rest of the design process.

Physical Experimentation Based

The Whitesides group contributed largely to the empirical methodology through experimentation (Ilievski *et al.*, 2011). They covered a wide range of applications, amongst those being robots powered by explosions (Shepherd *et al.*, 2013), those with the ability to walk whilst tethered (Shepherd *et al.*, 2011) (Figure 2.4) and untethered (Tolley *et al.*, 2014*a*), tentacles with three-dimensional mobility for use with various tips such as needles and cameras (Tolley *et al.*, 2014*b*), camouflage capabilities that can change in the visible and infrared ranges (Morin *et al.*, 2012), modular magnetic assemblies to hold soft actuators in place (Kwok *et al.*, 2014), and origami reinforced actuators (Martinez *et al.*, 2012). They further investigated methods of simplifying and speeding up fabrication by using modular assemblies of clickable silicone bricks (Morin *et al.*, 2014*a*) and soft jointed tiles (Morin *et al.*, 2014*b*) that offer fast turn-around times for subsequent iterative designs. Inspiration into these modular arrangements of soft actuators further led to mimicking the sailing motion of snakes and creating a soft mobile rolling robot (Onal and Rus, 2012; Onal *et al.*, 2011).

The group makes use of an iterative approach that relies on an initial general insight followed by incremental design improvements based on observation. For example, the actuation speeds of pneumatic networks of small channels (Pneu-nets) resembling finger-like actuators were improved (Mosadegh *et al.*, 2014) using this approach, Figure 2.5a. The improved actuation speed was demonstrated by using the finger-like actuators to play musical melodies on a piano.

Similar finger-like bending actuators with mechanically programmable bending characteristics were constructed using either a rigid sleeve that constricts the actuator around its circumference or with fibre-reinforced laminates that selectively restrict bending (Galloway *et al.*, 2013). The fit of this sleeve is such that it can rapidly be adjusted to better suit the immediate ap-

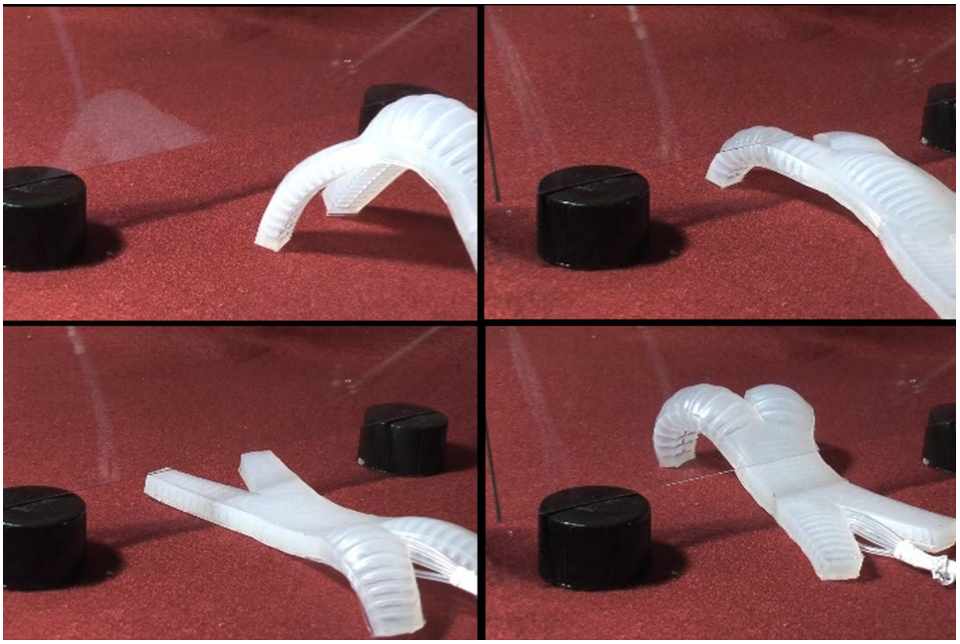

Figure 2.4: Multigait soft robot demonstrating its ability to crawl underneath obstacles whilst tethered (Shepherd *et al.*, 2011)

plication of the actuator where it is not known a priori, Figure 2.5b. Further designs of bending and rotary actuators were experimentally characterized for varying wall-thickness. The results of this research were published as guidelines for further design iterations (Sun *et al.*, 2013).

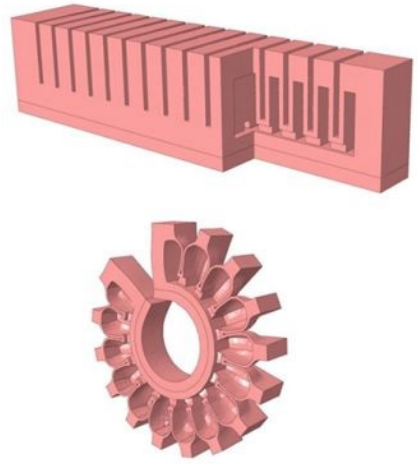

(a) Fast Pneu-net designed using an empirical approach for improved actuation speed (Mosadegh *et al.*, 2014)

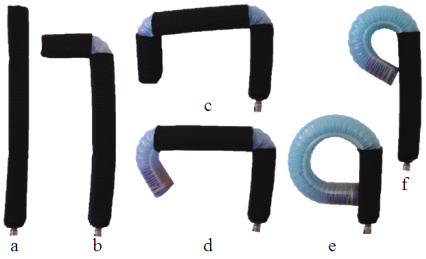

(b) An adjustable rigid sleeve that can be used to alter the range of motion of a FREE (Galloway *et al.*, 2013)

Figure 2.5: Different SPA constructions

Numerical Simulation Based

It is proposed that numerical work, in the context of empirical design methodologies, is classified as research being conducted where numerical simulations performed on solid bodies precede the manufacturing of the actuators. This process can be classified as numerical experimentation (as compared to physical experimentation). These simulations are typically performed using finite element (FE) analyses and allow designers to test prototypes for functionality before manufacturing. Setting up such simulations can be time consuming and computationally intensive, but they can yield detailed results. These results offer insight into the mechanics of the design by visualising deformation and stress states. As an explicit relationship between inputs and outputs does not exist (as is the case for analytical models), researchers require a high degree of familiarity with the numerical process in order to set up models that will yield reasonable results. Numerical simulation tools have the benefit that designs can be modelled and optimized before manufacturing and are not constrained by the conditions that bound explicit analytical relationships. Complex material models and geometries can be modelled in detail and with relative ease. These tools provide an important intermediary step to advance from manual empirical research to a methodology that utilises computational power to aid the design process. The use of numerical simulations in an empirical design process allows for a greater degree of repeatability and is quite suitable for determining the relative merits of two competing designs. In this case the time taken to construct a functioning model can be leveraged with numerical optimization for relatively little additional effort.

The large deformations and strains that soft actuators are subjected to require that nonlinear solvers be used along with representative hyperelastic constitutive material models. Widely used material models are the Ogden (1972), Yeoh (1993), and other polynomial-type models like Rivlin and Saunders (1951).

Some of the earliest design work in soft robots being aided by numerical tools was in selecting the cross-sectional shape of a bending actuator to maximize tip displacement for a given pressure (Suzumori *et al.*, 2007). Other early work using numerical simulations was related to the design of individual bending actuators. These were designed specifically for hand

rehabilitation using the Pneu-nets architecture (Ilievski *et al.*, 2011; Polygerinos *et al.*, 2013) and FREEs (Faudzi *et al.*, 2012). This type of optimization requires that the geometry be defined by a fixed set of parameters. Parameters of the Pneu-nets were altered in wall thickness, height and quantity for specific design specifications prior to manufacturing. These alterations to the parameters of Pneu-nets were investigated with FE simulations conducted in parallel with experimental research by Mosadegh *et al.* (2014), Figure 2.6. Further, performance of a three-chamber bending actuator for use in surgical applications was numerically modelled and optimized to reduce the ballooning effect inherent to unreinforced actuators (Elsayed *et al.*, 2014). The addition of fibres, and the need to understand the effect of the fibre angle, led to the development of a numerical model used to explore the available design space (Connolly *et al.*, 2015) with further details given by Polygerinos *et al.* (2015). It enabled prompt characterisation and offered valuable insight to the effect of the angle.

A different type of simulation was performed by Roche *et al.* (2014) in modelling a replacement left heart ventricle using pneumatically actuated soft elastomers. In this configuration two different silicones were modelled simultaneously. The one silicone acted as the SPA and the other as fill material between actuators in order to get the desired twisting motion, Figure 2.7. Wakimoto *et al.* (2011) investigated the effect of including a negative pressure in the pneumatic supply line of a specific morphology. They thereby developed an actuator capable of bi-directional bending movement using a single air supply. This design was refined using numerical tools. The majority of the presented work was performed using licensed software packages such as MSC Marc and Abaqus. Moseley *et al.* (2016), however, developed a comprehensive open-source tool specifically for FE analyses of SPAs and used that for the analysis of pneumatic wearable assistive devices (Agarwal *et al.*, 2016).

The versatility of numerical tools to simulate performance under such dissimilar conditions, geometries, and composite materials is promising. An empirical design methodology using numerical tools has the ability to steer the design process and refine the design for specific applications, independent of the intuition of the designer. However, the numerical tools used are not capable of generating the initial geometry. These tools remain

dependent on manual design inputs. Mosadegh *et al.* (2014) cite further exploration of parameter space as a source for improvement in the class of finger-like robots investigated.

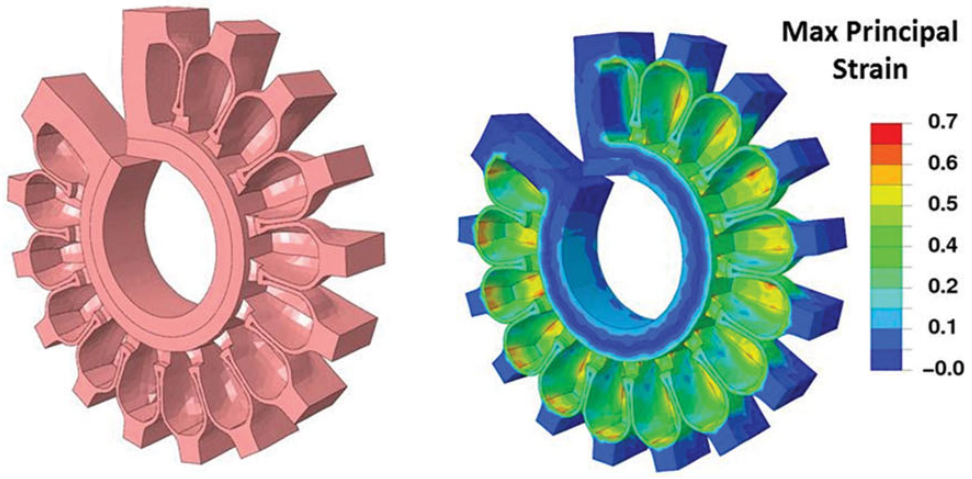

Figure 2.6: Numerical simulation of a fast Pneu-net designed using an empirical approach for improved actuation speed (Mosadegh *et al.*, 2014)

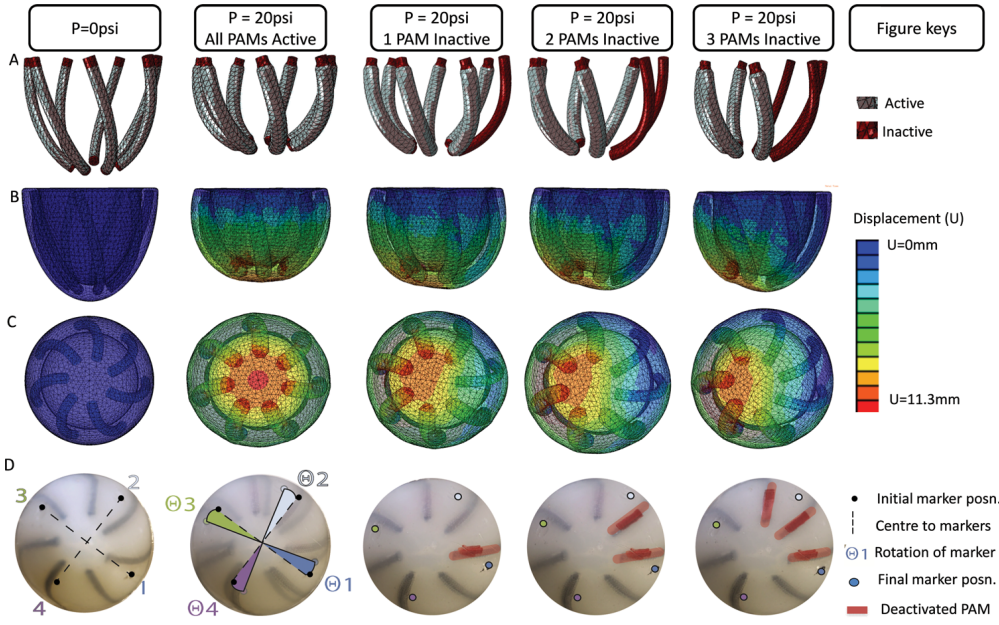

Figure 2.7: Numerical simulation showing the sequential deactivation of pneumatic artificial muscles (PAM) and the corresponding increase in the desired twisting motion of a heart ventricle (Roche *et al.*, 2014)

The versatility and simplicity of the empirical approach have been widely demonstrated. It is an ideal approach for pioneering applications, where inspiration can be drawn directly from biology, or where design constraints are not strict. It allows for practical designs to be generated regardless of whether a feasible analytical model can be constructed. It does however remain reliant on the physical input of the designer for which it is impossible to conceive solutions from the entire available design space. A method of enhancing this methodology with the addition of computational resources is required. These computational tools should facilitate and aid the process of exploration by selectively searching the available design space.

2.3.2 Analytical Design Methodology

Analytical models are well-suited to modelling phenomena where accurate assumptions can be made and physical conditions can be represented by mathematical relationships. Several factors contribute to making analytically modelling SPAs difficult, thus jeopardizing the achievable accuracy. Amongst these factors are the use of difficult to characterize nonlinear elastomers, pneumatic chambers consisting of different wall-thicknesses, and inflation being constrained in specific directions for the required functionality. The analytical approach requires that analytical models be deduced by the designer for the exact desired geometry, or that the geometry is simplified to a level where existing models can be used. The sacrifice in detail is often worth the explicit relationship that is obtained between inputs and outputs. Nonetheless, research has been undertaken investigating the possibilities of both simple and more complex actuated geometries.

One of the simplest actuated geometries exhibits one-dimensional linear translations, as evident in a McKibben-type muscle, Figure 2.8. This linear actuator consists of an internal bladder which is surrounded by individually braided fibres or fibre mesh in an anti-symmetric pattern. Dependent on the initial fibre angle, either extension or contraction can result upon pressurisation. Numerous studies have successfully produced analytical approximations for the behaviour of these McKibben muscles (Doumit *et al.*, 2009; Liu and Rahn, 2003; Ching-Ping Chou and Hannaford, 1996). The majority of analytical models currently available for soft robots exhibiting more complex deformed states than linear translations have been deduced for FREEs

and PneuFlex actuators. FREE and PneuFlex actuators are characterised by typically low degrees of freedom in the design and are in many cases suitable for analytical descriptions using fixed parametric models.

By using two families of fibres wound around the actuator at different, asymmetric, angles it is possible to achieve axial displacement and rotational or twisting movement along the length of the actuator. The decoupling of the kinematics and kinetostatics of a FREE can further allow the analytical complexity of the model to be reduced. This draws focus on the deformation characteristics in analyses of a two family actuator without the need to incorporate material properties (Singh and Krishnan, 2015). The model however remains a volume maximization problem subject to a set of constraints dictated by the inextensibility of the fibres. Material properties need to be reintroduced if actuation forces are required.

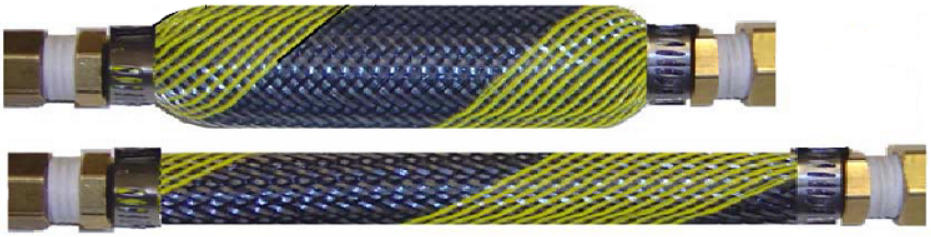

Figure 2.8: Pneumatic braided McKibben muscle shown in the pressurised (top) and deflated (bottom) states (Doumit *et al.*, 2009)

A further in-depth deduction of the equations for the modelling of FREEs that utilise an added layer of paper is available in Polygerinos *et al.* (2015). This paper layer acts as a strain limiter to create an asymmetric stiffness that results in a preferential bending direction. The deduced analytical model requires a strong mathematical foundation from the researcher for solving the partial differential equations and integrals. The ultimate goal of enabling FREEs to form part of regular mechanical design led researchers to present the results from these analytical equations as design selection charts in Bishop-Moser and Kota (2015). These design charts greatly simplify the design procedure.

A method was devised which allows for bending characteristics without the use of a strain limiting layer to be introduced in FREEs. By not restricting analyses to two sets of fibres wound at fixed angles, but by allowing

for an arbitrary number of fibres to be incorporated (Connolly *et al.*, 2016) it was possible to get the desired bending behaviour. This was achieved by modelling the fibre windings as a thin, separate anisotropic material on the actuator surface. This research resulted in a design strategy with the possibility of prescribing various input parameters that are related to the desired kinematic motion. An algorithm then outputs the specifics of the fibre windings and segment lengths required. The often arduous nature of physically winding these fibres has however resulted in a lack of repeatability in these FREEs (Memarian *et al.*, 2015). Research followed, devising new methods of pre-programming behaviour in actuators and ways of reducing the ballooning effect evident at relative high pressure. A laser cut silk mesh reinforcement along with a derivation from first principles of the angular displacement behaviour eased the repeatable manufacturing of bending actuators.

Euler-Bernoulli beam theory was used to model both the shape and applied load of a micro robotic tentacle without fibre reinforcement (Paek *et al.*, 2015). The deformed shape of the spiralling tentacle was modelled and an easy-to-solve model resulted. Modelling the static tip displacement of a bending actuator was undertaken by Onal *et al.* (2011). Inspired by the nonlinear relation in the two-balloon experiment, where two balloons inflated to different diameters and were allowed to freely exchange air, do not settle at equal volumes. The snap-through instabilities of inflated spherical membranes were amplified for linear actuation using analytical exploration to conceive a numerical algorithm determining the response (Overvelde *et al.*, 2015). This in-depth research led to actuators capable of a constant volume linear actuation to address the need for reduced pneumatic dependency in actuators. The design of soft robots can be aided by the analytical relationships in the research covered during the current section. The variety of relationships that exist are however limited to specific geometries and adapting these relationships for other geometries is not a trivial process. Further, this analytical methodology does not fare well at fully exploring the available design space as it is limited in its capacity to conceive new morphologies. Similarly to the empirical methods they are limited by the parameterisation scheme chosen. It can be concluded that an analytical methodology is not very conducive to designing soft robots for use in new applications.

2.3.3 Efficacy of Existing Design Methodologies

To date, the conceptual design of soft robots has resulted from the creativity and problem solving techniques of various researchers. While many great design problems have been solved with this approach, the question can still be asked whether faster, more accurate tools can be developed to assist. When the existing design space becomes large, it is possible that empirical methods can neglect to investigate design possibilities that are not necessarily intuitive or easy to conceptualise. Comparing the limitations of such manually conceived designs to the magnitude of possibilities that exists in the design space raises the question if existing designs are not potentially under performing or too time consuming to devise.

2.4 Generative Design Methodology

In order for the field of soft robotics to realise its full potential, Rus and Tolley (2015) recommend that, amongst other factors, creative individuals are required to design soft robots. Design methodologies utilised to date have shown inadequacies at performing well in the unstructured and large design space available. A different approach for designing soft robots is required altogether, one whereby the full design space can be explored by an organic means, to an extent not possible by manual methods. Human intuition must rather be leveraged with computational power and together provide the creativity that Rus identifies.

A new approach, similar to the evolutionary approach that has allowed nature to construct morphologies with heterogeneous materials to deliver high-performing bodies, is proposed (Cheney *et al.*, 2014). This method can be automated to reduce the need to observe all the details. Figure 2.9 provides a flow diagram of the general procedure for generative design.

An automated design methodology that incorporates evolutionary methods to investigate the design space is proposed here. Candidates that perform the best according to some fitness metric are allowed to evolve further. The best performing design according to the defined metric is ultimately obtained at the end of the design process. The choice of an evolutionary-based search technique is justifiable by the large scope of the problem (Rieffel *et al.*, 2014) and the non-intuitive nature of the solutions (Rieffel *et al.*,

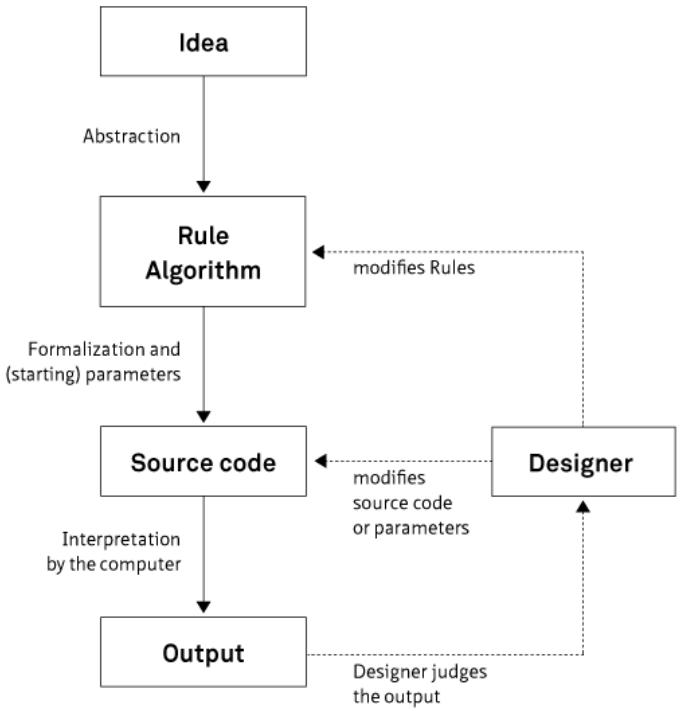

Figure 2.9: Flow diagram of a generative design procedure (Bohnacker *et al.*, 2009)

2009). Human intuition and engineering fare poorly in this regard due to the entangled and nonlinear design space (Cheney *et al.*, 2014). To date, the generative design methodology has seen limited use in the design of soft robots. This lack of an established generative design methodology for soft robots, is the result of the prohibitive computational costs of simulating flexible materials and the poor scaling of genetic encodings to large parameter spaces (Cheney *et al.*, 2014). The time consuming nature of the proposed approach therefore requires methods of developing fast and realistic simulations (Rieffel *et al.*, 2009).

The poor scalability of genetic encodings to large parameters spaces has been investigated. Approaches that account for the process allowing biological development to form require great computational resources when scaled-up. For soft robots, the level of detail computed using such a low-level approach can rather be traded for decreased simulation time. High-level of abstraction approaches that are based on the processes that give rise to natural forms have shown promise. These high-level approaches

are typically performed using compositional pattern producing networks (CPPNs), which are similar to artificial neural networks (ANNs), but where a more geometrically-useful transfer function is used (Cheney *et al.*, 2014; Hiller and Lipson, 2010; Clune and Lipson, 2011). The use of an indirect encoding like CPPNs allows the evolutionary process to capture patterns and regularities that otherwise need to be specified in direct encodings (Gauci and Stanley, 2010).

Rieffel *et al.* (2009) investigated different methods of reducing the simulation time while evolving physically embodied soft robots. A physics engine was used to perform the deformation analysis, as opposed to expensive non-linear FE analyses (Rieffel *et al.*, 2009). The soft-bodied material simulation capabilities of the physics engine was tested and compared to a reduced-order lumped model of the body. The lumped model provided a computationally efficient model for the evolutionary optimisation and yielded accurate results in comparison to experimental data. However, the non-trivial task of hand coding the system parameters was a major drawback. A second approach focused on reducing the time spent solving morphologies with a low-level of evolution typical in the initial stages of the evolutionary process. By using a coarser mesh on the solid body during the initial stages, the computation time was drastically reduced. However, once the switch to a finer mesh resolution was made after a set time, a drastic reduction in the calculated fitness resulted, Figure 2.10. The performance of a gait was found to be tuned to a specific mesh resolution. Gaits and physical properties evolved at specific mesh resolutions do therefore not translate well when placed in a higher-resolution simulation (Rieffel *et al.*, 2014).

Lipson and Hiller conducted more research using an evolutionary algorithm to investigate the forward locomotion of a robot manufactured by an automatic design process. Soft volumetrically actuated expanding materials were used. Forward locomotion was achieved for different pressure (Hiller and Lipson, 2012*b*) and temperature activated materials (Hiller and Lipson, 2010). Further research into a pressure activated robot capable of locomotion increased the available materials from two to four, each of which have different stiffness characteristics, Figure 2.11. This study posed the exact problem to multiple scientists and asked that a robot be designed by hand. None of the designed robots could outperform the evolved design

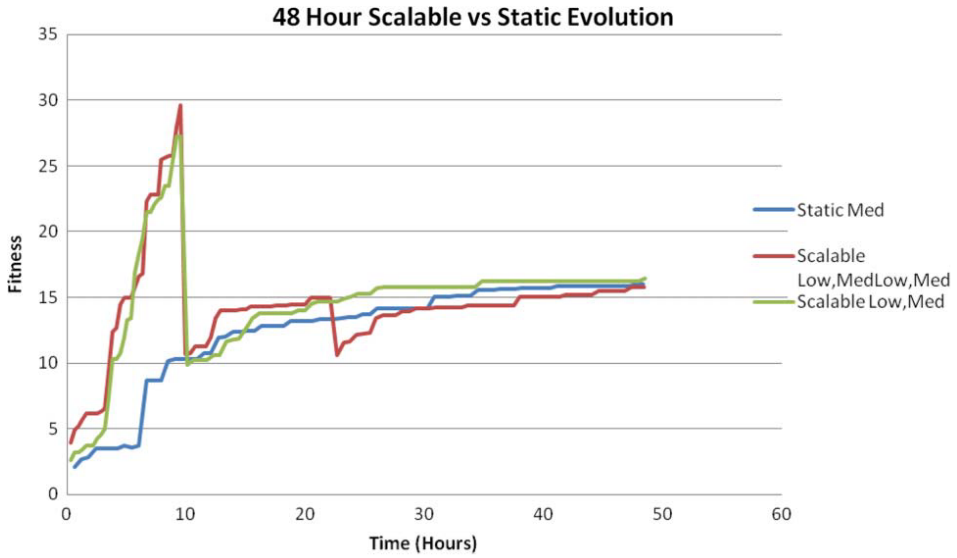

Figure 2.10: Results comparing the consequence of switching mesh resolution of a solid body over the course of the evolutionary process. It shows that a sharp drop in computed fitness results once the switch to a finer mesh has been made (Rieffel *et al.*, 2014). The legend indicates the relative mesh density used.

and participants noted the difficulty in designing such robots using multiple materials (Cheney *et al.*, 2014).

Although soft robot design using generative methodologies has thus far enjoyed limited research efforts, the ability of a generative methodology to create designs that could otherwise not have been devised, has been demonstrated. The conclusions from current research indicate that generative methodologies provide a promising technique that will be able to play an important role in the future design of soft robots to meet high level functional goals (Hiller and Lipson, 2010).

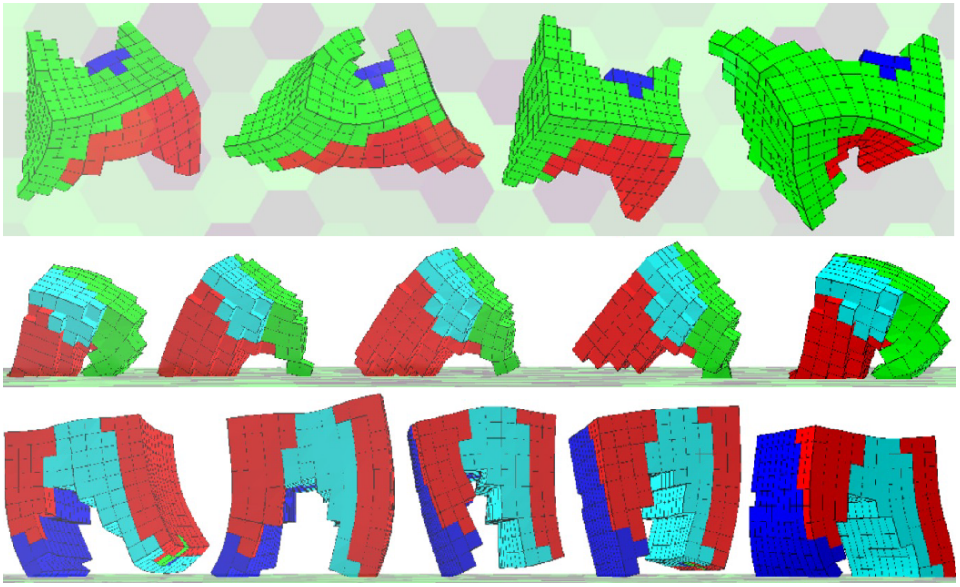

Figure 2.11: Time-series of three different evolved strategies for a walking robot using a generative encoding and four different material stiffnesss (Cheney *et al.*, 2014)

2.5 Design Methodologies in Context

In the presented review two widely used design methodologies of soft robots have been identified as being:

1. Empirical design methodology
    a) Physical experimentation based iterative manufacturing of manually generated designs
    b) Numerical simulation based iterative investigation of simulation results of manually generated designs
2. Analytical design methodology deduce governing equations of physical phenomena either from first principles or the adaption of existing theory to soft actuators.

Each of these methodologies has its advantages and drawbacks. The analytical methodology allows for designers to use identified relationships between various parameters to specify the details of the design. This, however, comes at the price of limited freedom to deviate from the parameterisation scheme for which the equations were derived. Not relying on the

description of the underlying mechanics of the design, the empirical design process allows the designer to manually conceive actuator morphologies from any source of inspiration.

Soft robots have a large feasible design space which poses limitations on the extent it can realistically be explored using such manual approaches. This leads to the natural progression of automating the empirical process by the addition of computational resources. Computational resources can be incorporated by means of numerical models that are run as part of an optimisation procedure. The current research develops a generative methodology for soft pneumatic actuator design. This generative methodology is presented as a logical succession to the empirical methodology as both are fundamentally an evolutionary process. Even though limited literature exists on the application of such a generative process, evidence is available in the literature to demonstrate the benefits to the field. By harnessing the potential of high performance computers and combining that with a methodology on generative design, it will be possible to design soft robots that have been evolved to best represent the available design space for the required application.

Throughout this work, the more traditional methods of design are however still used as the generative procedure only lends itself to certain applications. The work presented in Chapter 3 was more conducive to empirical and manual design methods. Experimentation-based design was preferred as rapid changes to the geometry could be made and the effect investigated. The generative design procedure was developed with focus on modularity, and not geometry-based changes.

2.6 Material Modelling

A key aspect to creating accurate FE models of structures is the ability to capture the material response to external loading. For most metallic materials the relationship between stress and strain is linear within the elastic region of the material and can be modelled using Hooke's law and Young's modulus. Depending on the strain range in question the nonlinear hyperelastic response of silicone is often simplified and modelled as a linear-elastic behaviour. This simplification requires that only the elastic modulus and

Poisson's ratio be known, but breaks down at high strains. Roche *et al.* (2014) successfully used a linear-elastic model in their numerical modelling of soft actuators for replacing the left heart ventricle with a bio-inspired material. In their application the Ecoflex 0030 was however merely used as a matrix material and not as a pneumatic actuator, therefore drastically reducing material strain. This relationship however does not exist for the majority of silicones. It is therefore required to perform a material modelling procedure. Material modelling in this context involves a constitutive equation and the corresponding material dependent coefficients to populate that relationship (Bergstrom, 2015):

$$[Constitutive\ model] + [Material\ parameters] = [Material\ model]$$

These hyperelastic models assume that the material behaviour can be described by a strain energy density function and are grouped according to three classifications; mechanistic models, phenomenological models, and hybrid models that combine the previous two approaches. Mechanistic models are derived from a theoretical basis and the underlying mechanics of the material. Phenomenological models are not derived from such first principles but rather describe the behaviour of the material and the observed relationship between variables. Characterisation of soft materials for use in soft actuators favour phenomenological models where results from multiple modes of experimental testing can be used for model calibration (Moseley *et al.*, 2016).

Modern FE software packages contain libraries of the most popular phenomenological constitutive equations as standard. Equations not included by default can be implemented via external user subroutines. Depending on the software being used however, this implementation might not be trivial or time efficient. For this reason, the different constitutive equations available in Siemens NX12 (Siemens NX12, 2017) were investigated and their ability to model the three silicones in this project evaluated.

Results from literature suggest that the silicones have no irreversible effects, time dependency or history-related behaviour. The response is therefore that of an isotropic, nonlinear, and elastic material which is conducive to hyperelastic constitutive equations. Hyperelasticity is a generalisation of linear elasticity for nonlinear and large strain predictions. The following

descriptions have been adapted from Bergstrom (2015) and Bathe (2014) if not stated otherwise. This form of modelling requires that stress (2^{nd} Piola-Kirchhoff) be calculated as

$$S_{ij} = \frac{\partial W}{\partial \epsilon_{ij}} \tag{2.1}$$

where ε_{ij} is the strain tensor and W the elastic energy stored in the material during loading, also known as the strain energy density, , described as

$$W = f(I_1, I_2, I_3) \tag{2.2}$$

with I_1, I_2, and I_3 the three invariants of the deformation gradient tensor, defined in terms of the three principal stretch ratios

$$I_1 = \lambda_1^2 + \lambda_2^2 + \lambda_3^2 \tag{2.3}$$

$$I_2 = \lambda_1^2\lambda_2^2 + \lambda_2^2\lambda_3^2 + \lambda_3^2\lambda_1^2 \tag{2.4}$$

$$I_3 = \lambda_1^2\lambda_2^2\lambda_3^2 \tag{2.5}$$

where stretch, λ, is related to engineering strain, ε, by $\lambda = \varepsilon + 1$.

The strain energy density can be calculated from two components

$$W = W_D + W_V \tag{2.6}$$

where W_D is the deviatoric strain energy density and W_V the volumetric strain energy density. In certain applications the material is assumed incompressible, setting $I_3 = 1$ and resulting in a volumetric strain energy density of zero.

The elastic properties of the silicone rubbers can be described in terms of the strain energy function which is an infinite power series in the strain invariants I_1, I_2, and I_3. The simplest forms of this function is the neo-Hookean, which can be obtained by truncating the infinite series to the first term in I_1 and the Mooney-Rivlin, which is a function in I_1 and I_2 (Yeoh, 1993). These two functions, along with the Ogden and Yeoh models are evaluated on their performance. These material models, as well as the mechanical testing used to calibrate them, are used as a means to an end in this research. Being able to get stable, accurate models for various loading conditions is an active research field and is not in line with the overall scope of this project.

Neo-Hookean

A neo-Hookean material model is the nonlinear equivalent of Hooke's law for stress-strain behaviour and large deformations. In a three-dimensional environment and for an incompressible material, the strain energy density function is

$$W^{NH} = C_1(I_1 - 3) \tag{2.7}$$

where C_1 is a material constant (MSC.Marc, 2018*a*). For a compressible material in a planar loading mode the strain energy density function becomes

$$W^{NH} = C_1(\bar{I}_1 - 3) + D_1(J-1)^2; J = \lambda_1\lambda_2 \tag{2.8}$$

where D_1 is a material constant and $\bar{I}_1 = I_1 J^{-1}$.

Mooney-Rivlin

The Mooney-Rivlin model is an improvement to the neo-Hookean model by including a linear dependence on I_2 as well. A few variations of this model exist of which two will be considered; the two-term and three-term deformation models for an incompressible material. The two-term model (MR2) is given by

$$W^{MR2} = C_{10}(I_1 - 3) + C_{01}(I_2 - 3) \tag{2.9}$$

and the three-term model (MR3) by

$$W^{MR3} = C_{10}(I_1 - 3) + C_{01}(I_2 - 3) + C_{11}(I_1 - 3)(I_2 - 3) \tag{2.10}$$

where C_{10}, C_{01} and C_{11} are material constants obtained from experimental data. The MR2 model is linear in the strain invariants and can therefore not accurately capture nonlinear responses. The addition of a second-order term in MR3 allows for better predictions of nonlinear behaviour.

Yeoh

The Yeoh (1993) model remains a phenomenological representation and is a third-order model in I_1, with no dependence on I_2. Due to the higher order

I_1 terms the model is capable of improved accuracy over the neo-Hookean model and also has fewer stability issues than the MR2 and MR3 models. For the incompressible case a generalized version of the Yeoh model is given by

$$W^{Yeoh} = \sum_{i=1}^{n} C_i (I_1 - 3)^i \tag{2.11}$$

where C_i are material constants obtained from experimental data.

Ogden

The Ogden model is typically an improvement over the Mooney-Rivlin model and is used for rubber-like materials and materials that are subjected to high strains. Instead of using principal invariants as most other hyperelastic models, the Ogden (1972) model makes use of the principal stretches. For a compressible material, the strain energy density then takes on the form

$$W^{Ogden} = \sum_{n=1}^{M} \frac{\mu_n}{\alpha_n} [J^{-\alpha_n/3}(\lambda_1^{\alpha_n} + \lambda_2^{\alpha_n} + \lambda_3^{\alpha_n}) - 3] + \frac{9}{2} K (J^{1/3} - 1)^2 \tag{2.12}$$

where μ, α, and K are material constants obtained from curve fitting of experimental data. In a follow-up publication, Ogden *et al.* (2004) state that sufficient convergence between experimental and theoretical results are achieved for $M = 3$.

Usage in Literature

Elsayed *et al.* (2014) used phenomenological models for characterising three different grades of silicone whilst researching finite element (FE) analysis and design optimisation of soft robotics for surgery applications. They worked with Ecoflex 0030, 0050, and Dragonskin 0030 and found that three different models were required to describe each of the different incompressible materials. The Yeoh model was also used by Polygerinos *et al.* (2013) for Elastosil M4601 with Shore hardness of 28 on the A-scale. Moseley *et al.* (2016) used the Ogden model for the response of Ecoflex 0030, but did not assume an incompressible material and therefore measured volumetric deformation during physical testing. The added accuracy of not assuming an incompressible material was not investigated.

Chapter 3

Bimodal Response in Soft Pneumatic Actuator

This chapter is a reproduction of a conference paper titled 'Bilinear Response in Paper-Silicone Composite Material' Ellis et al. *(2018). The paper is co-authored by my supervisors Dr Martin P. Venter and Prof. Gerhard Venter of the Department of Mechanical and Mechatronic Engineering at the University of Stellenbosch, South Africa. Their contribution was as a supervisory role.*

3.1 Background

A soft pneumatic actuator (SPA) using a simple actuation method, such as an increasing pneumatic pressure, will lead to a known deformed state (Ilievski *et al.*, 2011). To date, most common SPAs rely on a unimodal response to proportional pneumatic pressure changes (Cook and Walker, 2016) (Lampani and Gaudenzi, 2010). In the case of a linear actuator more pressure brings more elongation and in the case of a bending actuator, more bending. When blocked, they apply more force. Bending type SPAs make use of an asymmetric stiffness to bias the direction of deformation (Shepherd *et al.*, 2011). If more material is used on one side of the design than the other, it has an asymmetric stiffness and deforms less under the same load, Figure 3.1. Several design iterations showed that it is possible to adapt the configuration by embedding a flat strip of stiffer material, typically paper, into the design on only one side to create the asymmetric stiffness, Figure 3.2 (Mosadegh *et al.*, 2014). This layer is appropriately called a strain limiter -

limiting strain on that specific surface, causing the actuator to inflate and deform relative to it.

It was further found that by breaking the continuity of the more compliant side, more rapid articulation could be achieved at lower pressure (Mosadegh *et al.*, 2014). It is however conceivable that a more complex response becomes desirable without the need for multiple actuators or actuation sources. SPAs provide a flexibility of design that is useful in this regard (Kim *et al.*, 2013).

(a) Initial geometry (b) Pressurized geometry

Figure 3.1: Bending due to preferential stiffness

(a) Initial geometry (b) Pressurized geometry

Figure 3.2: Bending SPA with embedded strain limiter

An example of such a response is bidirectional bending or motion. Wakimoto *et al.* (2011) investigated the numerical modelling and manufacturing of a miniature curling actuator. For their actuator a single air-supply tube was used, but the actuator required both positive pressure and vacuum sources to get the two different bending directions. Paez *et al.* (2016) successfully manufactured a bidirectional bending SPA using an origami shell

reinforcement using only positive pressure, but which requires two separate air-supply tubes. Marchese *et al.* (2014) required bidirectional bending in attempting to replicate the swimming motion of an escaping fish. In their work this was achieved by essentially combining two independent bending actuators back-to-back and inflating each actuator as required.

A method that embeds a bimodal, as opposed to only a bidirectional response, in an actuator is desired to simplify the control means. This bimodal actuator must exhibit different distinct deformed states dependent on the internal pressure i.e. an initial bending direction that changes to a second mode once the internal pressure exceeds the controlling design parameter. This actuator should use a single air-supply tube and a positive linear pressure ramp as its source. The versatility offered by the varying stiffness distribution of the paper strain limiter is investigated as the method of embedding the desired behaviour.

This chapter proposes that by changing the configuration of the strain limiting layer in the design of a SPA, a bimodal response can essentially be pre-programmed into the actuator. Instead of using a flat embedded paper layer, a strain limiter preconditioned to a crimped initial geometry will be embedded. Under low strain the stiffness of the material is mostly that of the silicone matrix material. As the strain increases, the crimped paper strain limiter decrimps, increasing the effective stiffness. Once the strain limiter is fully decrimped, the stiffness becomes that of the paper layer. This crimped layer helps create a bilinear material with two distinctly different linear regimes. The actuator will therefore have different preferential bending directions depending on the strain the bilinear material is subjected to.

This chapter covers the development of the required bilinear material and how that is incorporated into the design of a bimodal actuator. Physical experimentation and numerical models formed part of this process. Where appropriate, the material testing and experimental procedure are briefly covered with further details available in Appendix A and Appendix B respectively.

3.2 Bilinear Composite Material

In order for the bimodal actuator to function as envisioned, it is required that the bilinear composite has two distinctly different linear regimes depending on the longitudinal strain. The initial stress-strain response should have a linear stiffness as low as can repeatably be attained using the combination of base materials. This is to ensure that the first bending mode of the actuator is such that the bilinear composite is on the outer radius of the bending actuator. After a predictable and tunable amount of strain, the composite should transition to a second linear stiffness. The exact strain at which this transition occurs is termed the strain transition point. The second response mode of the composite should be orders of magnitude stiffer to ensure that the actuators' second bending mode is such that the bilinear composite is along the inner radius of the inflated actuator. To achieve this, 80gsm white bond copy paper is used as the rigid, pre-crimped component of the composite and Ecoflex 0030 as the matrix material.

3.2.1 Sample Geometry

A single crimped architecture is investigated making use of a triangular wave pattern, Figure 3.3. The amplitude (A) is maintained at 1.5 mm and the wavelength (λ) of the crimp architecture varied to investigate the effect of the effective strain limiter length. The degree of crimp is defined as the ratio of the amplitude to the wavelength , $CR = A/\lambda$. Three ratios were chosen for investigation, Table 3.1.

The response of each base material was tested to determine their individual response to uniaxial tensile loading with three replicates each. The printer paper was tested according to ASTM D828-16 and the Ecoflex 0030 according to the ISO 37 standard for tensile testing elastomers using a dumbbell geometry.

3.2.2 Analytical Modelling

It is hypothesised that the strain transition point can be predicted using the effective length of the strain limiting layer. The effective length, L_e, of the strain limiting layer can be calculated using the number of flutes, N, and

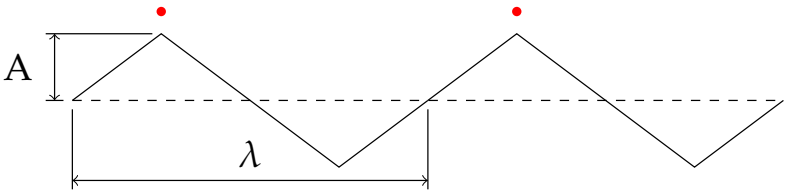

Figure 3.3: Triangular wave pattern of crimped strain limiter including the positions of the nodes used in Figure 3.6

Table 3.1: The ranges for variables investigated

Variable	Range
Material: Paper	Purco 80 gsm
Material: Silicone	Ecoflex 0030
Crimp style	Triangular
Crimp ratio (CR)	0.3, 0.25, 0.2

the length of each flute, s, in the strain limiter, Eqs. 3.1, 3.2, and 3.3. The side length of each flute can be calculated using Pythagoras' theorem and the amplitude and wavelength of the crimp, Eq. 3.1. The onset of strain stiffening should commence when the crimped strain limiter has fully decrimped. This stiffening strain can be calculated as a ratio of the effective length and the original crimped length, L_0, Eq. 3.4.

$$s = \sqrt{(2A)^2 + (\frac{\lambda}{2})^2} \tag{3.1}$$

$$N = \frac{L_0 - \frac{\lambda}{2}}{\lambda} \tag{3.2}$$

$$L_e = 2Ns \tag{3.3}$$

$$\varepsilon_{transition} = \frac{L_e - L_0}{L_0} \tag{3.4}$$

3.2.3 Numerical Simulation

Numerical modelling often offers additional insight into the behaviour of structures that cannot be measured during physical testing or captured in

analytical derivations. A 2D numerical model of the silicone-paper composite was constructed using finite element methods. A plane strain, displacement controlled analysis was performed. The silicone matrix material was represented using linear 4-node elements and a Ogden three-term model to capture the material response. The paper layer was modelled using 2-node rebar elements and a linear material model. Rebar elements were used in order to increase the computational efficiency of the model; the alternative method of including contact analysis between the different layers is cumbersome and could lead to numerical instability. Rebar elements, typically placed within existing elements, are hollow elements in which single strain members such as reinforcing rods or cords can be placed. This method allows the rebar and filler to be represented accurately with respect to their stress distribution as separate constitutive theories can be used for each (MSC.Marc, 2018*b*). Filler and rebar meshes need not line up either for the analysis to solve. The model was constructed and solved using MSC Marc; Siemens NX 12 does not support rebar elements which were crucial in this analysis.

Load is applied as an enforced displacement to a single node attached to the end of the paper layer, Figure 3.4. The corresponding node on the other end of the sample is fully constrained. This method is consistent with the physical testing where only the paper layer was clamped between the grips.

The non-uniform silicone thickness distribution caused by the crimped paper layer transfers through to the deformed shape of the bilinear material. Results from the simulation show a surface deformation consistent with that observed during physical testing, Figure 3.5. This cyclic surface deformation corresponds to peaks in tension and valleys in a compressive state of stress. The magnitude of this non-uniform strain distribution is shown in Figure 3.6 for half a wavelength of the crimped paper layer, starting at a node on the silicone surface corresponding to a peak in the paper layer and ending in a valley.

3.2.4 Sample Manufacturing

The silicone, paper, and composite material samples were manufactured to identical geometries and dimensions. A two-part mould manufactured using fusion deposition modelling 3D printing was used to cast the composite

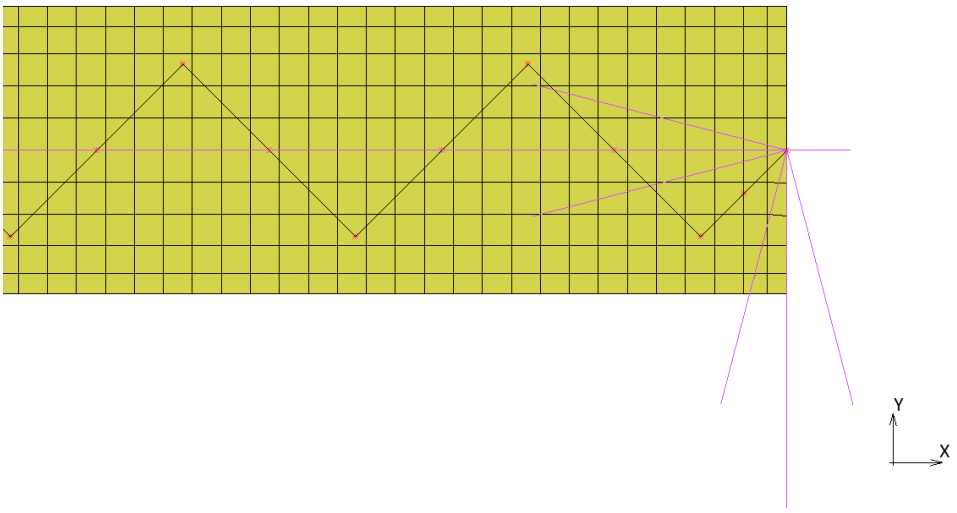

Figure 3.4: Boundary condition applied to the bilinear material. Displacement is constrained in the Y direction and an enforced displacement is applied in the X direction. The crimped paper layer can be seen surrounded by the yellow mesh used to model the Ecoflex 0030

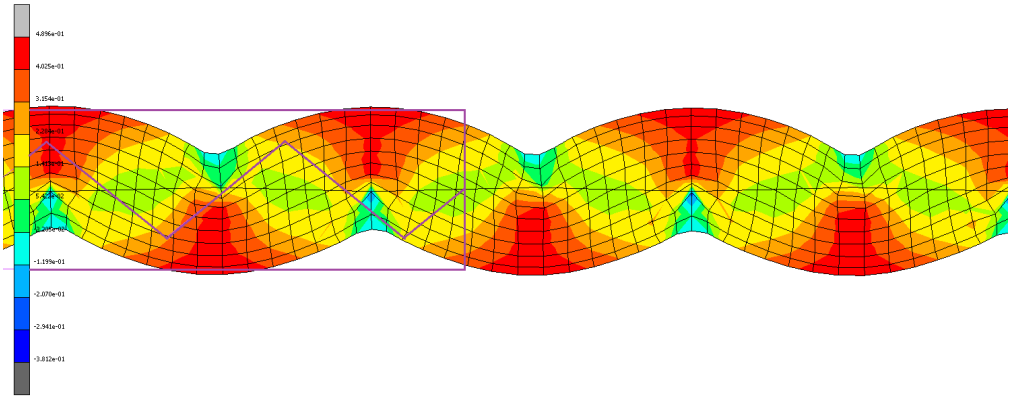

Figure 3.5: Deformed shape of the composite material at 60 mm of total displacement, a crimp ratio of 0.2, and an initial length of 176.25 mm. The faint purple lines indicate the original shape of the material. The paper strain limiter is fully decrimped at this strain value. The contour plot shows Total Strain in the longitudinal direction

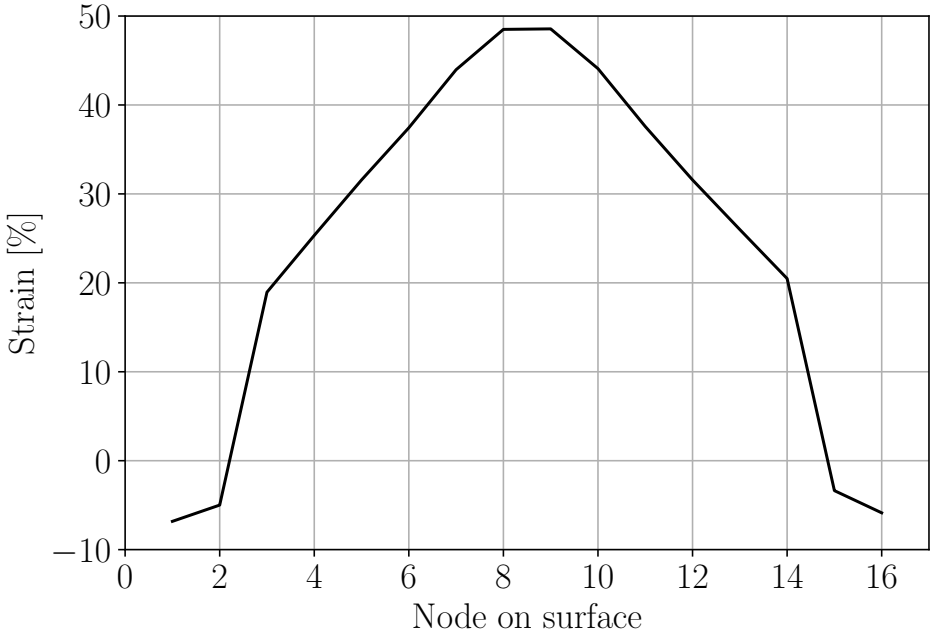

Figure 3.6: Non-uniform surface strain distribution of the deformed bilinear material for a crimp ratio of 0.2. The corresponding nodes on the crimped paper layer are shown in Figure 3.3

bilinear material in. These moulds were designed with a split along their length to accommodate the paper layer in the middle and ensure a continuous distribution of uncured silicone prepolymer along the entire length of the sample. An iterative experimental approach was followed to find a mould design and manufacturing procedure that yielded consistent results.

3.2.5 Physical Testing

Tensile tests were performed on an MTS Criterion frame with a 500 N HBM load cell. Strain was measured using digital image correlation (DIC) hardware of the Strain Master system from LaVision with the StrainMaster software package. Further details of the testing procedure are available in Appendix B.

3.2.6 Results and Discussion

Bilinear Material Physical Testing

Figure 3.7 shows the tensile response of the matrix material with embedded strain limiters for a range of crimp ratios (shown as averaged surface strain of the deforming sample). It can be seen in the response of the composite materials that as the crimp ratio is increased, the effect of the strain limiter is delayed. This is due to the increase in the effective length of the embedded strain limiter. Table 3.2 summarises the response of the three composites with the different crimp ratios. The primary modulus was calculated using a linear regression model fit to the first 10 % of strain. This range was chosen as all three the different crimp ratio materials exhibit clear linear behaviour there. The secondary modulus was calculated using a linear regression model fit to the last ten data points. The transition point is the strain value at which these two linear models intersect.

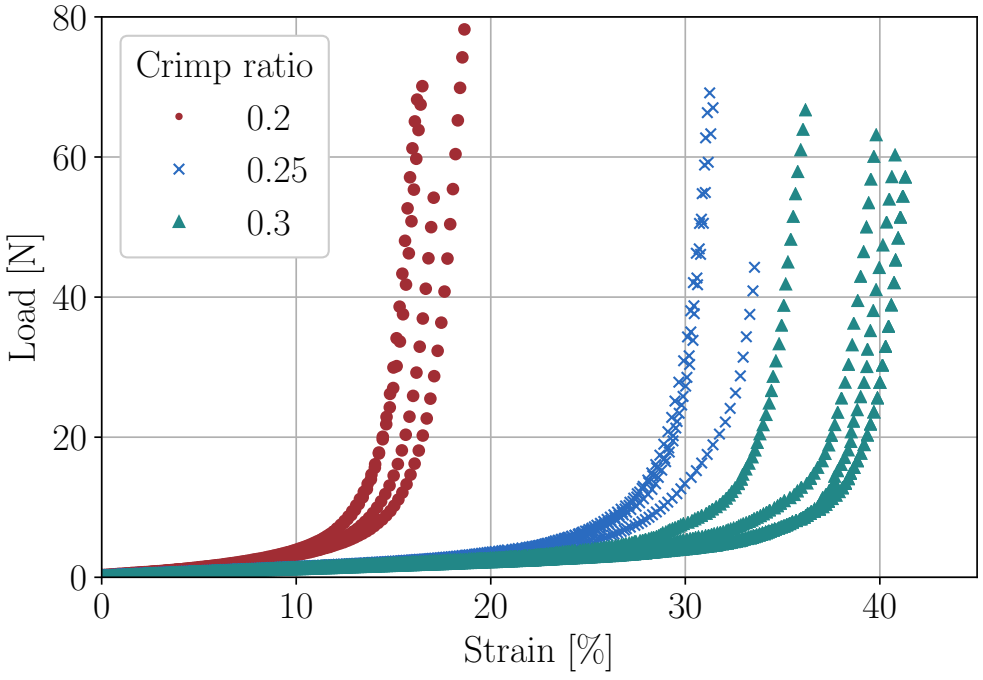

Figure 3.7: Load-averaged strain response of physical tests for three different crimp ratios

Table 3.2: Material parameters for composite bilinear material (standard deviation shown in brackets)

Crimp ratio	Primary modulus	Transition strain	Secondary modulus
0.2	216 kPa [18.5]	15.2% [0.95]	25.2 MPa [2.33]
0.25	81.9 kPa [1.87]	30.0% [0.96]	20.7 MPa [4.39]
0.3	80.0 kPa [8.06]	35.6% [3.58]	16.5 MPa [1.60]

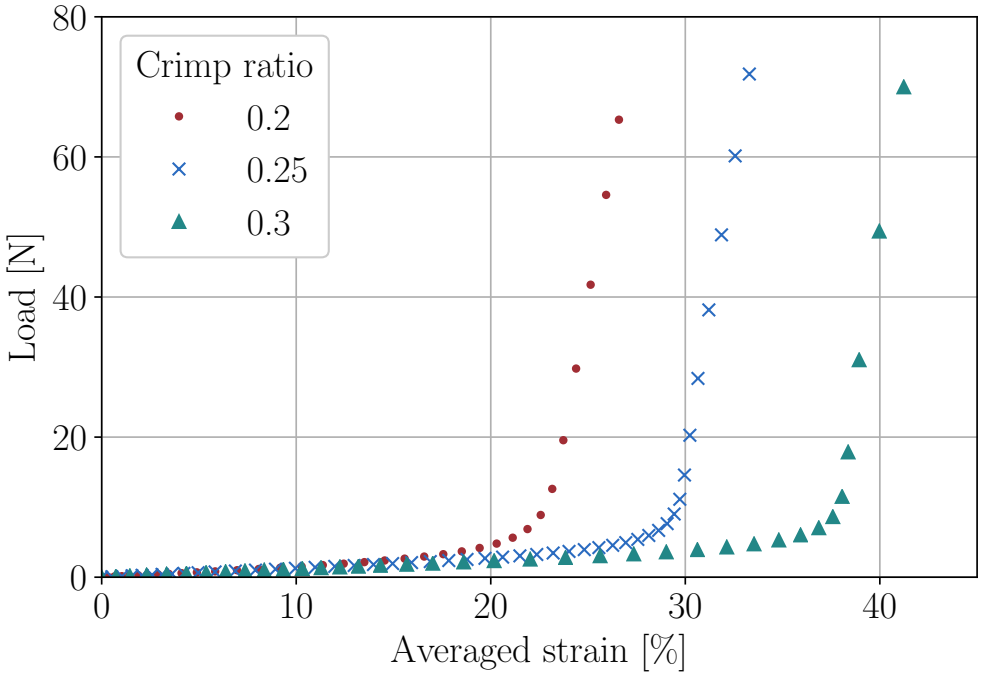

Figure 3.8: Load-averaged strain response of numerical model for three different crimp ratios

Numerical Model

The load-strain response of the numerical model is shown in Figure 3.8 using the averaged strain results. As the numerical model is a 2D representation of the cross-section, the average surface strain could not be calculated as done for the physical models. Instead, the average strain of all the nodes on that outer line section was calculated. The distinct bilinear behaviour is evident. The trend of a delayed response before the strain limiter becomes effective while increasing the crimp ratio, remains evident.

Table 3.3: Measured and theoretical strain stiffening transitions (standard deviation shown in brackets)

Crimp ratio	Measured (Mean)	Numerical (Averaged)	Analytical	Numerical (Engineering)
0.2	15.2 % [0.95]	22.7 %	27.9 %	28.3 %
0.25	30.0 % [0.96]	29.5 %	39.0 %	41.8 %
0.3	35.6 % [3.58]	38.2 %	54.4 %	55.9 %

Correlation of Transition Strain

Transition strain is the strain at which stiffening due to the decrimped paper starts to occur. Results for this strain value as predicted from the various models are summarised in Table 3.3, using mean values where necessary. These results indicate that close correlation exists between the analytical model and numerical model when comparing engineering strain, also shown in Figure 3.9 for an extrapolated prediction of the analytical model. This correlation remains for two of the three crimp ratios when comparing the results measured during physical testing. As shown with the numerical model, the results from the two different methods of calculating strain differ significantly. Therefore the averaged surface strain of the physical test cannot reasonably be compared to that of the analytical model. Results from the numerical model were used to provide a better insight into the surface strain measurement. These results indicate that the strain value predicting the transition decreases when the averaged values are used, but that a prediction error of between -1.6 to 49.3 % still exists in relation to the physical test. The manufacturing process allowed the three different composites to be produced with a standard deviation of 3.2-10 % amongst the four replicates made and tested.

Improved Manufacturing Procedure

With focus solely directed at the crimp ratio of 0.3, an improved manufacturing and data processing procedure was devised to try and bridge the gap between the three different models and also reduce the variation between physical replicates. A new mould system was designed that offers better support to the paper layer while the silicone pre-polymer is poured, shown in Appendix B.

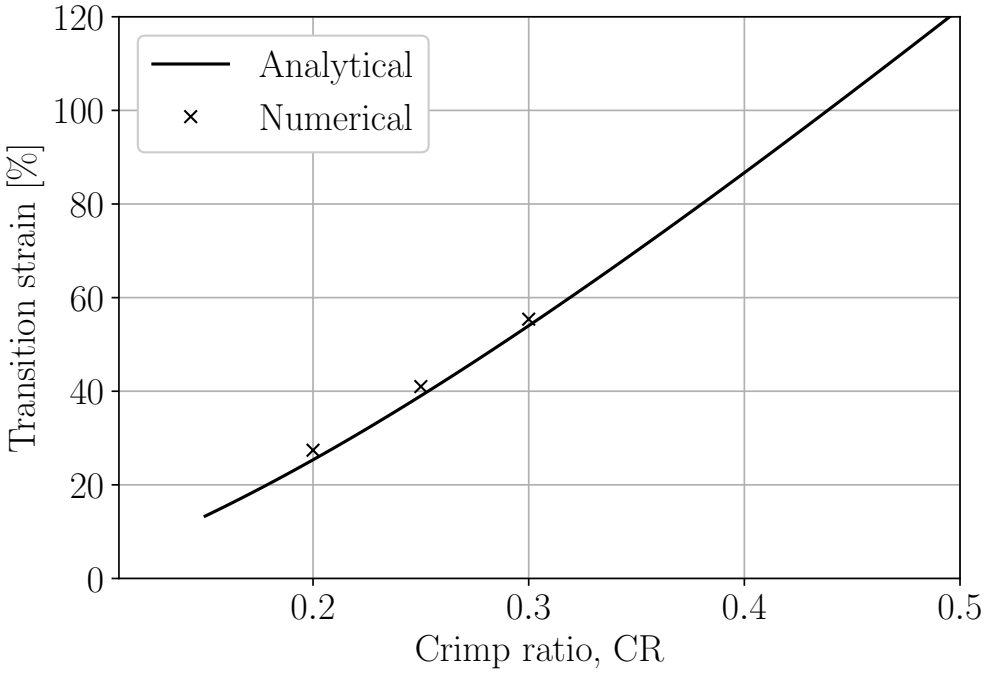

Figure 3.9: Transition strain values as predicted using the analytical model and measured using the numerical model

A custom Matlab script allowed for an array of varying discrete length virtual strain gauges (VSG) to be randomly placed on the surface of the deforming sample and the average thereof calculated. Each VSG length is a multiple of 5 mm to coincide with the wavelength used in the crimped paper layer. Although VSGs calculate engineering strain on an individual basis, by taking the average of various length VSGs the results will approximate the values calculated using the averaged surface strain. This variability is quantified using a statistical analysis. Based on the infinite population size, the minimum sample size is calculated as:

$$N = \frac{Z^2\sigma(1-\sigma)}{e^2} \tag{3.5}$$

where σ is the probability of the spread, Z is the adjusted value for a given confidence interval, and e the predicted margin of error. Using a 95 % confidence interval, predicted margin of error of 5 % and a predicted probability spread of 0.5, the minimum number of VSGs to apply are $N = 385$. The improved results and processing show that a new sample can be manufactured

having a 95 % chance from deviating within 5 % of the calculated strain transition point of 38.8 % for the tested crimp ratio. This updated result of the transition point further improves the deviation from the numerical model in Table 3.3 from a 6.8 % over-prediction to a 1.6 % under-prediction.

3.2.7 Response Modelling using a Hyperelastic Model

This research aims to construct a full 3D model of the bimodal actuator in which the response of the actuator is the focus. To reduce the possibility of convergence issues stemming from intricacies of the bilinear composite, it was decided to rather directly model the response of the composite and use that response in the FE model. Details of the various hyperelastic models considered are included in Appendix A. The stress-strain response was modelled using an existing set of hyperelastic constitutive equations which allows for the material to be defined in a similar way as any other nonlinear hyperelastic material within the FE environment. Four different material models were tested for modelling this behaviour and MSC Marc was used to determine the coefficients.

The performance of these models, as fit to a material with a crimp ratio of 0.3, is shown along with the experimental test data in Figure 3.10. The Ogden model is superior at matching the material response. It is important to note that the strain transition point of the material model (39.9 %) is in close agreement with that of the experimental tests (38.8 %). Ogden models were therefore calibrated for all three different crimp ratios (0.2, 0.25 and 0.3).

3.3 Bimodal Actuator

3.3.1 Design Criteria

Silicone has a highly nonlinear deformation characteristic. Coupling this with the response of the bilinear composite, it becomes difficult to predict the shape of a bimodal SPA purely by intuition. However, empirical methods and numerical tools offer solutions to deal with iterative designs problems and will be used here.

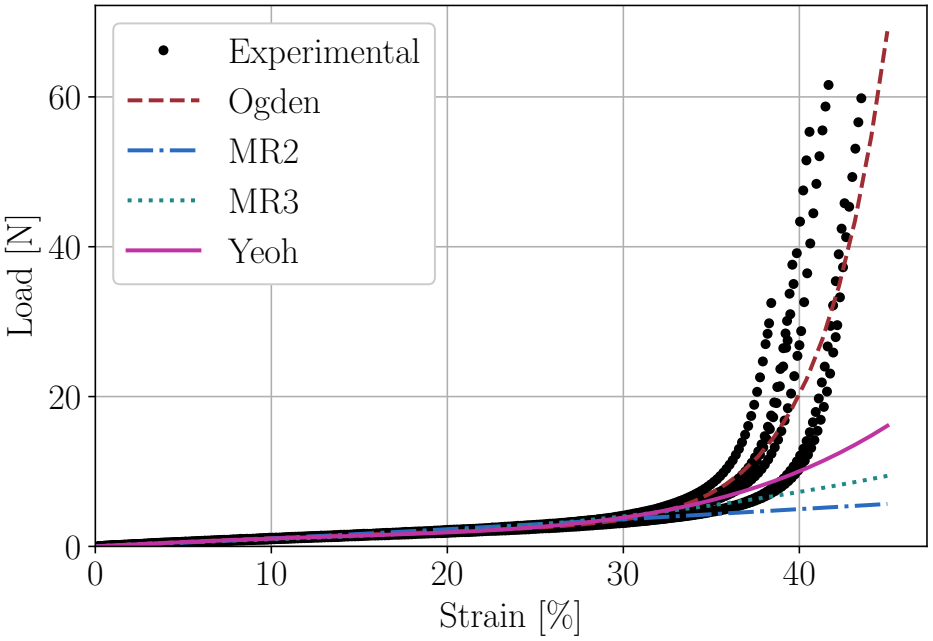

Figure 3.10: Response of various material models as fitted to the bilinear material with a crimp ratio of 0.3. The Ogden parameters are available in Appendix B

The basic design describing a Slow Pneu-net (a type of SPA) by Mosadegh *et al.* (2014), Figure 3.11, is used as guideline for the morphology of the actuator in this work, where the inextensible layer referred to is replaced with the bilinear composite. The Slow Pneu-net is preferred over the Fast variant in the current work due to the continuous and smooth surfaces all-round, crucial for attempting bimodal behaviour at this stage. To this end, a base design was chosen to which sections of material could easily be added as needed. This baseline actuator shares its dimensions with the actuator used throughout this dissertation and is 157.5 mm long, 15 mm wide, 17.5 mm high, has 15 inner voids and is manufactured using Mold Star 15, Figure 3.12. The height of the actuator varies between different design objectives as additional material is added to the top edge of it in order to get the different modes. These additional sections comprise individual thin layers of Mold Star 15 and a much stiffer Smooth-Sil 950.

In order to get two distinctly different bending directions, it is required that the actuator be pre-programmed with two preferential bending direc-

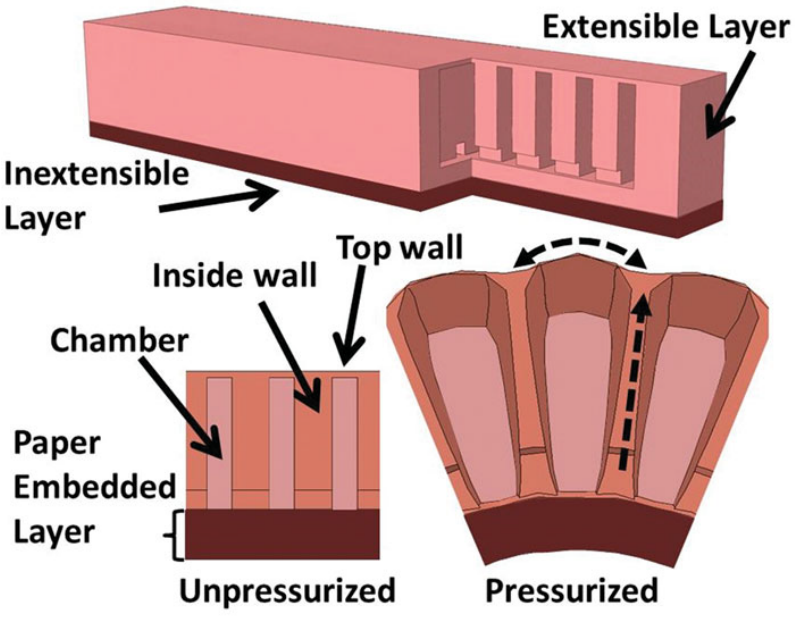

Figure 3.11: Cross-sectional view of a Slow Pneu-net (Mosadegh *et al.*, 2014)

tions, which are dependent on the strain in the model. The bilinear composite layer should be incorporated such that it facilitates the second bending mode. Therefore, the first bending mode should be such that the bilinear composite is elongated. This first deformation mode should proceed until the elongation is large enough for the strain transition point of the composite to be reached. Once this point is reached, the stiffness provided by the now decrimped paper layer dominates over the stiffness provided by the opposite edge of the deformed actuator. This swing in stiffness forces the deformed state to change direction as the internal pressure continues to increase.

The bilinear composite has a thickness of 5 mm. Even whilst still crimped, the composite offers stiffness to the initial displacement response of the actuator. To ensure there is indeed a preferential initial bending mode, the side opposite to the bilinear material needs to be stiffer up until the strain transition point is reached.

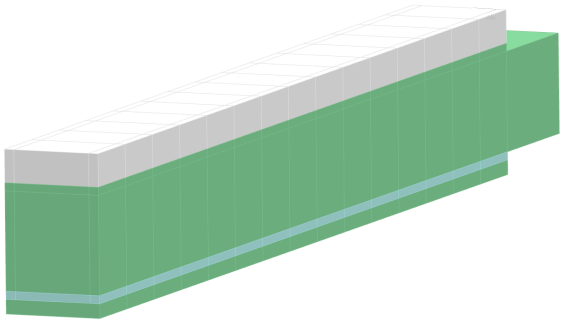

Figure 3.12: Isometric view of the bimodal actuator showing the Mold Star 15 in green, the bilinear material in white and the Smooth-Sil in blue

3.3.2 Physical Model

Moulds to manufacture the physical model were designed such that changes to the geometry were easily facilitated. Instead of casting the different actuators with different sets of moulds, the baseline geometry was rather used to which additional thin strips could be glued to achieve different results. These additional strips allowed the response to be rapidly changed without the delay of waiting for new moulds and were available in 1, 2, and 3 mm thicknesses. The bilinear composite was glued to the Mold Star 15 body using Smooth-On Sil-Poxy. To prevent the base material of the bilinear composite, the soft Ecoflex 0030, from directly being subjected to high pressures, a 1 mm strip of Mold Star 15 was glued to the bilinear material at the interface to the main actuator body, visible in Figure 3.12. The Ecoflex would have bulged substantially if directly subjected to the pressure required for the actuator to function as designed.

The actuator was clamped at the base and inflated using a medical needle inserted through the base into the first void. During testing it was hung down vertically to mitigate the effect of friction between the actuator and a flat surface. A checkerboard pattern with blocks spaced 2.5 mm apart was used to quantify deformation. A camera was attached to a tripod and used to take photos while the actuator was inflated. The internal pressure was controlled using a manual pneumatic pressure regulator and photos taken at 5 kPa pressure increments. The tip displacement was calculated

during post-processing by counting the blocks between the deformed state and reference state of the actuator. A sequence of this response to a pressure increase is available in Figure 3.13. The actuator tip that was tracked during the incremental pressure increases is shown as a red dot in the sequence. The pressure was increased until rupture occurred. Further details are available in Appendix B.

3.3.3 Numerical Development

The numerical model was developed as a FE model using Siemens NX12 and the multi-step nonlinear kinematic solver `SOL402`. A 3D model was constructed using linear hexahedral brick elements using material properties from Appendix A. A node corresponding to the position of the tip tracked in the physical test was selected and the displacements exported at completion of the simulation.

3.3.4 Results and Discussion

To demonstrate the use of the bilinear material and the extent to which that translates to a bimodal behaviour, the three different bilinear crimp ratios available were used. These design parameters should allow actuators to have distinctly different modes depending on whether the internal pressure has exceeded the transition pressure or not.

Figures 3.14-3.16 show the numerical and physical results for each crimp ratio as the pressure increases.

Disregarding the discrepancy between the physical and numerical models, the main objective of bimodal behaviour in an SPA has been achieved using both modelling techniques. In all three cases, the actuator has a preferential bending direction that changes according to the internal pressure. By varying the crimp ratio of the bilinear composite, it was further possible to alter the pressure at which this preferential direction changes as well as the magnitude of the maximum tip displacement achieved.

The 0.3 crimp ratio composite essentially has the longest strip of paper embedded of the three composites manufactured. This translates to the highest tip displacement (81.25 mm) in the initial bending direction out of the three actuators tested. In comparison, the 0.2 crimp ratio has the short-

est embedded paper layer which translates to the lowest tip displacement in the initial bending direction (17.5 mm), but the highest tip displacement in the secondary bending direction (65 mm). The crimp ratio therefore has a large impact on the tip displacement possible for each of the bending directions for a given pressure.

The large discrepancies evident between the physical and numerical models in terms of X-Y displacements and pressure magnitudes will need further investigation. Numerous possible causes exist which primarily revolve around the bilinear material: the material model incorrectly captures the strain transition point; parameters that are possible to measure on an homogeneous sample of silicone, such as bulk modulus, are difficult to characterise on the bilinear material; the material model is overly stiff after the transition point. Ways to mitigate these problems are listed as future work in Chapter 8.

The focus of this chapter revolved around demonstrating the ability to include a bimodal behaviour into a SPA. The trial-and-error approach suited this outcome as the results did not require a high degree of accuracy. The succeeding chapter investigates an approach where more control over the inflated shape is possible when using a modular actuator. This approach requires more accuracy, predictability, and a means to automate the design process.

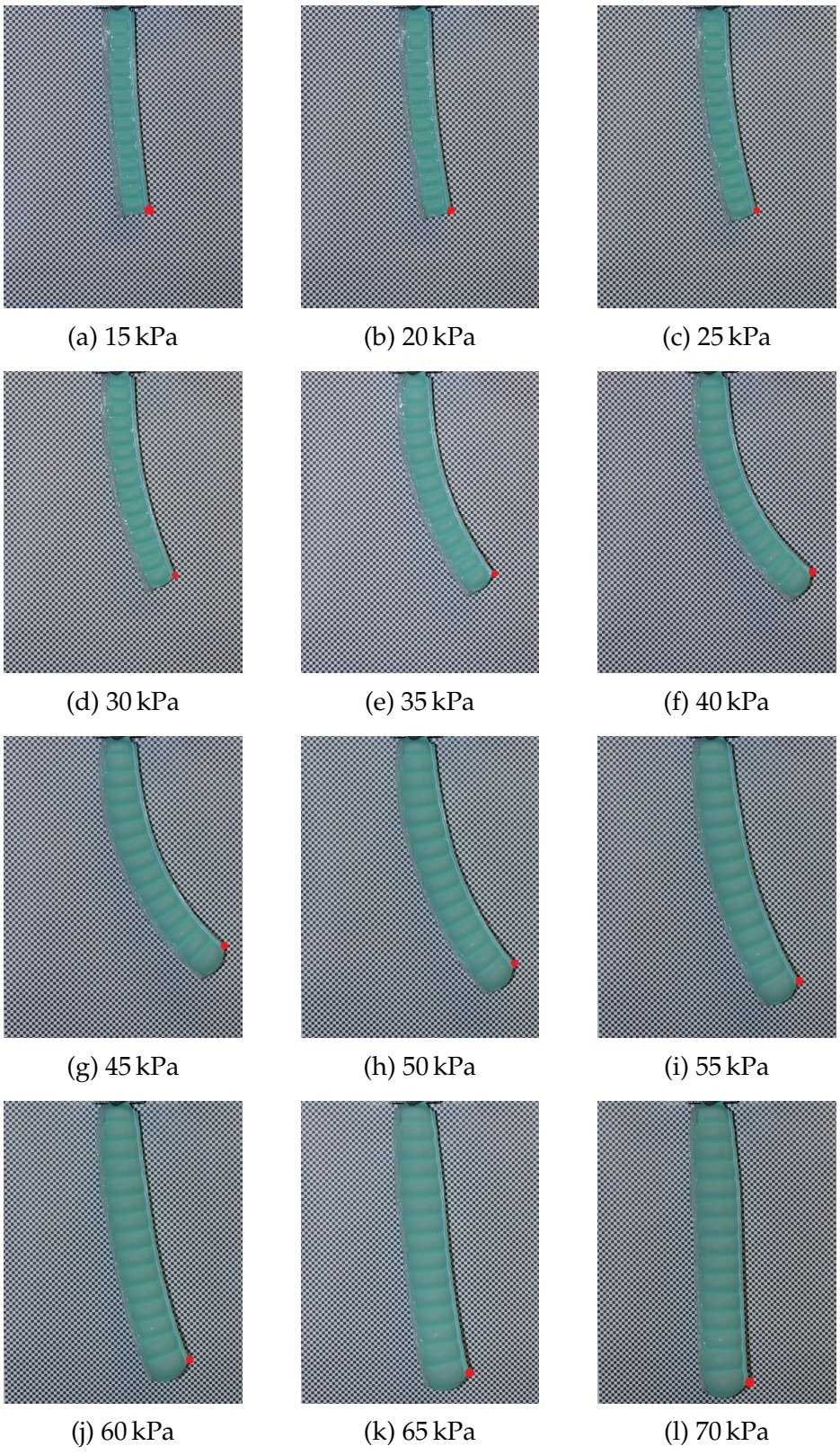

(a) 15 kPa (b) 20 kPa (c) 25 kPa

(d) 30 kPa (e) 35 kPa (f) 40 kPa

(g) 45 kPa (h) 50 kPa (i) 55 kPa

(j) 60 kPa (k) 65 kPa (l) 70 kPa

Figure 3.13: Sequential steady-state photos of the bimodal actuator as pressure is increased (Crimp ratio = 0.3). The red dot indicates the tip position tracked during post-processing

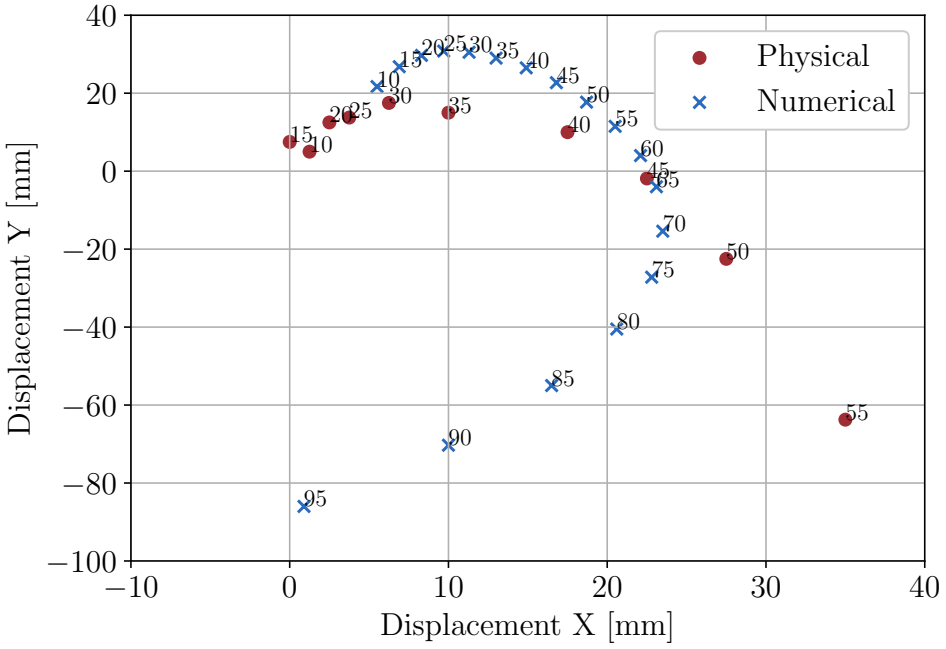

Figure 3.14: Tip displacement using a crimp ratio of 0.2 (Incremental pressure values indicated in kPa next to each point)

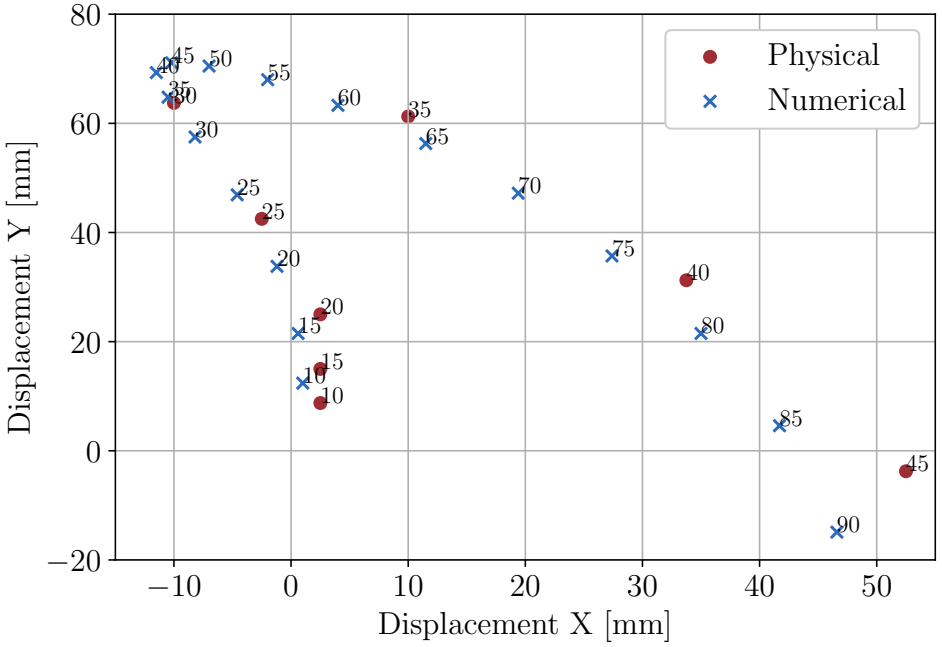

Figure 3.15: Tip displacement using a crimp ratio of 0.25 (Incremental pressure values indicated in kPa next to each point)

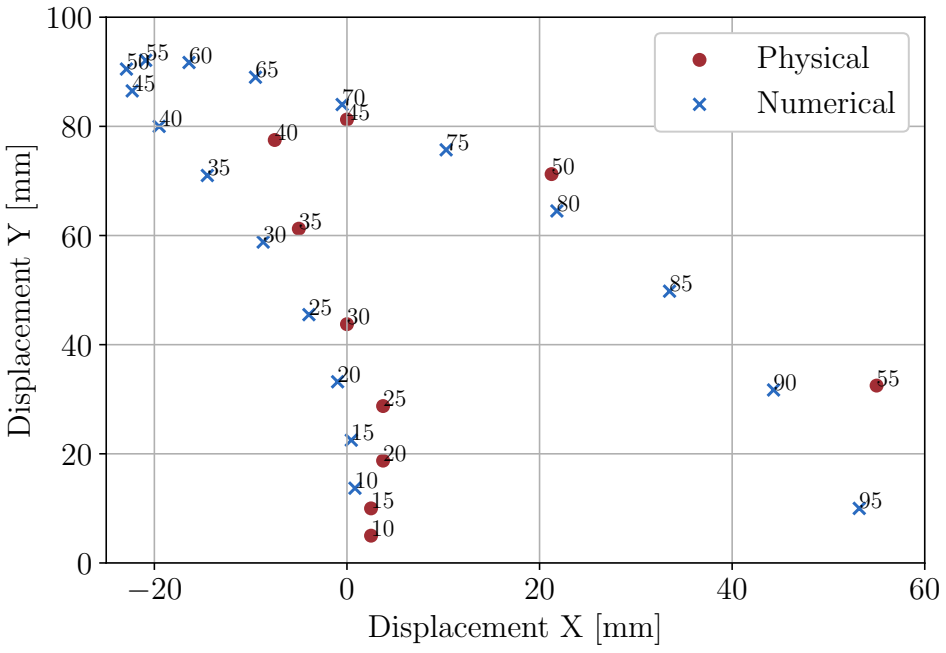

Figure 3.16: Tip displacement using a crimp ratio of 0.3 (Incremental pressure values indicated in kPa next to each point)

Chapter 4

Evolutionary Design Methodology and Actuator Construction

This chapter is a reproduction of a conference paper titled 'Computational Design for Inflated Shape of a Modular Soft Robotic Actuator' Ellis et al. (2019). The paper is co-authored by my supervisors Dr Martin P. Venter and Prof. Gerhard Venter of the Department of Mechanical and Mechatronic Engineering at the University of Stellenbosch, South Africa. Their contribution was as a supervisory role.

Being able to explore the design space available to soft robotic actuators is the driving force behind developing the proposed design methodology. The use of soft, nonlinear hyperelastic materials, typical in soft robotics applications, and the anticipated large displacements require the use of a multi-step numerical modelling tool resulting from typical operation. To perform this task, a genetic algorithm (GA) is coupled with Siemens NX 12 (Siemens NX12, 2017) pre-processor and Siemens Nastran implicit, nonlinear kinematic solver `SOL402` to evaluate designs and make changes to the modular actuator. This chapter shares the flow charts of the different facets used in order to design an actuator that best matches the desired profile and is capable of being expanded using different articulating building blocks.

4.1 Actuator Construction

A method is proposed here where the modular characteristic often seen in soft robotic actuators can be exploited. Each actuator is constructed by means of the repetition of a parametric modular unit capable of asymmetric

inflation. By designing this unit to have a preferential bending direction and combining them in series it is possible to get a range of different actuators by simply changing the orientation of each unit in sequence. The quantity of units to use is determined by the desired total length of the actuator.

It is important to note that for the numerical design work, no provision is made to ensure continuity between the adjacent inner voids. This was done to simplify the geometry and meshing of the numerical models. The effect of this simplification is investigated in Appendix D. It was found to result in a 4.5 % and 6.5 % error for X and Y-displacements, respectively, when inflated to the maximum working pressure. For the physical model this was however addressed by removing a small section of material from the walls that connect the units together.

4.2 Articulating Unit

The designed articulating unit does not use a thin paper membrane strain limiting layer, as is common practice for soft actuators (Polygerinos *et al.*, 2013). Rather, a bias in material thickness and silicone stiffness is relied on to create a preferential bending direction. This preferential bending direction can be utilised by switching the orientation of individual units by 180°. The softer Mold Star 15 is used for the main body of the unit with a thicker strip of stiffer Smooth-Sil 950 to create the bias in material thickness and stiffness. A section view of a single unit is shown in Figure 4.1 where all wall thicknesses are 1.5 mm, apart from the Smooth-Sil thickness which is 3 mm. The first unit, at the base of the actuator, is swapped out for a unit as in Figure 4.2. This extra block of silicone simplifies the experimental testing of the actuator by allowing a small needle to be pierced into the first void area without allowing air to escape. To simplify the numerical model, this additional block of silicone was ignored in the modelling. Further details are available in Appendix D. Figure 4.3 shows a cross-sectional view of an assembly of units that form a full-length actuator.

The maximum pressure that each unit is able to withstand is greatly dependent on the minimum wall thickness and was established by trial-and-error using physical models. It was found that 45 kPa could be sustained for prolonged periods when using a 1.5 mm wall thickness and Mold Star 15.

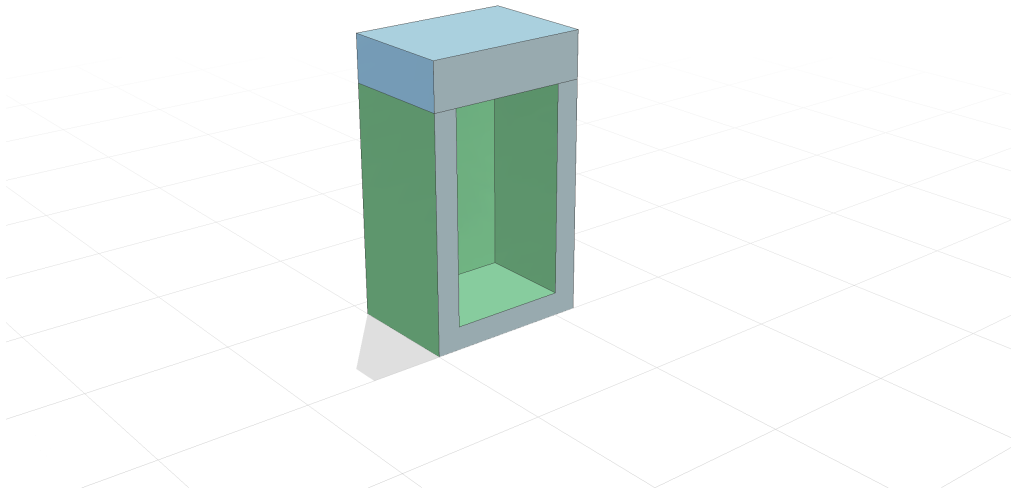

Figure 4.1: Cross-sectional isometric view of the articulating unit (Shown with Mold Star 15 in green and Smooth-Sil 950 in blue at the top)

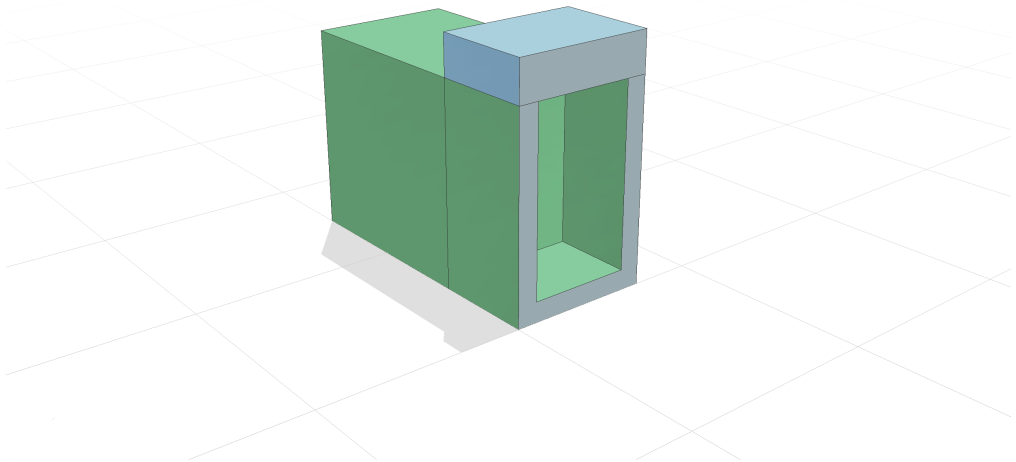

Figure 4.2: Cross-sectional isometric view of the articulating base unit (Shown with Mold Star 15 in green and Smooth-Sil 950 in blue)

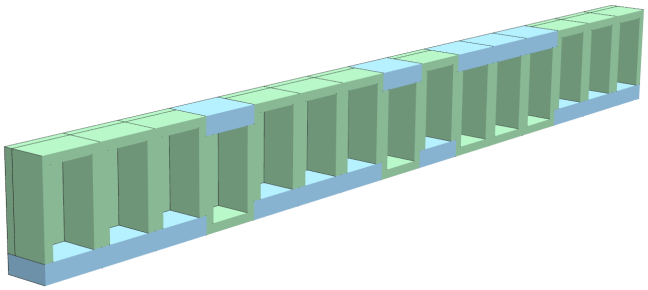

Figure 4.3: Assembly of units that shows an actuator with a random orientation vector

4.3 Enabling Varying Pressure

For additional accuracy at matching the desired profile, it was required to utilise a varying pressure in the models in lieu of always using the maximum available pressure. Two different methods exist to achieve this:

1. Specifying discrete pressure variables and using these as the maximum pressure in the model.

2. Utilising the nature of implicit nonlinear FE solvers and the increments in which the models are solved.

Method 1 involves adding extra information to each individual in the population. This information will have to be added to the orientation vector, but will need to act independently thereof. A key between the information in the vector and how that decodes to a pressure magnitude will be required. Individuals will therefore be calculated at different maximum pressures and that value can then be used in calculating the fitness value. This method is computationally more expensive and also very inefficient in the way it utilises already calculated information.

Method 2 utilises the converged results for every increment in the FE solver. These increments correspond to increments in the applied pressure loading. For one simulation result it is then possible to extract displacement information at a multitude of intermediate pressures. Preliminary testing proved that the numerical models can be solved using ten incre-

ments. Where a smaller step size is required for convergence, numerical cut-back is allowed, but these results are not added to the `.pch` file that is exported. The benefit of this is that a very structured output file is generated irrespective of how many cut-backs were required to solve the model. At no additional computational cost, a more efficient optimisation procedure can be run and converged results at different pressures extracted.

4.4 Genetic Algorithm

The problem that needs solving is the combination of orientations for each unit in the actuator. Genetic algorithms (GA) (Goldberg, 1989) excel at solving such combinatorial problems. A GA is an optimisation algorithm based on natural selection and Darwin's principle of survival of the fittest. Three types of bio-inspired operators are used to create the next generation from the current population:

1. *Selection* – The rule which chooses individuals (*parents*) from the population for later breeding

2. *Cross-over* – Also known as recombination; it combines genetic information of two parents by determining what genetic information a *child* will inherit from which parent.

3. *Mutation* – The operator used to maintain genetic diversity by randomly applying changes to *parents* while forming *children*

Additional operators such as *Elitism* exist where the top performing individual throughout the optimisation remains to ensure that their genetic information is retained.

An initial population of random candidate individuals is evaluated to determine the top performing or fittest individual using an objective function. Parents are then selected for reproduction, with the top performing individuals having a higher probability of being selected. This process is repeated over multiple generations and the population is allowed to evolve better performing offspring. Each unit and the orientation of that unit has a unique number i.e. a unidirectional bending unit is either 0 or 1 depending whether it is flipped with 180°. These numbers are stored in what is

termed the orientation vector in this research – the vector containing the information regarding the specific units, their orientation as well as the order in which they appear. Optimising this orientation vector forms the basis of this methodology. At conclusion of the optimisation a number of top performing individuals should be available for scrutiny by the user.

The proposed design methodology relies on solving a combinatorial problem using articulating building blocks in order to get the desired deformation. The articulating unit presented in this chapter is not the focus of the overall research – it merely serves as a means to achieve the actual objective of an actuator where the behaviour can be prescribed. Nevertheless, interesting and unique designs should be possible. The ability to mechanically pre-programme behaviour into a design is a distinct characteristic of soft robots which is exploited and developed in this section.

4.5 Automation

Every individual that requires an evaluation of its fitness requires that a nonlinear FE model be created, solved, and post-processed. Genetic algorithms typically require population sizes and number of generations which make this process infeasible to be performed manually. An automated procedure was required to improve repeatability between the models and reduce overall optimisation time.

A Python script was coded that runs the GA using the eaSimple implementation as presented in Chapter 7 of Back *et al.* (2000), available within the Distributed Evolutionary Algorithms in Python (DEAP) (Fortin *et al.*, 2012) library. A flow chart is provided in Figure 4.4 that schematically shows the work process where nonlinear FE models are created, solved, and the performance thereof evaluated during a fully automated loop implementing the GA. The superior scripting abilities (keyword: *Journal*) of Siemens NX 12 made it the go-to software package for this research. Different individual functions were coded that perform the various tasks required to make a fully automated loop, the names and functionality of each are discussed in this section in the order that they are called.

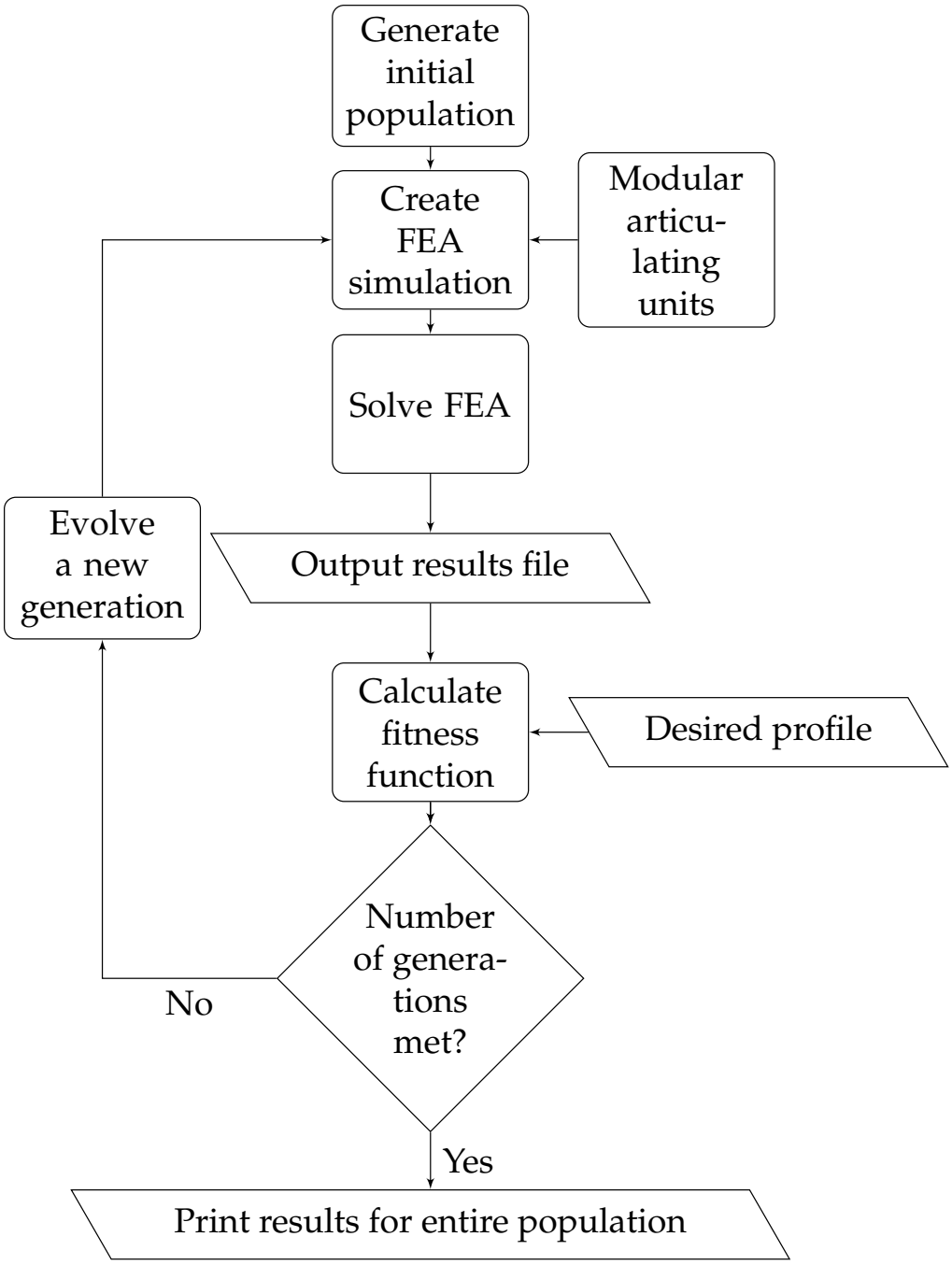

Figure 4.4: Work flow chart that implements the GA

4.5.1 Function `mainScript`

This function serves as the main script from where the GA parameters are set and all the different functions are called. The length of the actuator is input by specifying the number of units to use, the maximum pressure which should be considered, the population size, number of generations required by the GA, and a file name for the optimisation run. The DEAP toolbox uses this information and creates an initial population of individuals that have randomly generated orientation vectors. The GA optimises these orientation vectors based on the performance of every individual. This is done by calculating the fitness value; essentially the error between the desired profile and the deformed shape of the current actuator being analysed.

4.5.2 Function `profile`

The desired shape of the inflated actuator is specified in this function. This can be done via one of two different methods:

1. A description of the final position of the actuator's tip either as an instruction i.e. maximum horizontal displacement, minimum vertical displacement, maximum curl, etc.

2. A continuous mathematical function which takes the entire centreline of the actuator into consideration. This mathematical function should be able to uniquely describe each point on its path. Both a Cartesian and polar coordinate system suffice, with the former being the simplest method.

4.5.3 Function `generateJournal`

The performance of every individual needs to be established in order to compute the fitness value. NX 12 allows for the articulating units to be created independently with all the relevant material and mesh properties stored along with it as a `.fem` file. A Python script was coded that can recreate the Journal file used by NX 12 to assemble these articulating units, apply all the boundary conditions and pressure loads to the cavities, set up the parameters required for `SOL402` and submit it to solve. This Journal file can be

set up in various programming languages. Python was selected for consistency with the different code written throughout this research.

To create the initial Journal, the tasks that are required to be performed by it must be recorded while the user performs them using the graphical user interface, just as one would without the keystrokes being recorded. Two methods of modifying the Journal then exist. The simplest method is using the commands already native in Python to manipulate how the code is executed. This method is however restrictive. The more cumbersome, but powerful method is to create a new Journal file tailored to every individual. A Python script was created that can read and edit Journal snippets to perform the various tasks required in the FE analysis. These snippets are then combined into a larger file using the correct syntax and libraries that constitute a fully capable and working Journal. This method results in cleaner Journals tailored to a specific individual, thereby mitigating unnecessary actions and lines of code and providing more possibilities to expand the code. This method scales easily to longer actuators. The tailored Journal is run to create the FE analysis model.

This function receives the orientation vector, maximum allowed pressure, and file name as inputs. It then runs through a process of reading and modifying various snippets of existing code to create the actuator required. These modifications are written to one Journal for every individual.

4.5.4 Function `evalFitness`

At the GA's prompt to calculate an individual's fitness, the data deck for that FE model is written and submitted for solving in the foreground. This solution takes place in a new subdirectory created within the current working directory for every individual and generation. This additional directory ensures that results from previous runs cannot unknowingly be used in the process. A solution problem will lead to no results being available within that directory and lead to an error flag being raised. At completion, the nodal displacements for every increment of the solution are exported as a punch file. `punchToArray` is called and the returned arrays containing the X and Y displacements used to calculate the fitness value. The fitness metric required for the GA is calculated using the tracked displacements of the individual and its deviation from the desired shape specified at every solution

increment. The number of solution increments is fixed at ten for this project. The displacements of the individuals are tracked at the four nodes spaced an equal distance from the outer edge for each of the modular units. Figure 4.5 shows an example of the location for one of these units. The average of these four separate nodes is calculated for Y-displacements, essentially calculating the centre height of the void area. The error between the desired profile and the current actuator is used as the fitness metric, F_f, and is calculated as:

$$F_i^f = \sqrt{\sum \left[(Y_i^{desired} - Y_i^{actual})^2 \right]} \tag{4.1}$$

where Y_i is a vector with the superscripts referring to displacements of the desired profile and those of the actual actuator for which its fitness is being calculated, and the subscript used to denote each of the ten increments for which the nonlinear solution is solved. The fitness metric is therefore calculated individually for each solution increment and stored as an array.

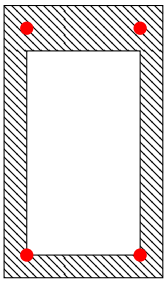

Figure 4.5: Cross-sectional representation of a modular articulating unit. The red dots indicate the vertices of the void region which are the nodes of which deformation is tracked for further calculations

4.5.5 Function `punchToArray`

Punch files (`.pch`) exported from Nastran are structured ASCII files that contain only the specific information requested for export – nodal displacements in this instance. The convenience working with these files is that only the nodes of concern can be written to them resulting in small, compact files. Tools exist to process the binary results file (`.op2`), but the drawback is that these contain all the simulation results, resulting in a potentially large file leading to higher computational costs involved with post-processing. A

function was written that imports this punch file, reads through all the lines of text, and extracts the X and Y displacements for each of the nodes, for each of the ten solution increments. These results are returned as NumPy arrays.

4.6 Mesh Refinement of 3D model

A mesh refinement study was performed on an actuator with all of its units orientated in the same direction. The coarsest possible mesh is where one element is used through thickness i.e. 1.5 mm edge length of a hexahedral element. The mesh was refined by increasing the number of through thickness elements on the thinnest wall section. The meshes investigated therefore had one, two, three or four hexahedral elements though the thickness with edge lengths of 1.5 mm, 0.75 mm, 0.5 mm, and 0.375 mm, respectively. These element sizes were evaluated using linear 8-node element formulations and an actuator inflated to 45 kPa using only eight units, Figure 4.6. This reduced actuator length was used to allow the models with finer meshes to be solved on a desktop computer in a reasonable time. Apart from the reduced actuator length and element sizes, these models are identical to those used throughout this chapter. The constraints used are shown in Figure 4.7.

The 1.5 mm element size was evaluated using a quadratic 20-node element formulation as well. Solution time for each model is presented in Table 4.1 where models were solved using an Intel i7-4770 CPU at 3.4 GHz.

Table 4.1: Solution time during mesh refinement

Mesh details	Solution time [s]
1.5 mm, 8-Node	173
1.5 mm, 20-Node	590
0.75 mm, 8-Node	1466
0.5 mm, 8-Node	7032
0.375 mm, 8-Node	60370

It proved difficult to conduct a quantitative analysis of the performance of each mesh. In this work the overall deformation shape of each actuator is of concern. As such, the analysis will be qualitative. The coarsest mesh with

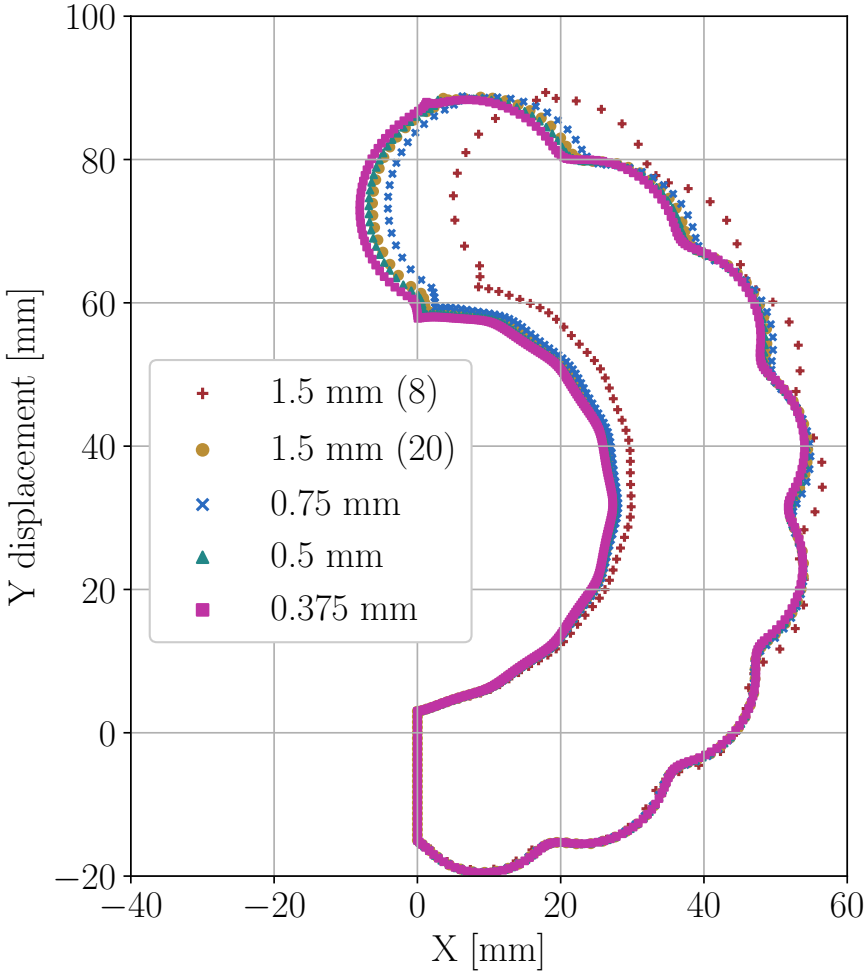

Figure 4.6: Mesh refinement of shortened (8 units instead of 15) 3D model using different element sizes and formulations. All units are orientated in the same direction and the actuator is inflated to 45 kPa

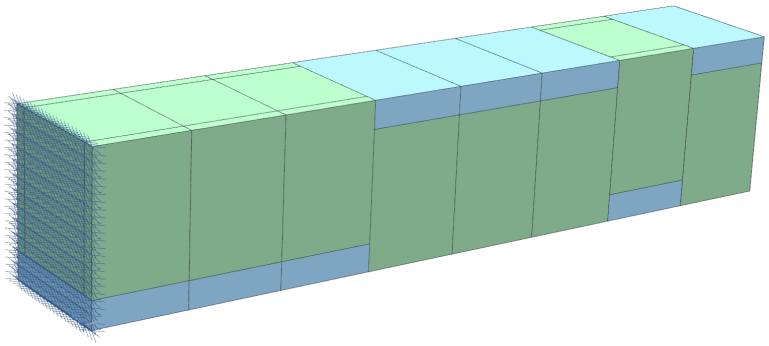

Figure 4.7: Fully fixed constraint shown on the reduced length actuator used during the mesh refinement study

the lowest quantity of nodes solves in the shortest time, but also yields the least deformation. Decreasing the element size delivers more deformation, albeit at an increased solution time. The mesh appears converged for element sizes less than 0.5 mm, but these require run times in excess of 2 h. A trade-off between accuracy and time is required. The 1.5 mm elements and a 20-node formulation approximates the values of the converged mesh at a much quicker run time. The quadratic 1.5 mm element is thus used for all further work.

4.7 Computational Resources

Using a design algorithm that performs an iterative search through the available design space requires that a multitude of simulations be solved. The nature of nonlinear FE analyses is to solve the model in incremental, smaller, and linear steps, therefore adding to this computational cost. The design algorithm in this chapter only requires displacement values from the numerical simulation as the pressure at which failure occurs was experimentally determined. Strain values from the model are therefore not required. This sole dependence on displacement information allows that a computationally cheaper means of accurately approximating it can be investigated, even if it requires certain non-realistic features. A reduced order model is researched to this end.

Chapter 5

Reduced Order Modelling

This chapter is a reproduction of a conference paper titled 'Computational Design for Inflated Shape of a Modular Soft Robotic Actuator' Ellis et al. (2019). The paper is co-authored by my supervisors Dr Martin P. Venter and Prof. Gerhard Venter of the Department of Mechanical and Mechatronic Engineering at the University of Stellenbosch, South Africa. Their contribution was as a supervisory role.

Depending on the population size and number of generations in a genetic algorithm (GA), the number of individual actuator simulations for which a fitness metric needs to be calculated can lead to prolonged optimisation run times if no attempt is made to curb it. The level of detailed information obtained from 3D numerical models is largely excessive for the purpose of this research and comes at the cost of prolonged run times. Since an iterative approach will be followed as part of the design methodology, it is imperative to reduce the time required for each function evaluation required as part of the fitness evaluation. As such, a means of reducing the 3D model to a 2D planar case was investigated and is presented in this chapter. The reduced order model is used as a means to save on computational costs whilst approximating the results of the 3D model.

5.1 Simplified Model

A starting point for this investigation was to merely determine the response that the cross-section would have as a 2D model. This simplification takes into account the varying thickness of each modular unit around the void region in the centre. Fifteen of these units were connected in series with a

random orientation vector. A plane-strain model of this simplification was created in NX 12 using SOL402. The calculated displacements from this 2D simplification were compared to those from a 3D model of identical unit orientation.

Figures 5.1a and 5.1b show the difference in displacement for the two models. These figures show that the 2D model undergoes significantly more deformation and that the final deformed shape poorly represents that of the 3D model. The reinforcement offered by the solid sides on the 3D model therefore creates an actuator that is much stiffer than what the simplified 2D model can match. A method of efficiently adding extra stiffness to the 2D model is required.

5.2 Equivalent Model

To achieve a better correlation between the 2D and 3D models, an additional linear isotropic material is added to fill the available void section of the 2D model. Using an optimisation procedure implemented in Design Optimization Tools (DOT) from Vanderplaats Research &, Development Inc (a general-purpose gradient-based optimisation library) and a custom Python script, the isotropic stiffness that gave the best correlation with 3D results was identified. A schematic of the work flow that is implemented in the script is given in Figure 5.2.

The objective function for the optimiser is calculated as the squared nodal displacement error between the 2D and 3D models:

$$minimize : \Gamma = \sum \left[(\bar{X}_2 - \bar{X}_3)^2 + (\bar{Y}_2 - \bar{Y}_3)^2 \right] \tag{5.1}$$

where $\bar{X}$ and $\bar{Y}$ refer to the averaged x- and y-displacements of the four nodes exported for each modular unit, as in Figure 4.4. Subscripts 2 and 3 distinguish between the 2D and 3D models. The average of these four nodes therefore calculates the centre point of the deforming unit. The error is calculated using displacements from each of the units along the length of the actuator at the final increment.

An actuator length consisting of fifteen modular units was used to calculate the stiffness of the filler material. The loads and boundary conditions used are shown in Figure 5.3. The pressure is equally applied outward to

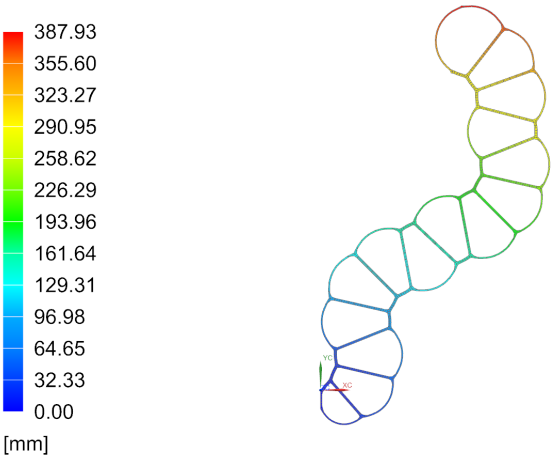

(a) Simplified 2D model

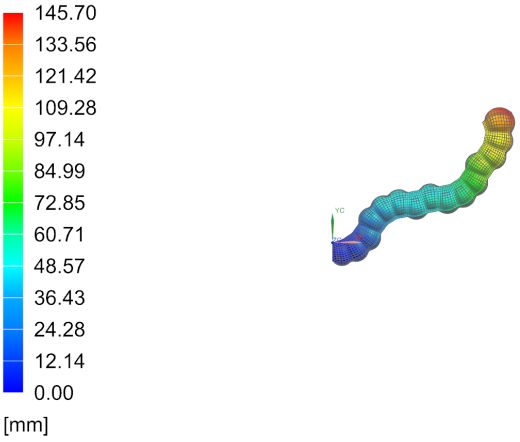

(b) 3D model

Figure 5.1: Magnitude of displacement for an actuator with the random orientation vector for both a 2D and 3D model, inflated to 45 kPa. Scaling is kept constant between models. The 2D model appears much larger due to its higher compliance.

the four vertices which forms the void of each unit. A fully fixed constraint is applied to the outer edge of the base unit. An optimisation procedure was set up to calculate the required stiffness at pneumatic pressure increments of 5 kPa over the range 5 kPa–45 kPa. For each pressure increment a new random orientation vector was generated and a random initial starting point was used. This complete optimisation was run three different times

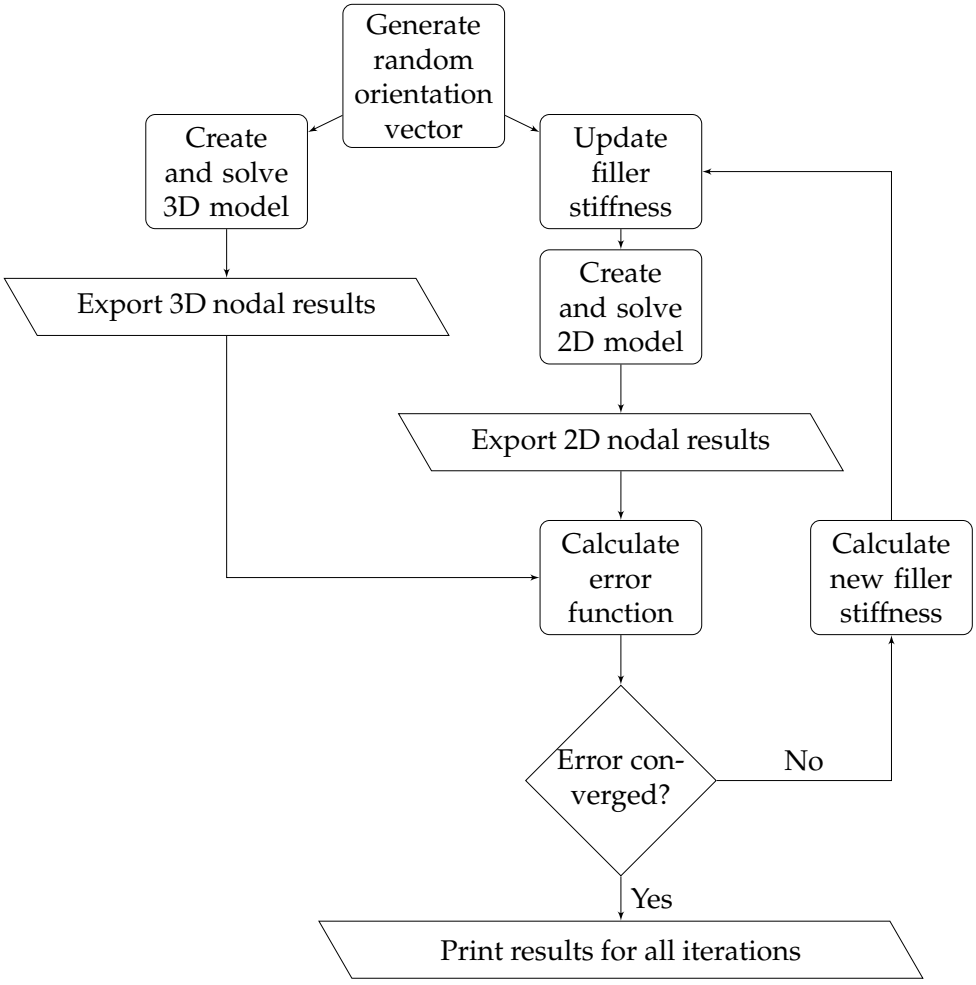

Figure 5.2: Work flow chart to calculate the material filler stiffness with DOT

to minimise local minima from skewing the results. Figure 5.4 shows the results from these different runs along with two different least-squares regression fits used to model the behaviour. The R^2 value for these two fits are shown in the figure legend and distinction is made from the different optimisation runs using the acronym of the optimiser used - DOT.

Results from the three different runs all show a similar trend where required stiffness reduces as the inflation pressure increases. No obvious outliers were converged to. Based on the R^2 value, the quadratic fit models the data much better than the linear fit and was therefore the chosen model. There is no extra cost (computationally, or input complexity) involved to implement a quadratic model over that of a simpler linear model in the software. This model therefore acts as a smeared response between the three different sets of results calculated and is represented as

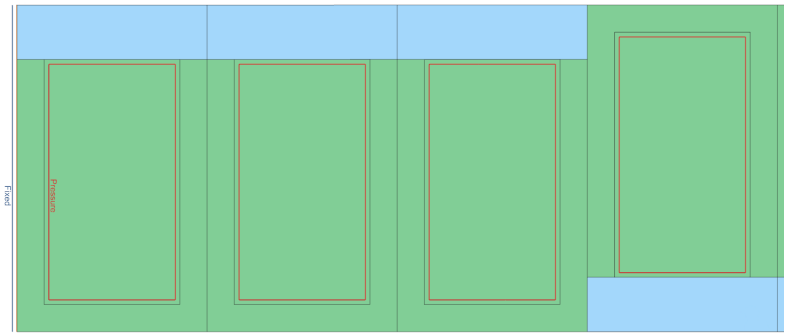

Figure 5.3: Fully fixed constraint and internal pressure loading shown on the reduced order 2D model. The additional linear isotropic material added to the void region is the area encapsulated by the red rectangle.

$$E = 0.0643 - 1.82P + 12.4P^2 \tag{5.2}$$

with pressure in MPa.

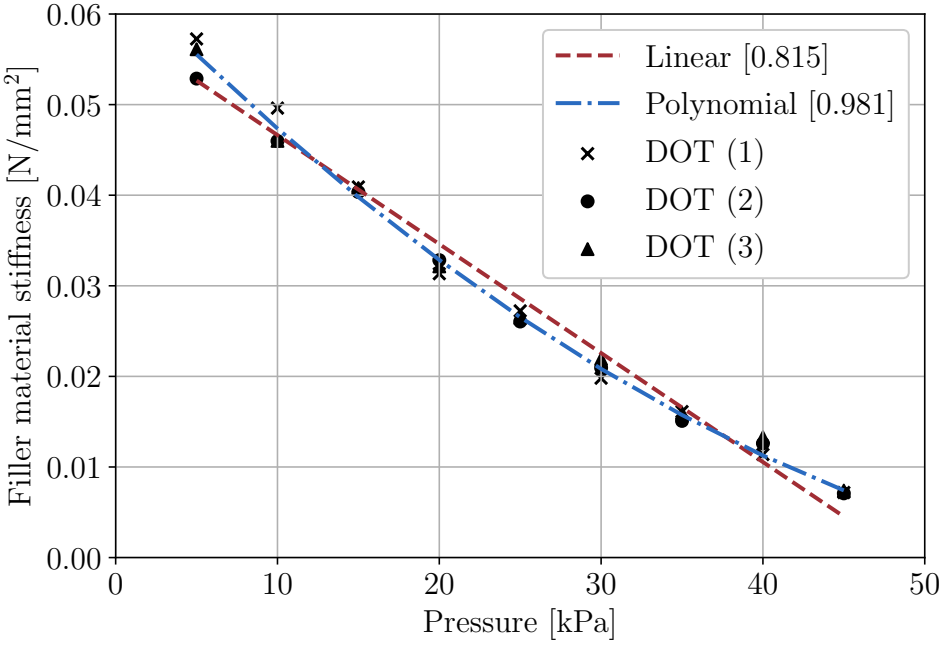

Figure 5.4: Relationship of filler material stiffness to internal actuator pressure as shown for three independent runs using DOT and random orientation vectors

The sensitivity of the reduced order model to changes in this stiffness value was investigated. For this, the same orientation vector as used in Figures 5.1a and 5.1b was used. The 2D simulations were run and displacements calculated at a pressure of 45 kPa using the three different results calculated using the optimiser as well as the prediction at that pressure using the quadratic model. These results are shown along with the 3D displacements in Figure 5.5. The added accuracy achieved with the addition of the filler material is evident by all the lines having similar profiles and displacements. Investigating the performance of the quadratic model against the 3D model by calculating the distance between similar nodes, the two models vary on average with 4.32 mm along their length. For the orientation vector investigated, the model does not appear too sensitive to small changes in the stiffness value of the filler material as small errors are computed and profile shapes appear similar.

Although the 2D mesh was calibrated on results from the 3D model, a mesh refinement study was still performed. The reduced order model was constructed using square plane strain elements. The coarsest mesh that fits within the geometry, required elements measuring 1.5 x 1.5 mm each to represent both the silicone and the filler material, Figure 5.7. This element size was reduced to 0.75 mm and the impact on the results measured. To quantify the contribution of the mesh to the final results, an identical procedure was followed as used to calculate the stiffness of the filler material. Three independent optimisation procedures were run using random orientation vectors and a polynomial function fit through the results. Figure 5.6 shows this best fit polynomial along with the function calculated using the coarser mesh from Figure 5.4. These results show very little deviation from one another and the conclusion can be made that the coarse 2D mesh using the 1.5 mm elements is converged. This performance justifies that the reduced-order model is accurate enough to proceed with the design optimisation phase.

The full 3D model of a modular unit has 408 elements and 3 635 nodes, whereas the reduced order 2D unit has 84 elements and 366 nodes. This reduction in nodes reduces the average runtime from 590 s for a 3D model to 45 s for the final reduced order model using 15 articulating units. These simulations were performed on a computer running a 3.4 GHz Intel Core i7

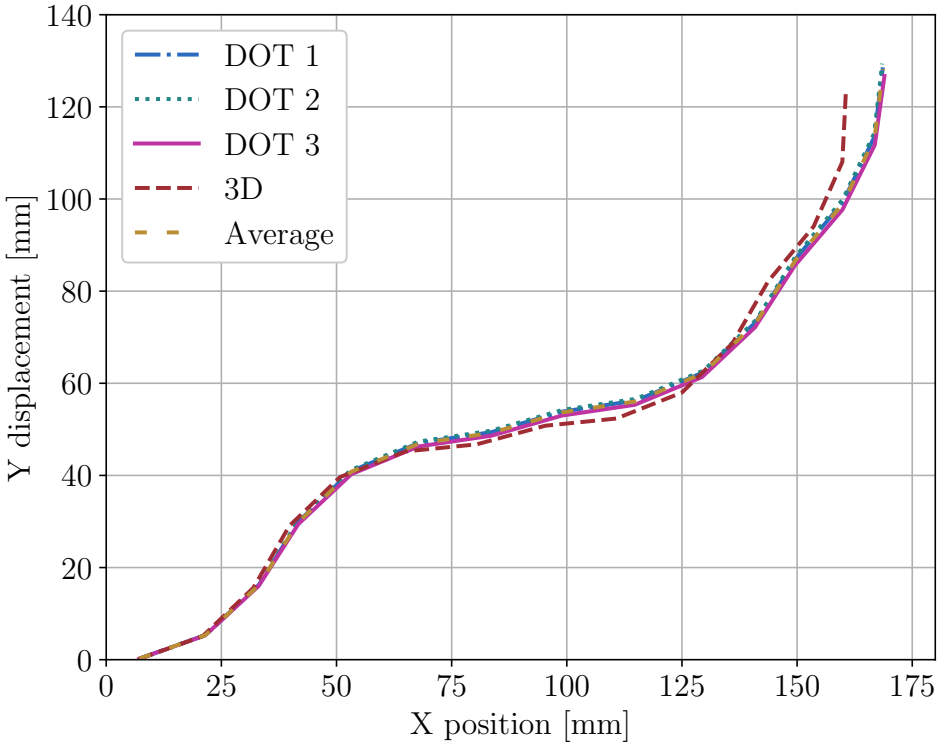

Figure 5.5: Sensitivity of actuator to changes in the stiffness of the filler material. Profiles are shown for three different optimisation runs, a quadratic function (Average) modelling those results and the displacements from the 3D model, all at 45 kPa

CPU and 12 GB of RAM.. The solution times include creating the Journal, solving the model and waiting for the `.pch` file to be written.

The use of a hyperelastic material model requires the use of a Green strain and Second Piola Kirchoff stress formulation. Without enabling this calculation method, the models are prone to encounter convergence issues that stem from element failure.

5.3 Incremental Pressure Dependent Equivalent Model

In order to utilise the method of a varying pressure load described in Chapter 4, it is required that the converged incremental results in the FE analysis

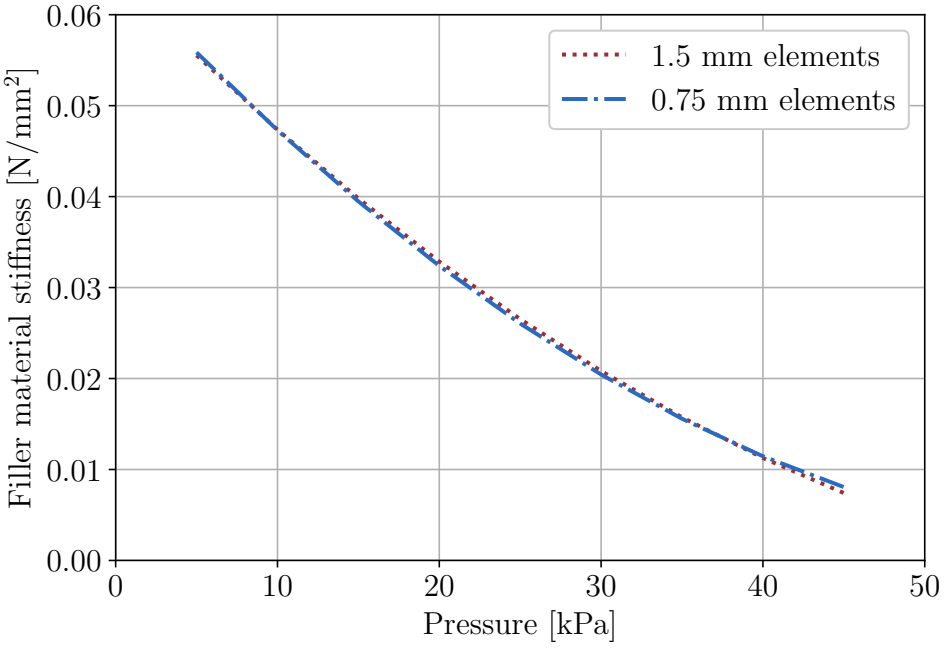

Figure 5.6: Effect of mesh refinement on the required pressure-dependent stiffness of the 2D filler material

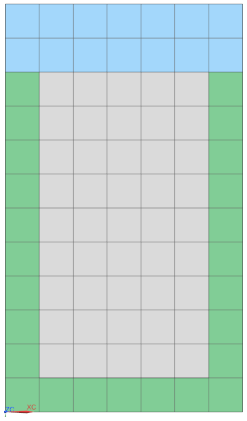

Figure 5.7: Close-up of the mesh used for a single modular unit with the filler material shown in gray

be accurate for all intermediate pressures. The stiffness of the filler material, which is pressure dependent, needs to be added to the FE model so that it can be updated for the different incremental pressures. However, NX 12 does not allow a material property to explicitly be linked to internal pressure. The only variable on which a material property can be dependent is temperature. This does allow for a work around, explained in detail in Appendix D, where a fictitious temperature is added that is linked to the solution time. The quadratic model in Figure 5.4 is adapted to be temperature dependent and is linked to this temperature variable. The result of this work-around is shown in Figure 5.8 for the orientation vector used previously. The effect is shown when using a constant filler stiffness as required for the maximum pressure versus the approach of incrementally updating the stiffness value. The final position of both curves line up as they use the same stiffness value. A large disparity exists between profiles at similar pressures, but using the two different filler stiffness values. When tracking the two profiles from their initial state, it can be seen that the profiles solved using a constant stiffness value have more deformation for a similar pressure than for the varying stiffness value. This agrees with what is expected seeing as the varying stiffness value starts with a higher value at the low pressures.

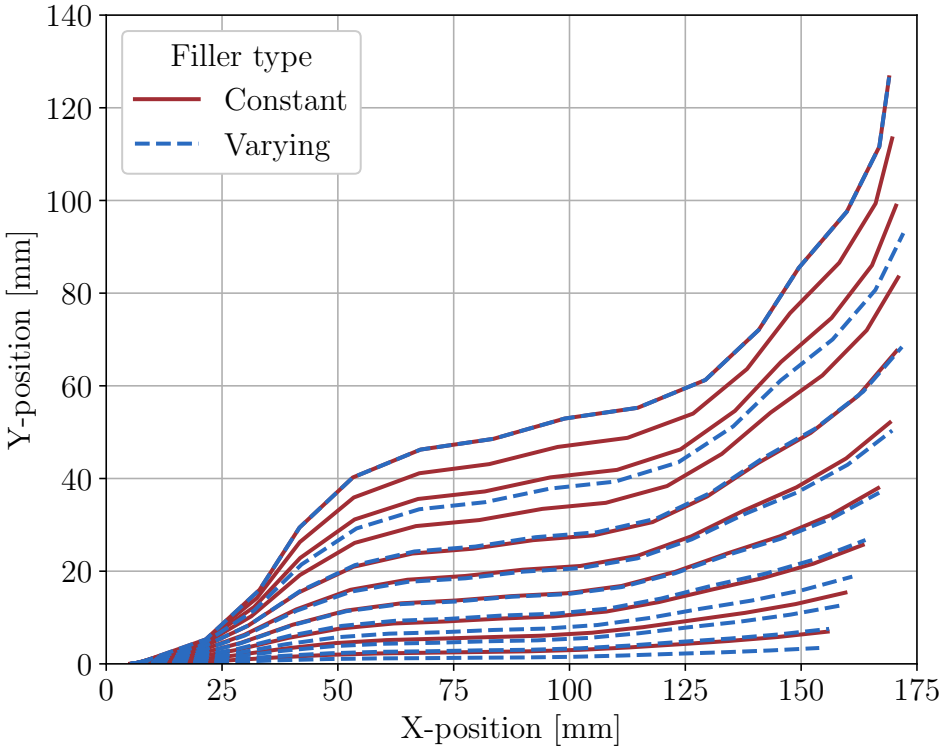

Figure 5.8: The difference between using a varying filler material stiffness versus using a constant modulus as shown when ramping the pressure from 0-45 kPa

Chapter 6

Design for Inflated Shape

The design procedure developed in this dissertation is tasked at solving different target shapes to demonstrate its application at solving such design problems. This chapter poses various design targets to the procedure and then investigates how well the numerical design matches that of the desired profile. These results are presented as an X-Y plot of the actuator's profile and an image of the inflated shape from the 3D FE model. For a selected number of actuators, the correlation to physical reproductions is also investigated.

6.1 Genetic Algorithm Hyper Parameters

Genetic algorithms require that a few user inputs be made prior to running the script. These parameters assist the GA with obtaining the best available solution. With poor user input, the optimiser can prematurely converge to a local minima, or can present final answers before an optimum has been reached due to slow convergence and a fixed number of iterations.

Guidelines and rules-of-thumb can be used to ball-park the values for these controlling parameters, but an application specific study needs to be performed to gain a better understanding of the system at hand. Population size plays a role at ensuring enough genetic diversity exists within the initial population. A study was performed where the actuator length was set at 15 units, a design target selected and the effect of varying the population size investigated. By submitting the same target with identical control parameters, but a different initial population five times, it is possible to de-

termine the extent to which local minima were converged to, and thereby whether sufficient genetic diversity exists in the population. No optimisation algorithm can guarantee convergence to a global optimum solution, but by carefully selecting the controlling parameters in the GA the likelihood of premature convergence to local minima can be reduced.

Once all the fitness values of an entire generation had been calculated a summary thereof was written to a file for post-processing. Within this information is the best performing individual of that generation. This information can be used to track at which generation the design algorithm typically cannot further improve the objective function value. The design process is programmed to complete a successful optimisation run once the number of generations has been met. As such, specifying more generations than what is typically required is computationally wasteful and comes at the cost of prolonged run times. The population size was varied from 20 to 80 in increments of 20 and used a number of generations fixed at 25. The number of total function evaluations therefore increase with population size.

It is important to reiterate that the same target was optimised throughout all of these simulation runs. The results in Figure 6.1 show that for a small population size, the final objective function value has a large spread, as indicated by the difference between the Lowest, Largest, and Mean values. This indicates that insufficient genetic diversity is available within the population. As the population size increases, the Largest value from each of the five runs decreases and approximates that of the Lowest value. The Average therefore also decreases. At a population size of 80, a converged answer is also found before the 13th generation. The remaining design problems all require that 15 units be used as the actuator length. To further improve the quality of the candidates provided, a population of 100 individuals evolved over 15 generations was used for further design work.

6.2 Single Specified Objective

The versatility of the design algorithm at presenting vastly different design configurations is demonstrated in this section. The design algorithm was tasked to solve problems where a single objective was applied to the tip position. To achieve the required outputs, only the position of the tip was

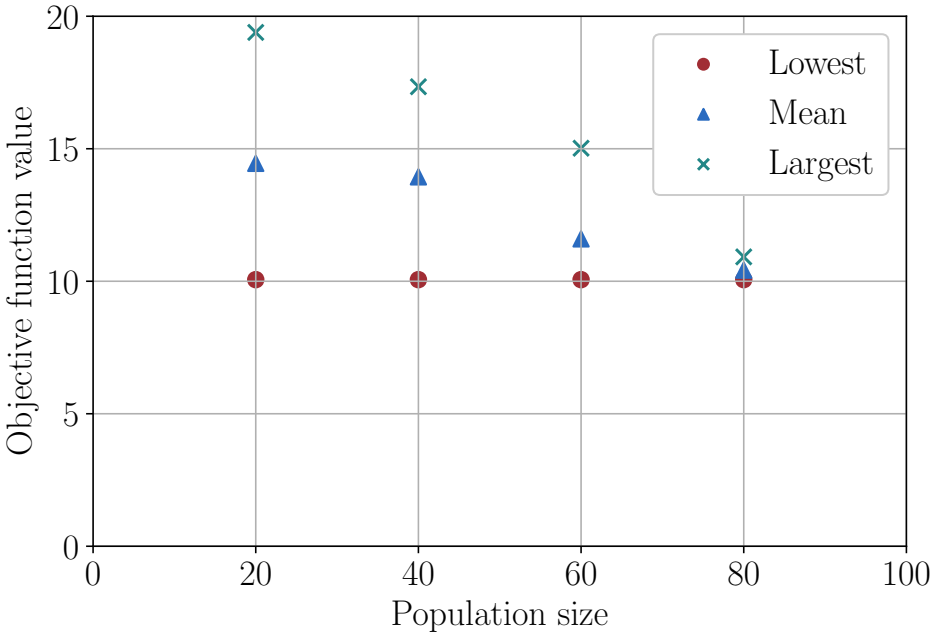

Figure 6.1: Effect of varying the population size on calculating the best estimated solution using a number of generations fixed at 25 (Lowest and Largest refer to the minimum objective function value found and Mean the average of that value for five different initial populations for a fixed population size)

considered. The hyper parameter in the GA, that determines whether the fitness function must be minimised or maximised, was altered as required. The exact objective functions solved are given in Table 6.1 along with a brief description of the desired outcome for the actuator tip.

Table 6.1: Objective functions solved for actuator tip position, where X_b, Y_b refer to the position of the base at the origin, and horizontal refers to the lengthwise direction of the actuator

Description	Objective function	Results
Maximum horizontal	max X	Figure 6.2
Minimum horizontal	min X	Figure 6.3
Maximum vertical	max Y	Figure 6.4
Minimum radius of curvature	min $\sqrt{(X_b - X)^2 + (Y_b - Y)^2}$	Figure 6.5

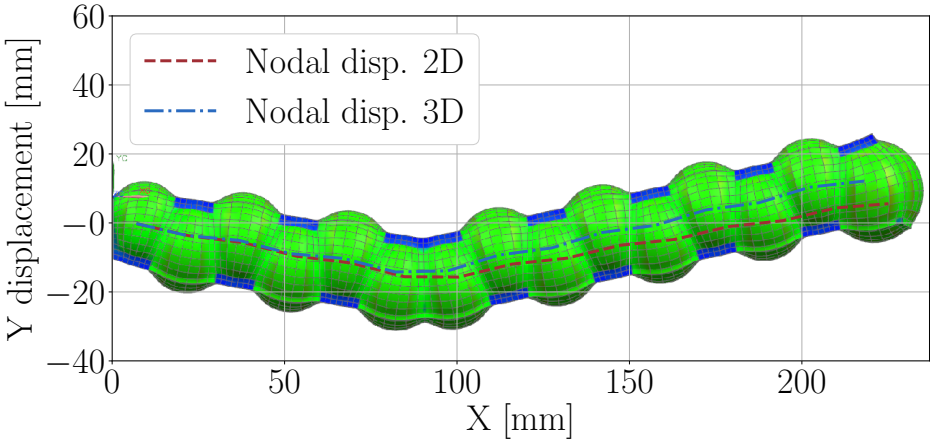

Figure 6.2: Maximum horizontal tip displacement [45 kPa]

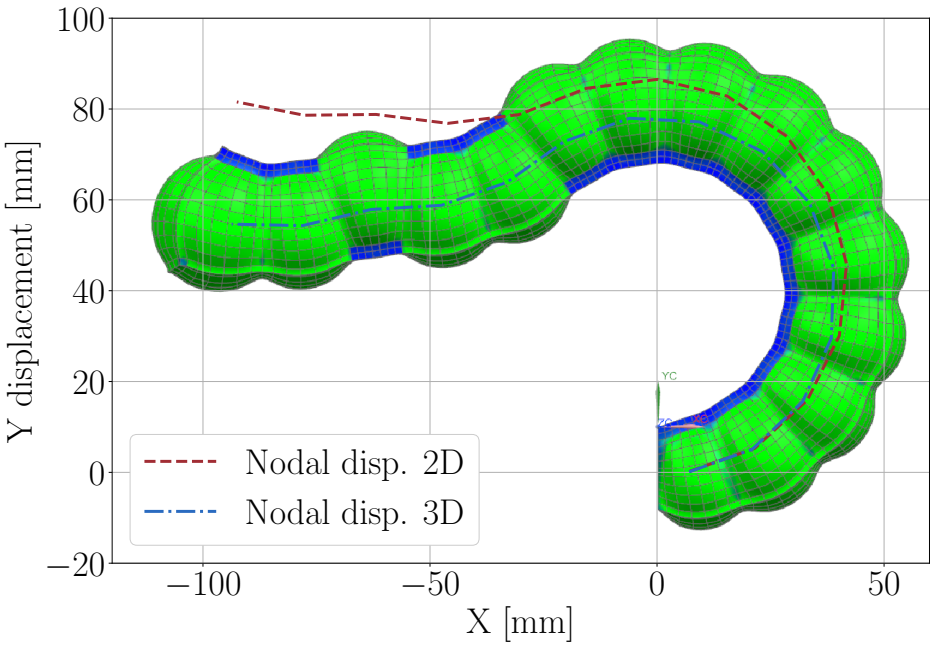

Figure 6.3: Minimum horizontal tip displacement [45 kPa]

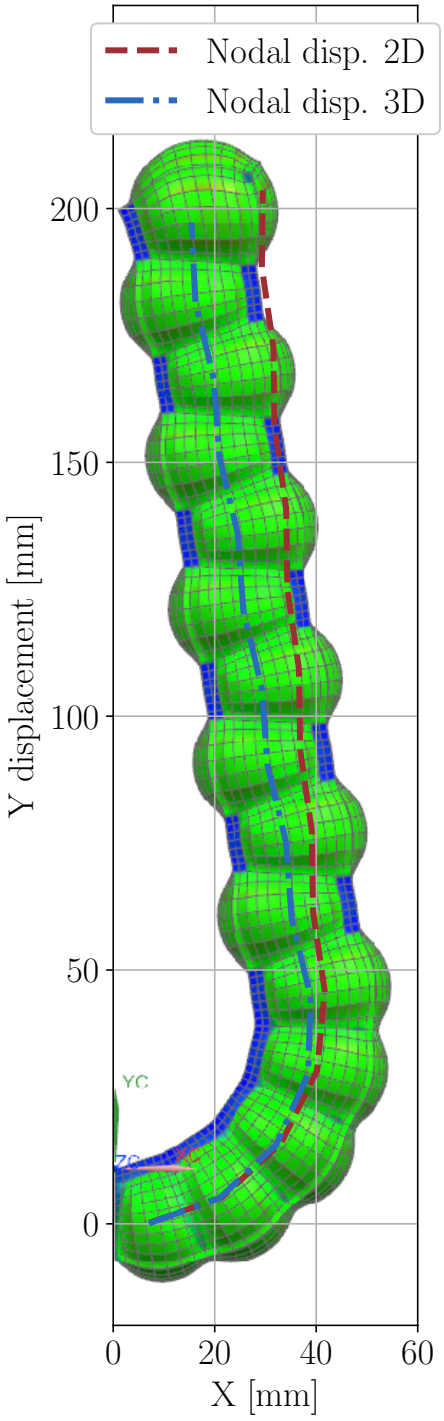

Figure 6.4: Maximum vertical tip displacement [45 kPa]

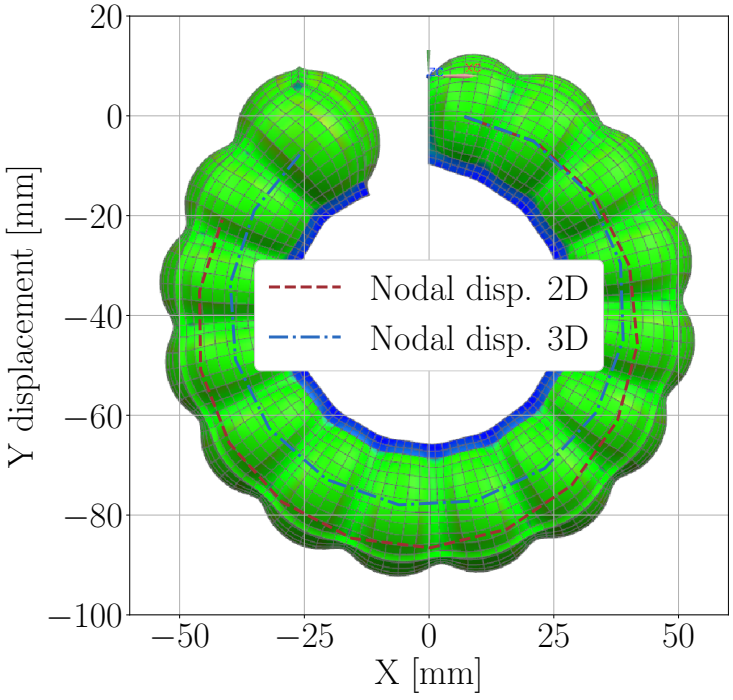

Figure 6.5: Minimum radius of curvature [45 kPa]

In each of the cases investigated there is deviation between the 2D and 3D models. The inflated shape of the 3D actuator however qualitatively resembles that of the 2D profile. The filler material was calibrated using actuators with random orientation vectors. In essence, the filler material is used to compensate for the stiffness provided by the sides of the 3D model. These sides inevitably provide a different stiffness depending not only on the internal pressure, but also the amount of deformation subjected to. The filler material therefore provides a smeared response for those actuators used in the calculation thereof. The design algorithm successfully managed to present candidates with different orientation vectors to best match the specified objective function.

6.3 Target Profile

This section tests the design algorithm for its ability to provide candidates for which the inflated shape best matches a desired continuous profile. Two trigonometric functions, evaluated at various amplitudes, were used for this purpose; sine and cosine. For both functions the design was restricted to investigate one full period and try to match the various amplitudes as best possible. No restriction was placed on the inflated length. Figures 6.6 – 6.11 show the results from these optimisations.

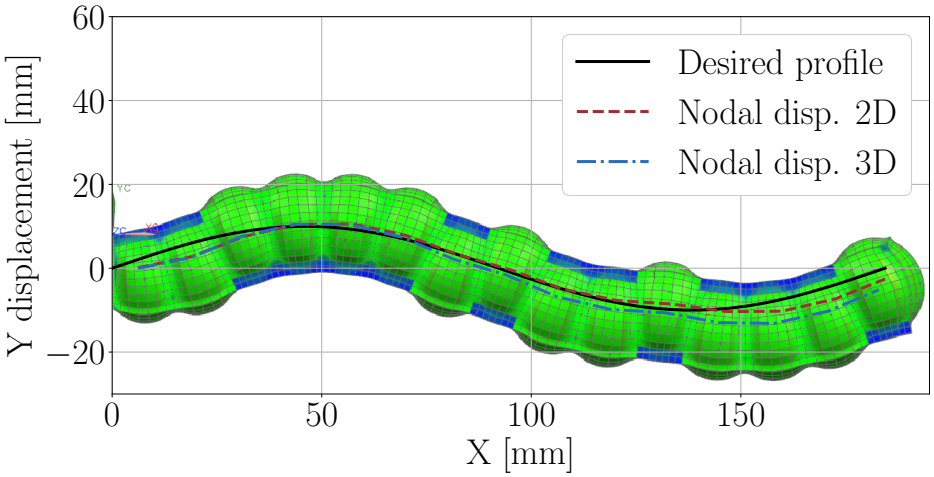

Figure 6.6: Candidate that best fits one period of a sine function with an amplitude of 10 mm [36 kPa]

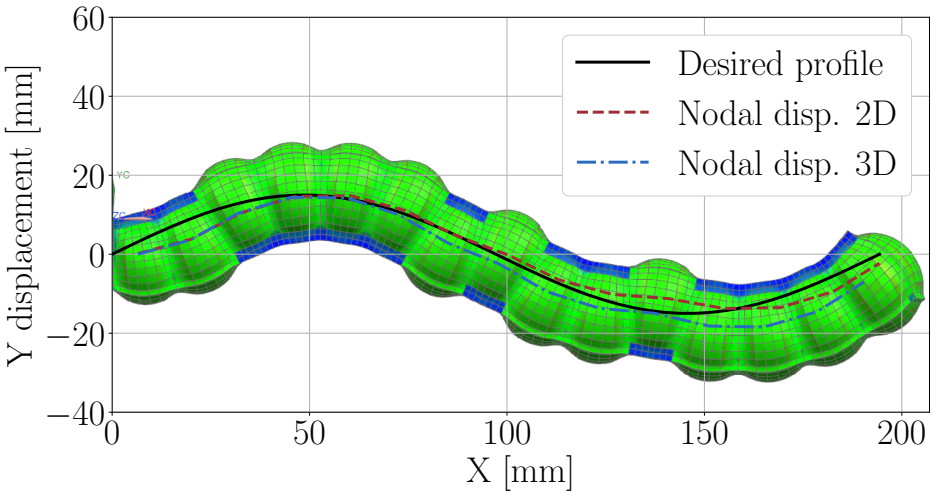

Figure 6.7: Candidate that best fits one period of a sine function with an amplitude of 15 mm [40.5 kPa]

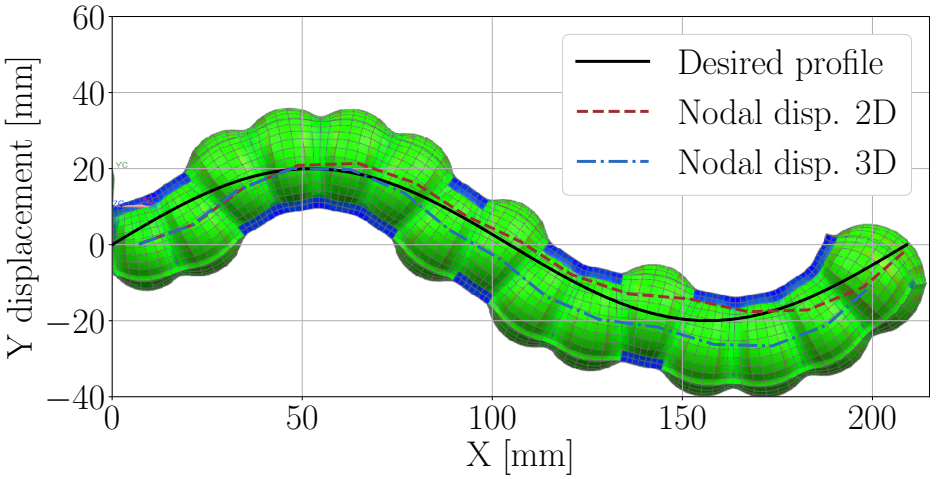

Figure 6.8: Candidate that best fits one period of a sine function with an amplitude of 20 mm [45 kPa]

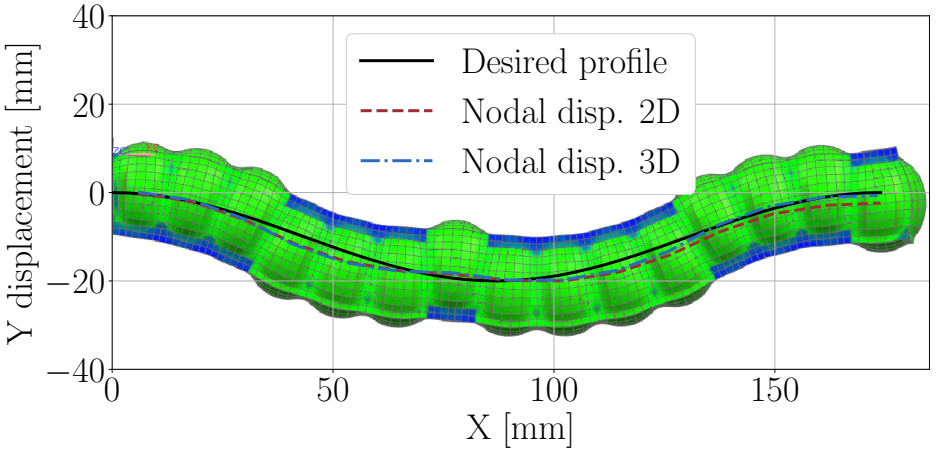

Figure 6.9: Candidate that best fits one period of a cosine function with an amplitude of 20 mm [31.5 kPa]

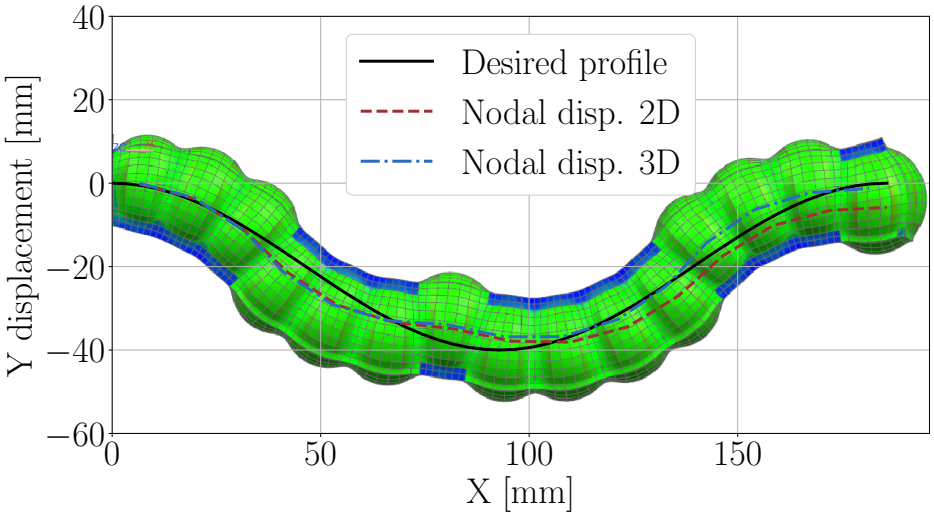

Figure 6.10: Candidate that best fits one period of a cosine function with an amplitude of 40 mm [40.5 kPa]

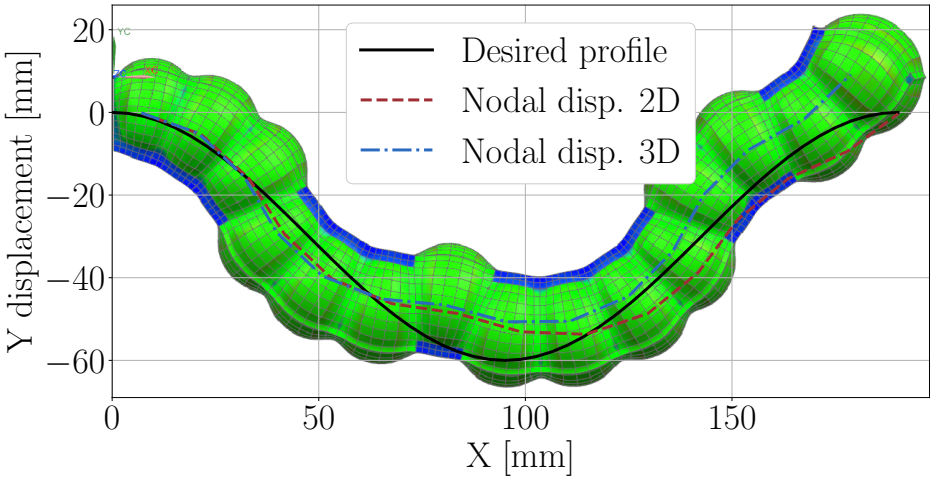

Figure 6.11: Candidate that best fits one period of a cosine function with an amplitude of 60 mm [45 kPa]

For both the sine and cosine functions, candidates are provided that closely match the desired profiles at lower amplitudes. With increasing amplitudes comes larger disparity between the desired profile and what the numerical actuator could achieve. This does not necessarily indicate a weakness in the design algorithm, but points to a physical restriction of the articulating unit at larger deformations. The nature of the two different profiles allows the cosine function to fit to larger amplitudes than the sine function can.

6.4 Physical Actuators

6.4.1 Manufacturing

A sensitivity study relating the effect of manufacturing tolerances of 3D printed moulds to the inflated shape of an actuator was performed in Appendix E. The results showed that a ± 0.1 mm tolerance on the parameters can significantly change the shape of the actuator. To reduce this effect, a set of modular moulds were designed to be manufactured from machined aluminium parts and steel dowel pins. Benefits of this approach include tighter tolerances at ± 0.02 mm and a stronger mould that is less susceptible to degradation due to use. Figure 6.12 shows the different components of the mould and Figure 6.13 shows the mould assembled, ready for casting.

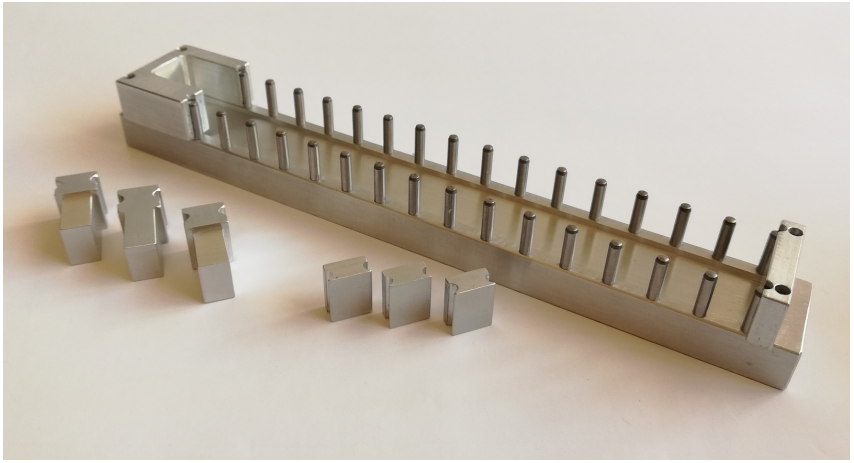

Figure 6.12: Parts of aluminium mould used to manufacture the modular actuator

Figure 6.13: Assembled aluminium mould used to manufacture the modular actuator

The Mold Star 15 prepolymer was poured into the mould and placed in a vacuum chamber for 15 min to enable trapped air bubbles to escape. Once removed from the chamber, additional prepolymer was poured onto the mould to overfill it. A thick, smooth steel plate was slowly placed over the open end of the mould, forcing the excess silicone out of the mould. This method delivered the most consistent finish to the actuator exposed to the open-end of the mould. After complete curing, the actuator was removed from the mould and flashing removed. Circular holes 1.5 mm in diameter were punched between adjacent units to ensure connectivity.

The Smooth-Sil section was cast as one large slab between two glass panes separated with aluminium spacers machined to a width of 3 mm. The cured slab was cut into 15 mm wide strips using a sharp blade and a steel ruler. These strips were further cut down to the required individual lengths specific to each actuator. Sil-Poxy was used to glue the different sections together. Figure 6.14 shows a collection of manufactured actuators.

6.4.2 Testing

The low pressures and soft materials make these actuators susceptible to measurement inaccuracies due to friction if placed on a flat surface while evaluating their shape if no precautions are taken. To minimize these errors, a glass pane was used and silicone oil used to lubricate the glass and the

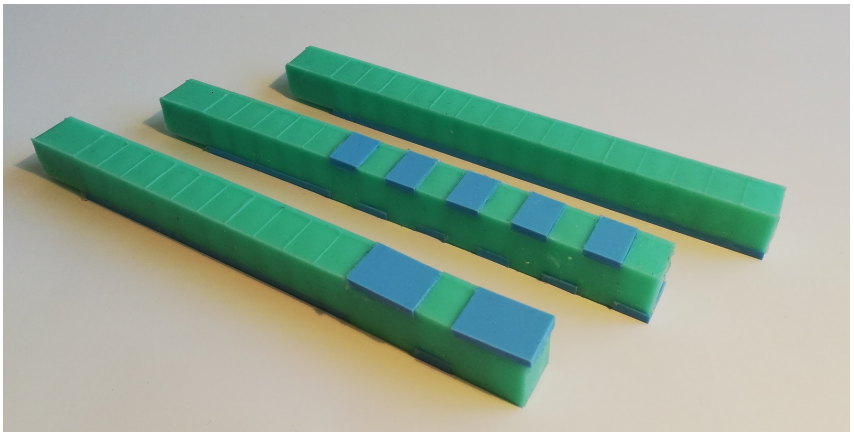

Figure 6.14: Manufactured actuators

actuators. This combination resulted in a slippery surface with minimal friction.

The actuator was inflated by inserting an 18 gauge surgical syringe through the base into the void of the first articulating unit. A second 18 gauge syringe was inserted for pressure measurements using a 25-500 mbar Endress+Hauser pressure transducer. The thicker slab of silicone at the base prevents air from escaping through the insertion. The pressure was regulated using a manual pneumatic pressure regulator.

Once inflated to the required pressure, a two camera HP 3D Structured Light Scanner was used to scan the deformed actuator. The model was cleaned up using the HP 3D Scan 5 software and a `.png` picture of the side view exported.

6.5 Results and Discussion

It is required to demonstrate how the actuators generated by the design algorithm translate to the real world. A number of selected actuators were therefore manufactured and physically tested in order to find the correlation between them and the corresponding numerical models. Figures 6.15 to 6.19 show these actuators as the physical models overlaid with the perimeter of the numerical models for each actuator. These results were processed in Python where the `.png` picture of the scanned actuator was used as a background for the numerical data. The `.png` picture was scaled using the scanned `.stl` model imported into NX 12.

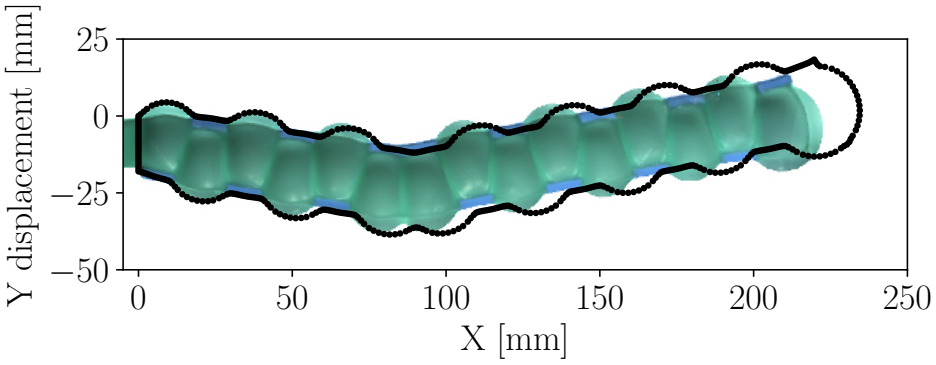

Figure 6.15: Comparison between numerical (dotted black line) and physical (solid green and black background) models of the maximum horizontal tip displacement actuator

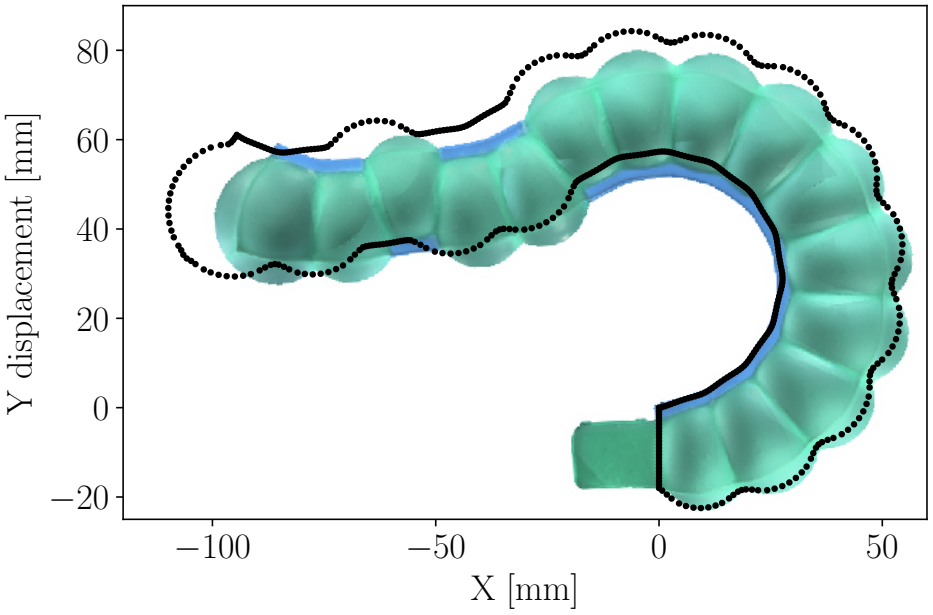

Figure 6.16: Comparison between numerical (dotted black line) and physical (solid green and black background) models of the minimum horizontal tip displacement actuator

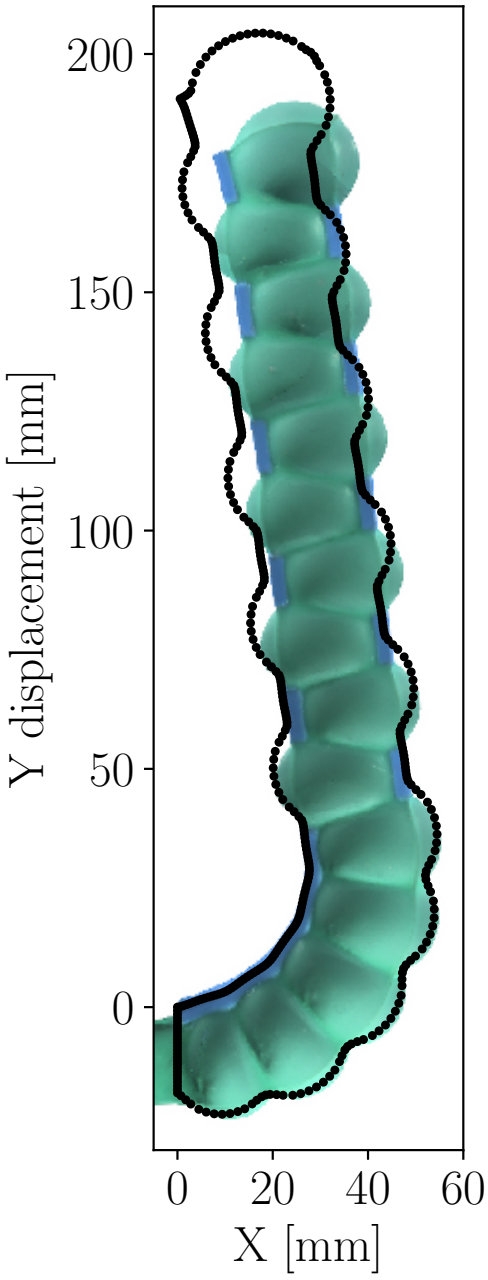

Figure 6.17: Comparison between numerical (dotted black line) and physical (solid green and black background) models of the maximum vertical tip displacement actuator

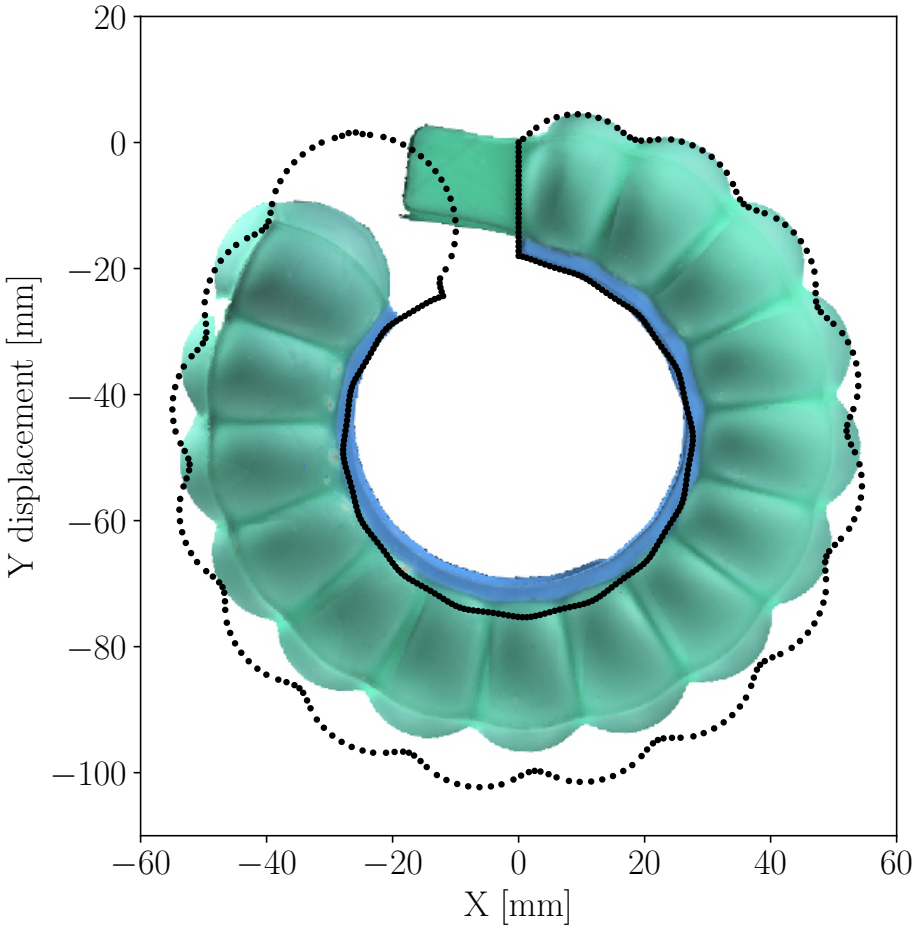

Figure 6.18: Comparison between numerical (dotted black line) and physical (solid green and black background) models of the maximum curl actuator

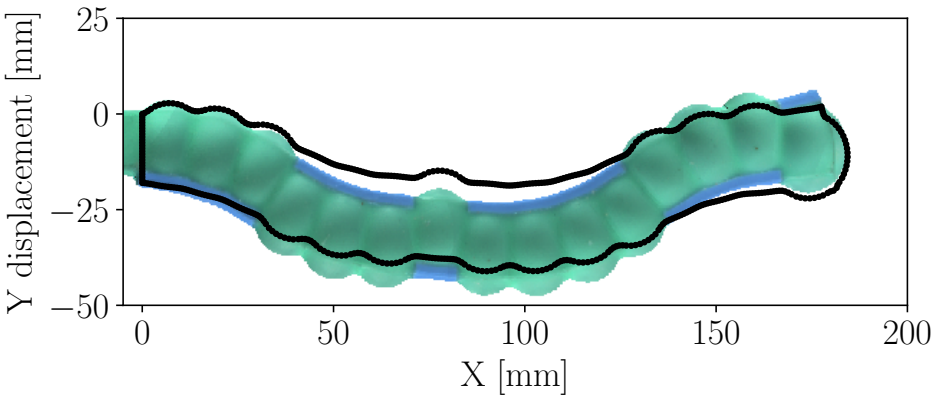

Figure 6.19: Comparison between numerical (dotted black line) and physical (solid green and black background) models of the actuator designed for a cos function with an amplitude of 20 mm

A qualitative comparison between the performance of the physical models and the numerical models is provided. For all designs presented, the physical models correlate well with the numerical designs for overall deformed shape. In general the physical models appear overly stiff when comparing the final tip position. The desired design targets can be identified in the inflated physical actuators. Possible causes for this deviation is most likely a combination of minor inaccuracies in the material model of the silicones (Appendix A), the numerical simplifications made (Appendix D), and the sensitivity of the physical model to manufacturing tolerances (Appendix E).

Chapter 7

Discussion and conclusion

The overarching research question in this project set out to investigate the extent that different behaviour can be incorporated and pre-programmed into soft pneumatic actuators. The research conducted was restricted to soft pneumatic actuators and materials that can contribute to them. The main areas that were touched on are concluded individually along with the novel contribution.

7.1 Bimodal Behaviour in a SPA

A means to exploit the trait of soft robots that allow designers to embed deformation characteristics directly into their architecture was sought in this chapter. One such method was devised by creating a material with a bilinear response that activates at an adjustable and predictable strain threshold. Results show that the threshold at which strain stiffening occurs can be controlled in the composite and can be predicted using both an analytical or numerical model. By increasing the crimp ratio (decreasing the wavelength of the triangular flutes) it is possible to further delay the strain at which the crimped paper layer is activated.

Three different crimp ratios of this bilinear composite material were incorporated into a SPA. Physical and numerical models were created to investigate the response of the SPA to an increasing internal pressure. Both these models showed the desired behaviour where a preferential bending direction exists at lower pressures. As soon as the SPA has been inflated to a large enough pressure, such that the deformation is sufficient to strain the

bilinear material beyond its strain transition point, a new preferential bending direction is created in the opposite direction. A disparity between the required pressures and displacements magnitudes was found between the physical and numerical models, but both approaches yielded similar trends.

The significant contributions can be summarised as:

1. Development of a bilinear composite material with a tunable transition point using paper and silicone. This includes an analytical and numerical model that correlates well with experimental values.

2. Manufacturing of a bimodal actuator where a single pressure source can be used to generate different bending directions by merely altering the internal inflation pressure.

7.2 Automated Evolutionary-Based Design Algorithm

This research set out to develop a computational tool that can assist with designing modular soft robotic actuators where the final inflated shape is of importance. It was shown that it is possible to utilize numerical design and optimisation tools for this process. By using a modular approach, and a simple deforming unit, it was possible to allow the design algorithm to predict the orientations for each of the fifteen units in order to best match the desired profile. The employed genetic algorithm drastically reduced the number of function evaluations required to reach this optimum design from a possible 32 768 available combinations to $< 1\ 000$ function evaluations. The 32 768 available combinations is from each of the fifteen units having two different orientations, 2^{15}.

The computationally intensive task of solving hundreds of 3D FE analyses as part of an iterative optimisation scheme was investigated to find a solution for improved run times. It was possible to create a reduced order model of the system, where the 3D model that uses quadratic hexahedral elements was simplified to a 2D plane strain case using quadratic quad elements. This model decreased the solution time for each fitness evaluation from 590 s to 45 s, on average, for the actuators investigated. Quantifying the error between the 3D model and the reduced-order 2D model using a

random orientation vector showed an average node-to-node error along the center line of 4.32 mm. The results, where the reduced-order model was used as part of the optimisation, however showed larger deviations. The overall deformation shape however remained qualitatively similar, and given the much decreased run times, proved a valuable addition to the design algorithm.

Five different physical actuators were manufactured, each of which was designed for a unique desired shape. The testing procedure followed made an attempt to measure the most accurate shape of the inflated actuator by using a 3D scanner and methods that reduced measurement inaccuracies. A qualitative comparison was performed between the numerical and physical models. Overall close correlation was found between the deformed shapes. The extensive numerical design work performed throughout this work therefore correlates well with physical actuators.

The final design algorithm is capable of suggesting candidate solutions that closely match a request from a user for a desired profile. The suggested candidate is numerically determined, but also qualitatively resembles that of a physical model.

The significant contributions can be summarised as:

1. The ability to specify a desired profile, or design target, and allow an evolutionary-based design algorithm to suggest candidates that best match the profile.

2. A numerical method to simplify a 3D model of a SPA to a 2D model that decreases solution time by ≈ 92 %.

Chapter 8

Future Research

8.1 Further Mechanical Characterisation of Silicone

Due to the sensitivity of the actuators to numerical input data, a further detailed study needs to be performed on the three different silicones used. The models were shown to be sensitive to bulk modulus, which will warrant the time to develop a test device that can measure this parameter more accurately.

All material tests performed in this research were limited to uniaxial tests. The inflated actuator inevitably experiences a biaxial load case, which would require that the material be characterised for a similar response.

DIC was used to capture material strain due to loading. This method limits the range that can be captured accurately due to the area-of-interest moving out of the field-of-view of both cameras and the random paint speckle peeling off. A long travel extensometer will need to be performance tested against the DIC values for low strain, where after a decision can be made whether to proceed with it. A long travel extensometer should yield a faster test procedure which will facilitate a larger testing strain range.

8.2 Improved 3D Model of Bimodal Actuator

In Chapter 3 the numerical and physical models both showed the desired bimodal behaviour, but at different pressures. This disparity was most

likely caused by the method with which the response of the bilinear material was modelled leading to an inaccurate strain transition point and an overly stiff response. While developing the bilinear material, rebar elements in MSC.Marc were used in a planar numerical study. This 2D study yielded close correlation with the analytical and physical models. The 3D work performed in this research should be repeated using 3D rebar elements in Marc. This will allow the material properties of the paper and Ecoflex 0030 to be included individually in a manner which better resembles the actual bilinear material.

8.3 Geometry of Articulating Units

Better adaptability and functionality can be achieved from the modular actuator by improving certain aspects thereof. Two of these approaches include improving the unit used throughout this research in the following ways:.

1. By reducing the lengthwise size of each articulating unit (and therefore the size of the void), it will be possible to use more units without increasing the overall length of the actuator. By using more units, it is envisioned that more design possibilities can be achieved.

2. By optimising the articulating unit for some performance metric; maximize the angle (Ω) between the two sides while minimising the ballooning height, h_b, subject to some failure strain threshold, Figure 8.1. With this approach, more degrees of articulation will be possible for each unit, whilst resulting in a smoother actuator due to a lower ballooning height.

8.4 Create a Library of Articulating Units

The proposed evolutionary design algorithm can facilitate additional types of articulating units. A library of these units can be created where different deformation modes can be incorporated, such as:

1. A low degree of preferential bending at high pressures

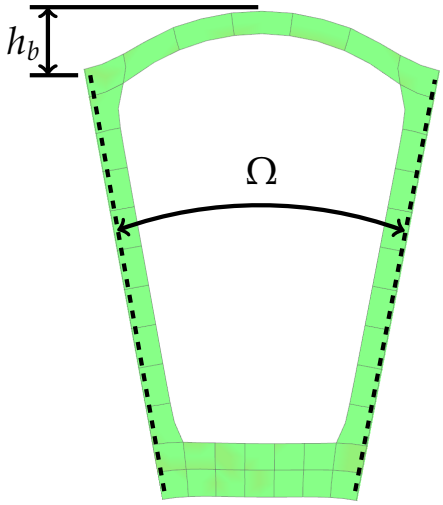

Figure 8.1: Metrics to incorporate in an optimisation for improved unit performance

2. A high degree of preferential bending at high pressures
3. Linear extension with increasing pressure
4. Near rigid response to increasing pressure
5. Bimodal response with two opposite bending directions controlled only by a linear positive pressure ramp

8.5 Improved Correlation Tool

A tool can be created to better align the 3D scanned physical actuator to the numerical model by translating and rotating the models relative to each other. This can be achieved using a least squares fit between corresponding points on the two models. A more accurate comparison can be drawn between the different models which will lead to better insight to areas that require further work.

Appendices

Appendix A

Silicone Characterisation and Modelling

This research uses three readily available silicones that cover a range of different stiffness values: the Smooth-On (2019) products Ecoflex 0030, Mold Star 15, and Smooth-Sil 950. This section introduces the material and covers the testing and characterisation processes followed. Reliable material response data was not available for these materials and required that experimental characterisation be done.

A.1 Digital Image Correlation

Soft silicones are not conducive to conventional strain measurement techniques; the attaching of clip gauges and strain gauges alter the local material properties and lead to inaccurate measurements. As such Digital Image Correlation (DIC) (LaVision GmbH, 2015) was used to measure the surface strains throughout testing. DIC is a non-contact strain measurement technique which requires a random contrasting pattern, known as a speckle pattern, to measure surface strain on the material. This comparison is achieved by correlating grey-scale intensities of a set of interrogation windows, or subsets, throughout reference and deformed images. This speckle pattern has an effect on the accuracy of the method (Lecompte *et al.*, 2006) and as such, deciding on the ideal speckle for optimum accuracy is currently an area of active research. In a previous study Ellis (2017) benchmarked the accuracy of the system and performed a speckle pattern quality assessment

for woven polypropylene. That information was brought forward to the current project. A representative picture of the speckle used throughout this research is shown in Figure A.1.

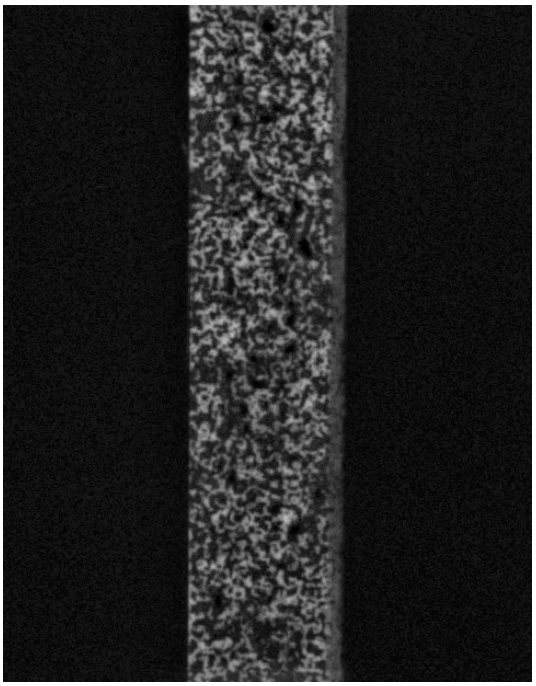

Figure A.1: Contrasting speckle pattern as applied to a silicone dumbbell sample

A.2 Testing and Characterising the Base Materials

Material mechanics problems can typically be divided into two main categories: predictions of deformation behaviour and predictions of failure events (Bergstrom, 2015). The nature of this project is not concerned with material failure, but requires that material deformation accurately be predicted. As such, the testing procedure has been designed to extract displacement data to a load response.

A.2.1 Sample Preparation

Standardised test procedures developed for testing rubber-like materials from the International Organisation for Standardisation (ISO) were used for characterising the three silicones in tension, ISO 37 (ISO, 2011), and compression ISO 7743 (ISO, 2017). All samples were allowed to cure at room temperature.

For tension, a dumbbell shaped geometry is required and dimensions of the Type 1A sample using a thickness of 2 mm were chosen from the standard. A negative of this geometry was CNC machined into a block of aluminium and four replicates of each material were cast, degassed and allowed to cure at room temperature. Two degassing steps are required to ensure no bubbles are trapped in the material; the first step is in the mixing cup once the two parts have been mixed; the second step is after the pre-polymer has been poured into the aluminium mould. After the final degassing step, a steel blade was slowly scraped along the top surface of the mould to remove excess pre-polymer. This led to the formation of a meniscus on the top surface of the sample. An alternative manufacturing method would be to cast a large flat piece of the material between two separated glass-panes. This alternative method would ensure better thickness distribution over the sample, but would require that each dumbbell-shaped sample be punched from the larger sheet, which in itself introduces additional problems and costs.

Once cured, the samples were removed from the casting moulds and their cross-sectional thickness evaluated under a microscope. This was a destructive test, so one of the four samples was cut with a sharp blade and mounted such that it could be viewed under a microscope. Measuring tools available with the microscope software were used to determine the area of each sample. These areas are given in Table A.1 and the microscope images in Figure A.2.

Table A.1: Cross-sectional area of each silicone dumbbell as measured under a microscope [mm^2]

Ecoflex 0030	Mold Star 15	Smooth-Sil 950
9.69	9.38	8.50

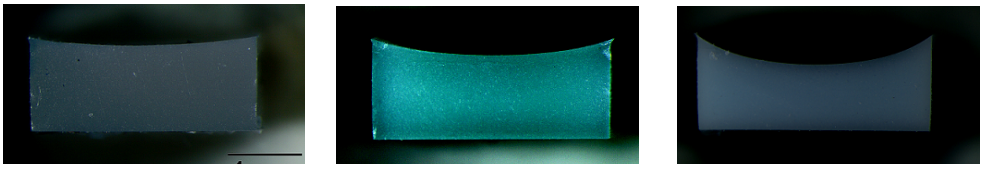

(a) Ecoflex 0030 (b) Mold Star 15 (c) Smooth-Sil 950

Figure A.2: Cross-sectional view of the meniscus that forms when casting the various silicone dumbbell samples for tensile testing.

Solid round pucks were required for compression testing of the silicones. The dimensions for Standard Test Piece A were used and an aluminium mould manufactured to cast three samples of each silicone, Figure A.3.

Figure A.3: Samples used for determining the stress-strain behaviour of the three different silicones (Ecoflex 0030 [Left], Mold Star 15 [Center], and Smooth-Sil 950 [Right])

A.2.2 Density

When testing the physical actuators, much of the experimental measurement uncertainty can be mitigated by clamping it at its base and letting the rest of the actuator hang down freely. To simulate this in the numerical

models, an acceleration equal to gravity can be applied to the entire model. Accurate material density is therefore required to calculate the load magnitude.

The pucks manufactured for the compression testing were weighed using a digital scale and their dimensions taken using a digital vernier calliper. The densities were calculated using the measured weight and the calculated sample volume. The results for the three silicones are presented in Table A.2.

Table A.2: Material densities of the three different silicones [kg/m^3]

Ecoflex 0030	Mold Star 15	Smooth-Sil 950
1031	1139	1211

A.2.3 Uniaxial (Tension and Compression) Properties

A universal mechanical tensile test frame (MTS Criterion Model 44), a 1 kN load cell, and a LaVision DIC system were used during mechanical testing. Ambient lighting conditions were kept constant throughout testing by only testing at night. For compression testing, smooth aluminium parallel plates were used to compress the sample. The narrow area between these two plates required that additional lighting be used for the DIC system to function properly. The LED lights in the LaVision package were too intense when aimed directly at the sample. The shiny, curved surface of the silicone pucks caused reflections that rendered that area on the captured image useless. To circumvent this, white printer paper was placed around the sample and the lights rather directed at the paper. This caused a softer light to be reflected onto the sample over a larger area, Figure A.4. Samples were tested at a crosshead speed of 10 mm/s to a compressive strain of 30–40%. A thin film of lubricant was applied to both the flat plates and the sample to ensure a near frictionless surface.

The test set up for the tensile properties is presented in Figure A.5 where the DIC system can be seen relative to the load frame. A set of self-tightening roller grips (Instron) were used and samples tested at the required speed of 50 mm/s with images being taken at 1 Hz. These samples were not as prone

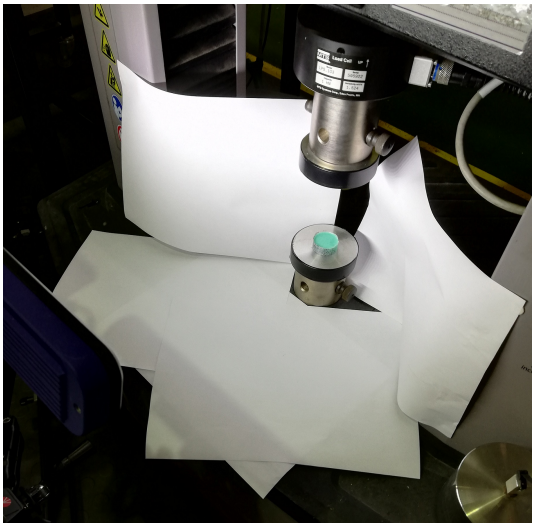

Figure A.4: Experimental lighting setup used for testing the compression properties of the silicone pucks

to the reflection issues and it could be resolved by placing sheets of white printer paper directly over the additional LED lights.

All the tensile samples were preconditioned by stretching them to 200 % strain before applying the contrasting speckle using satin black rattle-can paint. This pre-stretching is to overcome the Mullins effect (Mullins, 1969) where a rubber material softens when subjected to cyclic loading. This softening dissipates after a few cycles where after material response stabilises. Meunier *et al.* (2008) did however find the Mullins effect to be negligible for unfilled silicones rubbers. The speckle pattern was applied using satin black paint on an individual basis per sample, immediately followed by the tensile testing. This ensured that the test proceeded while the paint was still damp and lowered the risk of the speckles peeling off due to the large strains being encountered.

When inserting the sample into the roller grips, it tends to buckle in the longitudinal direction. To ensure that the sample was initially flat before applying the load, a marker was used to place ink lines spaced at 25 mm on the sample while still in the aluminium casting mould. This made it possible to load the sample into the grips and measure the distance between the two marks. The crosshead could be moved until the correct distance was achieved. Provision for a pretension is made by ISO 37, but the prescribed 0.1 MPa magnitude is not always feasible, especially on low Shore-hardness

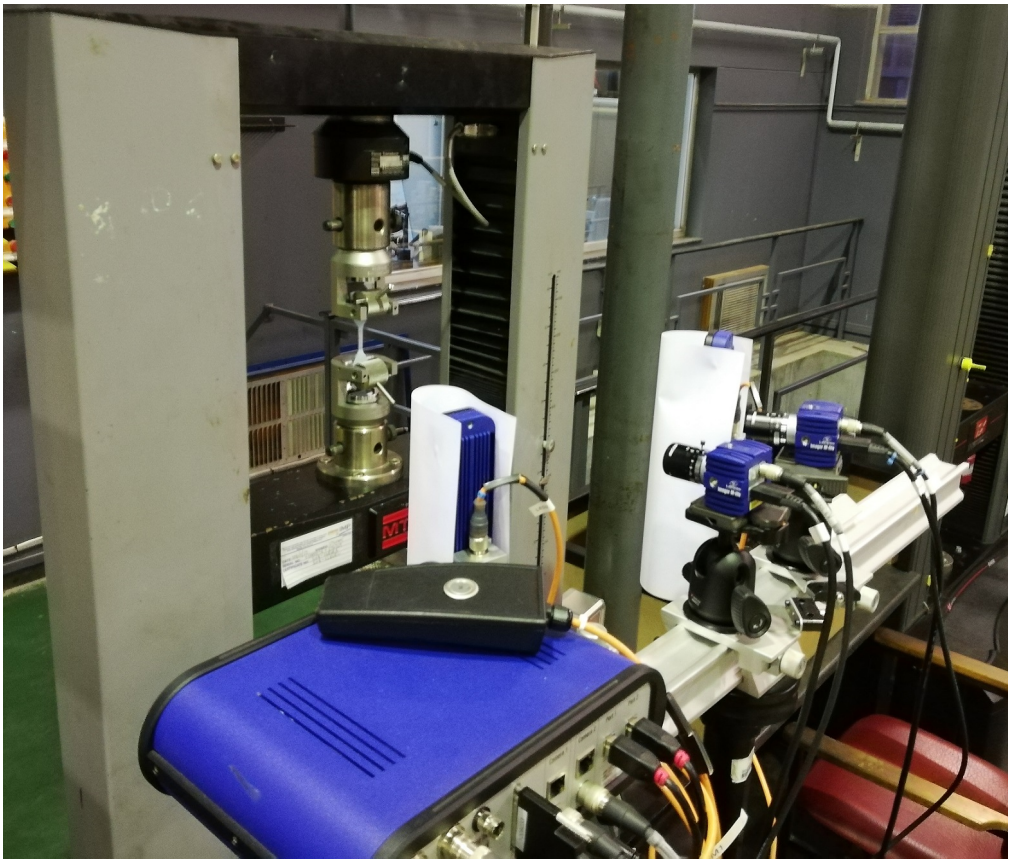

Figure A.5: Experimental setup used for testing the tensile properties of the silicone dumbbells

materials. The LaVision GmbH (2015) software was used to process the captured images and output engineering strain in the longitudinal and transverse testing directions. The DIC system is stand-alone from the test frame and requires that the load measurements be ported to it as an analogue signal. The scale factor for this signal was adjusted at the no-load condition and by hanging a 40 N load to it.

Figures A.6-A.8 show the mechanical response to tensile and compression loading on engineering stress-strain graphs for the Ecoflex 0030, Mold Star 15, and Smooth-Sil 950 respectively. The visibly rough line on Figure A.6 is due to using the 1 kN load cell at the lowest end of its usable range - noise in the signal is therefore measured as well.

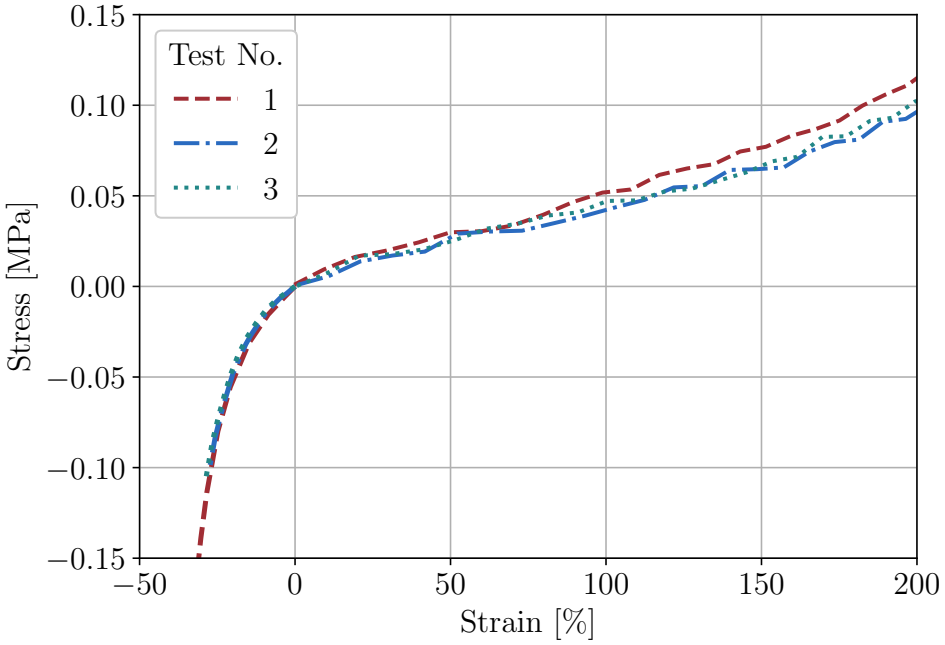

Figure A.6: Tensile test results for Ecoflex 0030

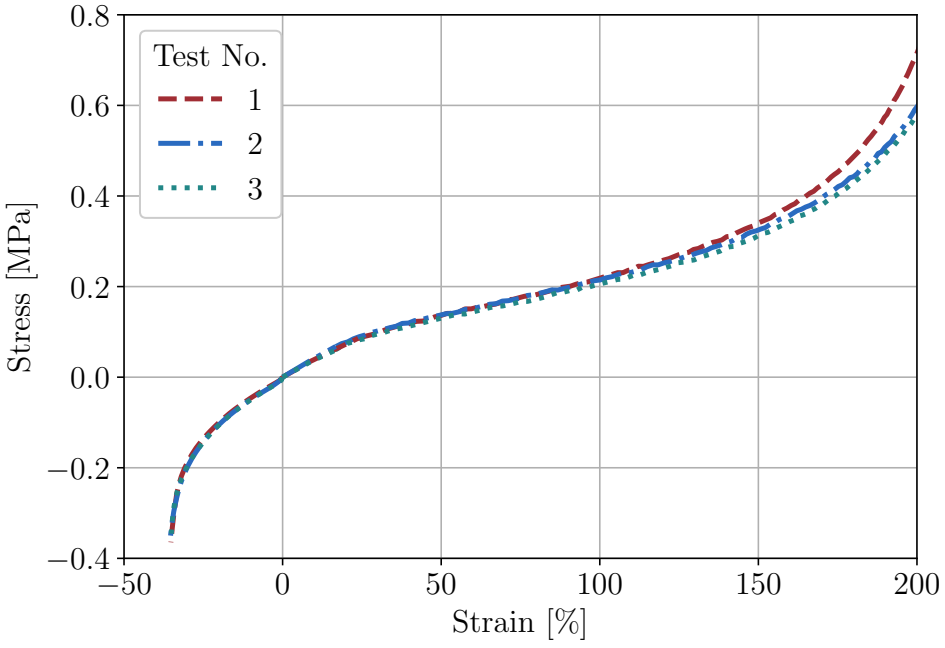

Figure A.7: Tensile test results for Mold Star 15

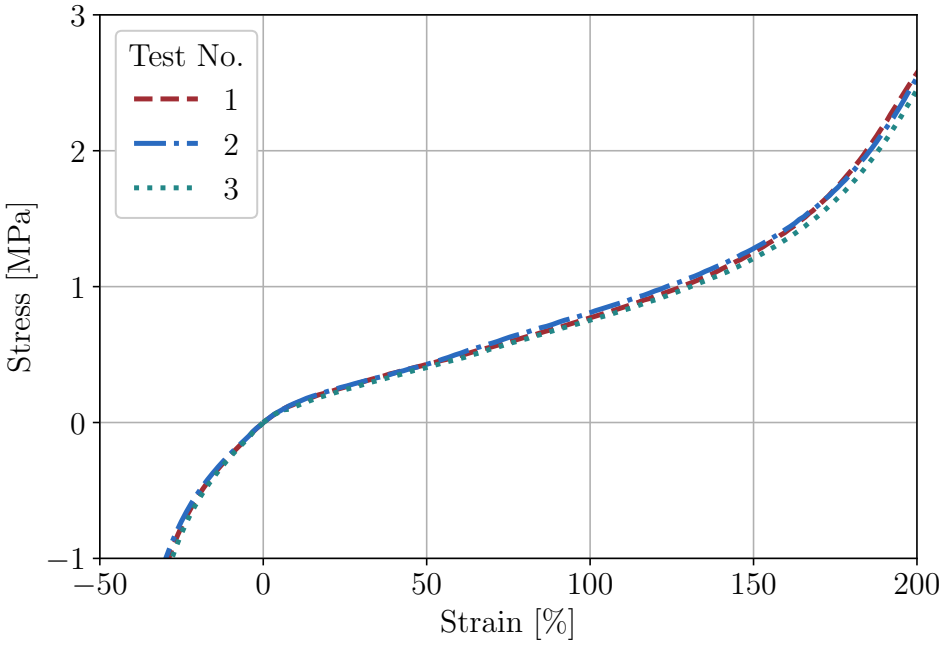

Figure A.8: Tensile test results for Smooth-Sil 950

Performance of Material Models

The chosen software package in this project, Siemens NX12 (2017), requires that the appropriate constitutive model be selected and the calibrated parameters then input. MSC.Marc (2018*c*) however allows that raw experimental data be loaded and the curve fitting done in-house. The experimental data was prepared and material models therefore processed using Marc.

The accuracy of the discussed models to representing the required silicones is presented in this section. The conclusion as to which model will ultimately be used is dependent on the R-squared value as well as its ease of use in the chosen software package. The R-squared value, or coefficient of determination, is a fraction that represents the proportion of the variance for a dependent variable that is explained by an independent variable in a model. The R-squared value is given by

$$R^2 = 1 - \frac{SSE}{SSTO} \tag{A.1}$$

where

$$SSE = \sum_{i=1}^{n} (Y_i - \hat{Y}_i)^2 \tag{A.2}$$

and

$$SSTO = \sum_{i=1}^{n} (Y_i - \overline{Y}_i)^2 \tag{A.3}$$

with Y the experimental data, $\hat{Y}$ the value from the material model, and $\overline{Y}$ the mean of the experimental data. SSE therefore represents the variation explained in the model and $SSTO$ the total variance in the data. The R-squared values for all four material models for each of the three different silicones are given in Table A.3. Figures A.9–A.11 show the fit of each model over the strain range used for calibration. It is clear that the two-term Mooney-Rivlin model is incapable of capturing the strain-hardening of the materials, and in general, is a poor fit to the data. The three-term Mooney-Rivlin, Yeoh and Ogden models are all reasonable fits, but the Ogden model is superior based on the R-squared value. The Ogden constitutive equations are available in NX12 and is therefore the chosen model for this project.

Table A.3: R-squared values for the various hyperelastic material models

Material	Ogden	MR2	MR3	Yeoh
Ecoflex 0030	0.9946	0.7991	0.9130	0.7963
Mold Star 15	0.9926	0.9256	0.9395	0.9626
Smooth-Sil 950	0.9980	0.8594	0.9732	0.9766

At this stage, only the μ and α parameters of the Ogden models are known and are given in Table A.4, with all μ terms in N/mm^2 and all α terms dimensionless.

Table A.4: Ogden parameters for the three different silicone materials

Material	μ_1	α_1	μ_2	α_2	μ_3	α_3
Ecoflex 0030	-0.0143	-5.224	-3.646e-10	-0.1628	9.594e-8	11.38
Mold Star 15	-6.503e-6	-21.32	0.2169	1.180	1.372e-3	4.884
Smooth-Sil 950	-0.3062	-3.059	0.0283	4.597	6.596e-9	17.69

The bulk modulus parameter, D, requires a further review and study.

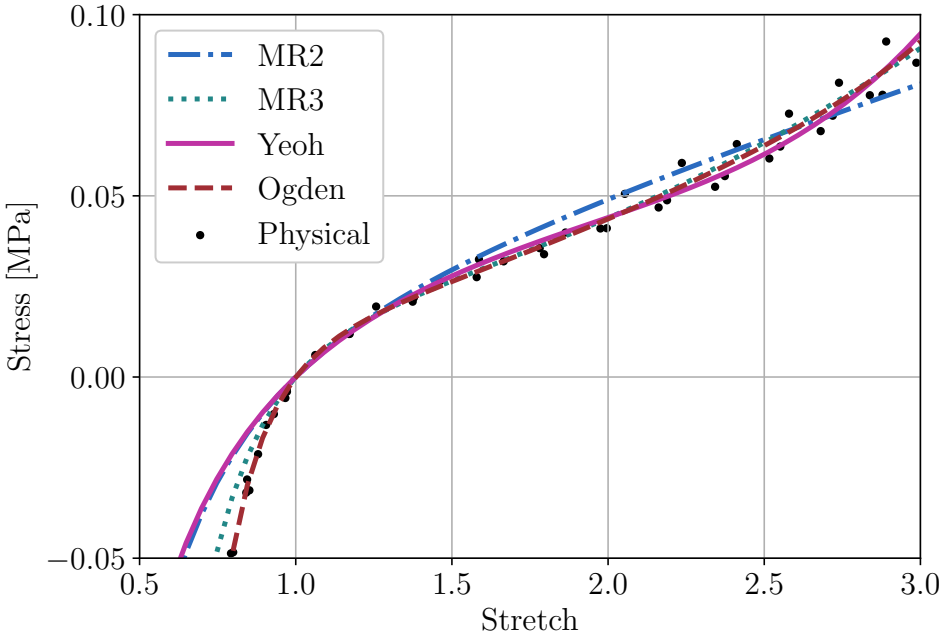

Figure A.9: Material models as fit to experimental data of Ecoflex 0030

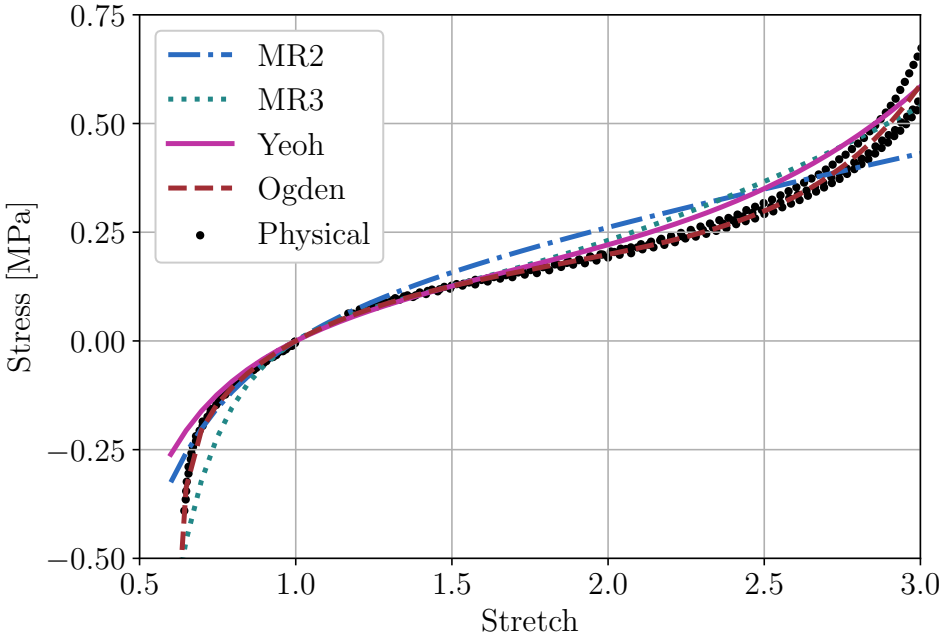

Figure A.10: Material models as fit to experimental data of Mold Star 15

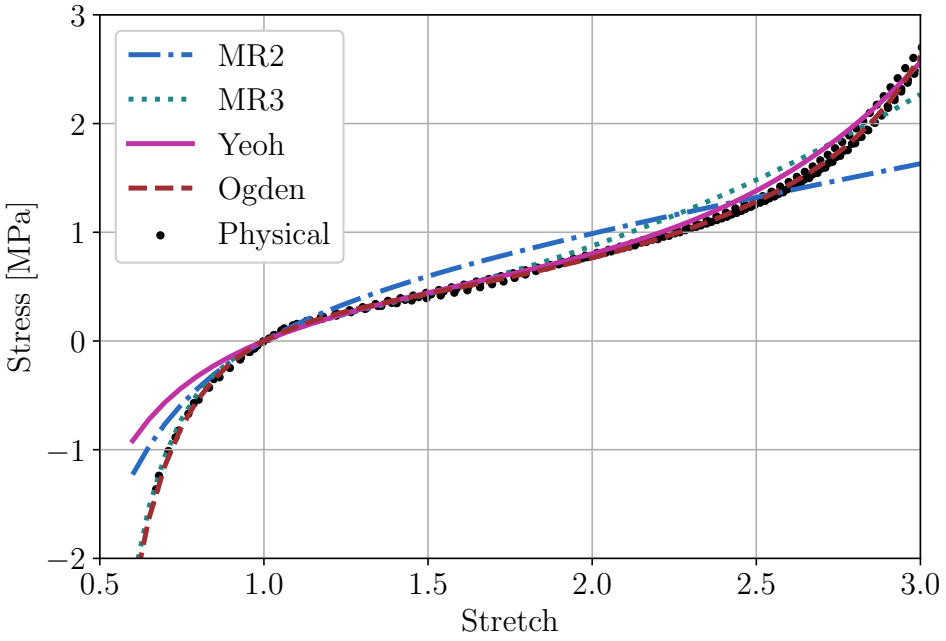

Figure A.11: Material models as fit to experimental data of Smooth-Sil 950

A.2.4 Bulk Modulus

The bulk modulus of a material is a measure of its compression resistance under loading. For certain rubber materials incompressibility can be assumed and the bulk modulus need not be measured. This section investigates the sensitivity of the silicone-rubbers used in this research to determine whether incompressibility can be assumed or whether bulk modulus needs to be characterised. Bergstrom (2015) provides a detailed summary on the bulk modulus of polymeric materials. This current section is adapted from their work and attempts to cover the particulars concerning the presented research.

For most applications of silicone rubber the material bulk modulus need not accurately be known in order to get an accurate FE model. The reason for this is that the majority of loading modes that silicone can be subjected to are largely insensitive to bulk modulus. On the other hand, applications exist where the bulk modulus is the only parameter that has an impact on the behaviour, such as the compression of an o-ring into a groove. It was required to determine the sensitivity of silicone to inflation loads and whether the bulk modulus had to be determined accurately. A bulge infla-

tion test was therefore performed. This loading mode involves a section of material that is clamped around its periphery and inflated to form a semi-sphere. Figure A.12 shows the centre height of the sphere as the pressure is increased for three different bulk moduli.

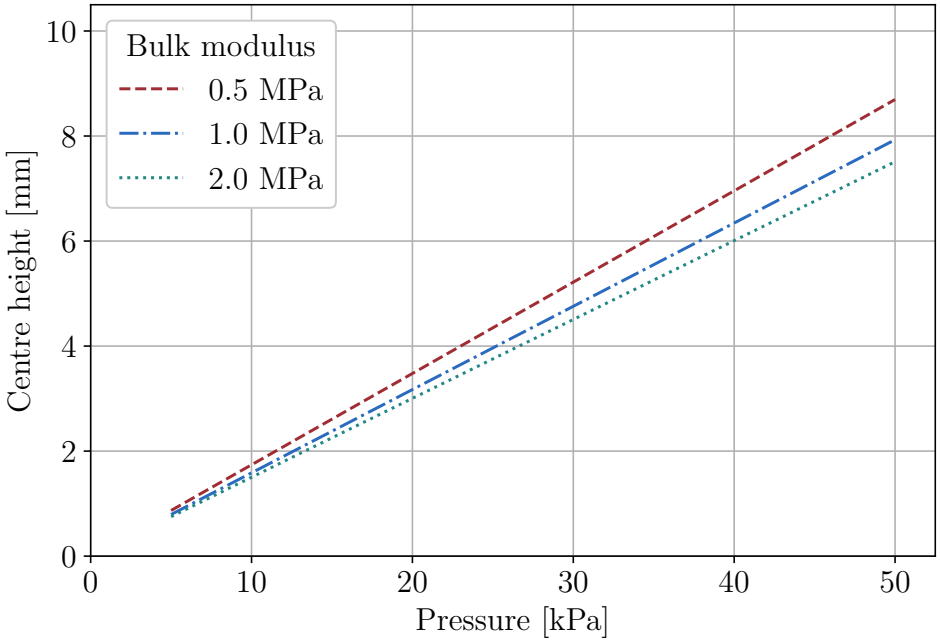

Figure A.12: Sensitivity to bulk modulus of a Mold Star 15 sample under a bulge inflation load, shown here as the centre bubble height for increasing pressure

These simple demonstrations show the dependency the results have on the loading condition and whether bulk modulus needs to be characterised accurately. Since the primary loading mode in this research is inflation, and that preliminary tests confirmed the dependence, it is required to accurately characterise the bulk modulus for all three silicones used in this project.

The bulk modulus of a polymer can be measured using one of three different experimental techniques:

1. Uniaxial tension or compression testing using DIC where both axial and transverse strains can directly be measured simultaneously. These measurements can then be used to calculate Poisson's ratio and from there the bulk modulus.

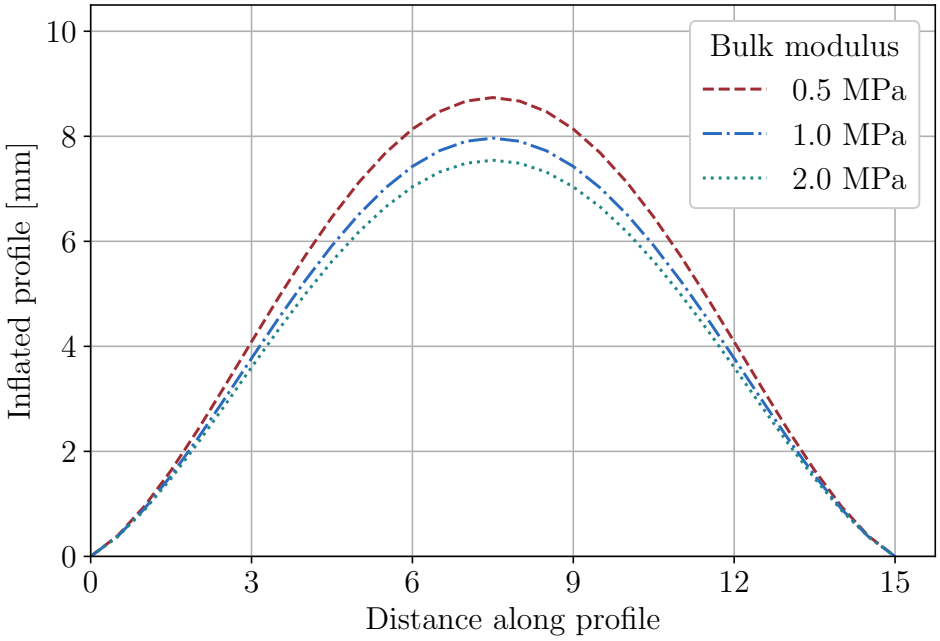

Figure A.13: Sensitivity to bulk modulus of a Mold Star 15 sample under a bulge inflation load, shown here as the cross-sectional profile along the circle diameter

2. Pressure-volume-temperature (PVT) testing. In this technique, the specific volume of a material is measured as a function of the applied pressure and temperature.

3. Confined compression test. In this technique, a cylindrical specimen is inserted into a thick-walled cylinder, and then compressed using a piston of similar diameter. The force-displacement response of the piston and the strain on the outer surface of the cylinder need to be measured. The pressure-volume response can be determined using this data and from there the bulk modulus.

The inability of using conventional strain measurement techniques on silicone-rubbers requires that DIC be used in any case. Therefore it is possible to measure the data required for the bulk modulus simultaneously with the stress-strain response. For linear elastic materials the bulk modulus, κ, can be calculated if the Poisson's ratio, ν and elastic modulus, E are known:

$$\kappa = \frac{E}{3(1-2\nu)} \tag{A.4}$$

where

$$\nu = -\frac{\varepsilon_y}{\varepsilon_x} \tag{A.5}$$

with ε_x and ε_y the strain measurements in the axial and transverse directions respectively. However, the silicone-rubbers are elastic, but not linear. To this end, the Poisson's ratio and bulk modulus become a function of axial strain. The above process was followed for the Mold Star 15 and Smooth-Sil silicones with the results shown in Figures A.14 and A.15.

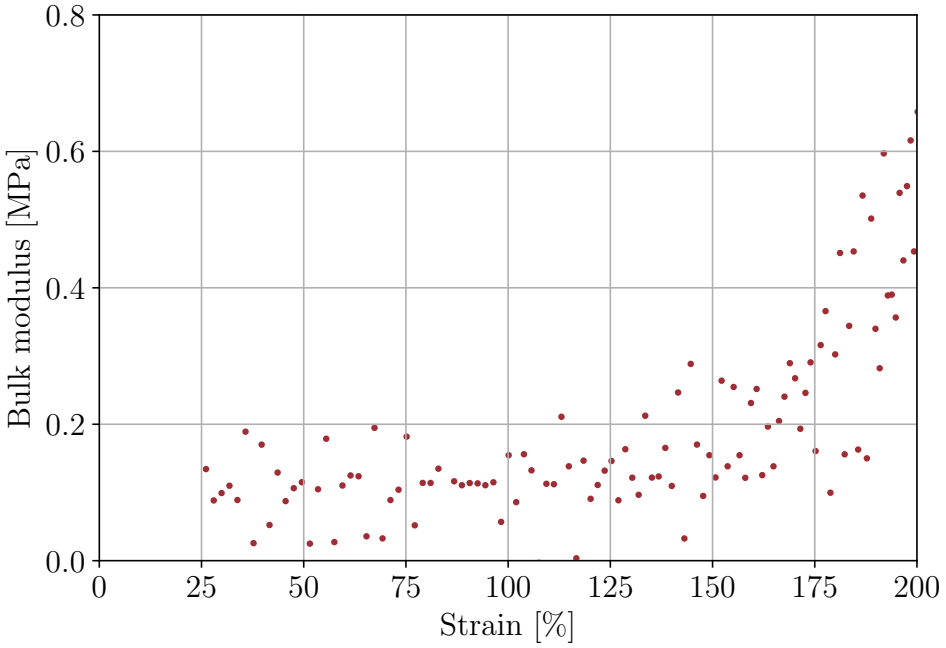

Figure A.14: Bulk modulus for Mold Star 15

The constitutive equations implemented in FE software can only process constant bulk moduli entries by and large. Incorporating a nonlinear bulk modulus is not a trivial task. To this extent, preliminary simulations were run and the strain range of interest determined as 0–150 %. The average of the bulk modulus of each silicone was calculated over this range and included as a constant value in the simulations, Table A.5.

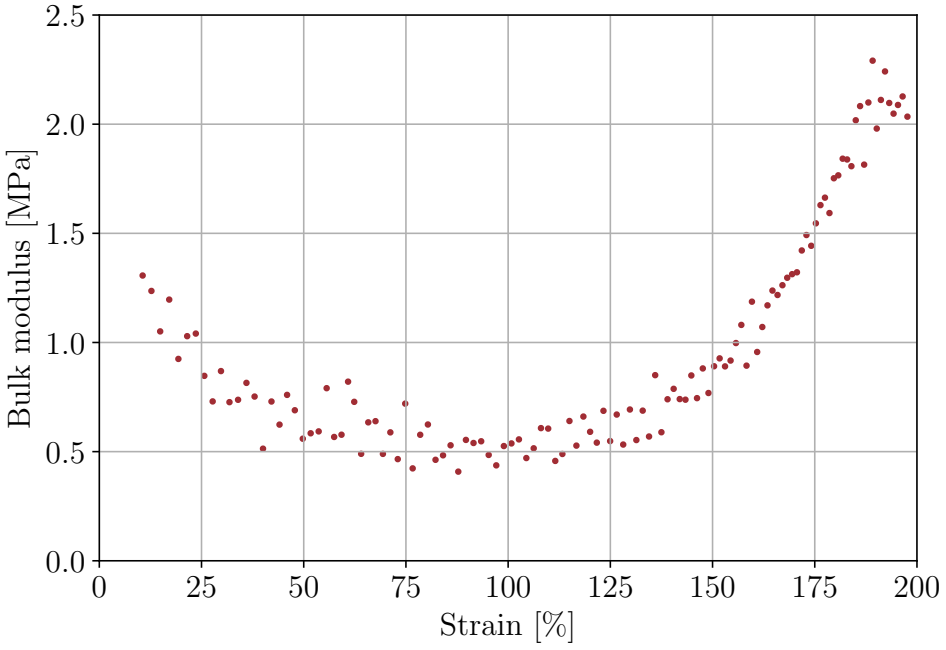

Figure A.15: Bulk modulus for Smooth-Sil 950

Table A.5: Bulk modulus of different silicones

Material	Bulk Modulus [kPa]
Mold Star 15	119
Smooth-Sil 950	679

A.2.5 Thermal Expansion Coefficient

The impact that the thermal expansion of the silicone could potentially have on the inflated shape of an actuator was not available in literature. The thermal expansion coefficient of silicone is not readily available in material data sheets. A simple test procedure was created whereby this could be measured using DIC.

A flat rectangular strip for each of the three silicones was cast between two glass panes spaced at 1.4 mm and tested on an individual basis. Each sample was clamped at the one end and allowed to hang down freely. A Fluke Ti 30 Thermal Imager was set up to focus on the sample and keep track of the temperature. A heat gun was used to heat the sample to 100 °C taking care to ensure an even heat distribution without damaging the speckle

pattern. The range 100 °C–85 °C was used to allow any local heat spots to dissipate. Ten images were taken over the interval 85 °C–20 °C using the DIC system. These images were processed using the StrainMaster software and the resulting strain field exported for post-processing to determine the thermal expansion coefficient in Python.

The thin silicone strips used cooled down fast. Trial-and-error experimentation showed that it was simpler to take measurements while the sample was cooling down from a maximum temperature. The alternative was to heat the sample and take measurements after consecutive incremental heating cycles. This proved tedious and inaccurate.

A linear relationship can be seen in the temperature-strain plot shown in Figure A.16 for all three silicones. The linear thermal expansion coefficient of a material can be calculated as

$$\alpha_{lin} = \frac{\Delta\varepsilon}{\Delta T} \tag{A.6}$$

where $\Delta\varepsilon$ is the change in engineering strain and ΔT the change in temperature. The linear thermal expansion coefficients are given in Table A.6.

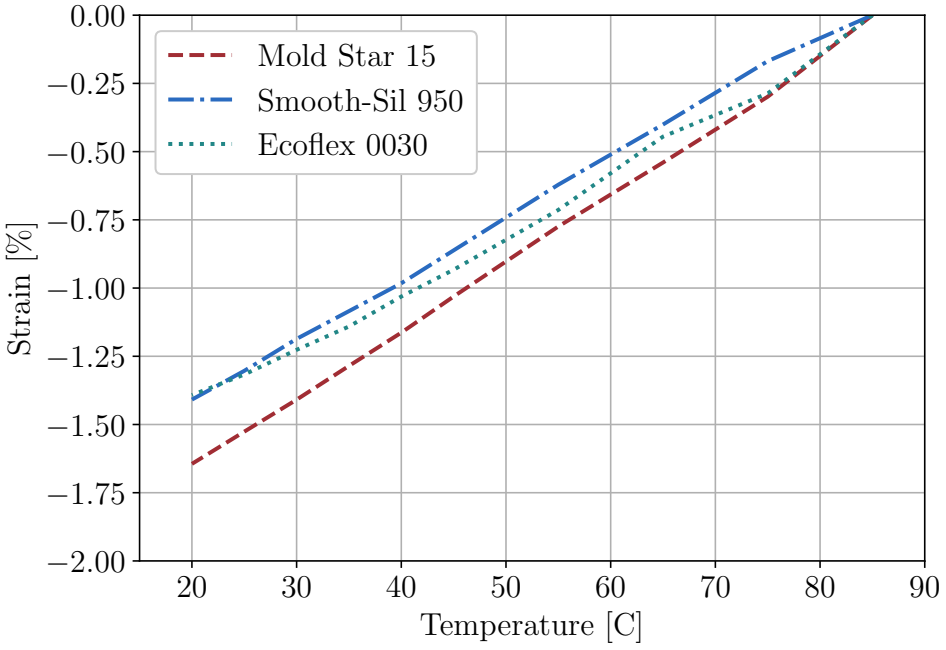

Figure A.16: Linear thermal expansion strain of silicone as subjected to a temperature loading

Table A.6: Linear thermal expansion coefficients of the three silicones in $[\frac{\mu mm/mm}{^{\circ}C}]$

Ecoflex 0030	Mold Star 15	Smooth-Sil 950
214.2	245.3	215.9

Appendix B

Experimental Details of Bimodal Actuator

B.1 Bilinear Material

B.1.1 Sample Manufacturing

The silicone, paper, and composite material samples were manufactured to identical geometries and dimensions, Figure B.1. Silicone matrix samples were cast in similar moulds as used for manufacturing of the composite materials, resulting in samples with a thickness of 5 mm. All samples were mixed and degassed before casting in a two-part mould. Samples were cured for 20 min at 70 °C. Paper tabs were embedded in the grip area of each matrix sample to facilitate the tensile testing. Preliminary tensile testing showed that the paper tabs were easier to consistently grip than the bulk silicone. Gripping the bulk silicone slab resulted in the initially flat sample bulging out and also led to slippage within the grip.

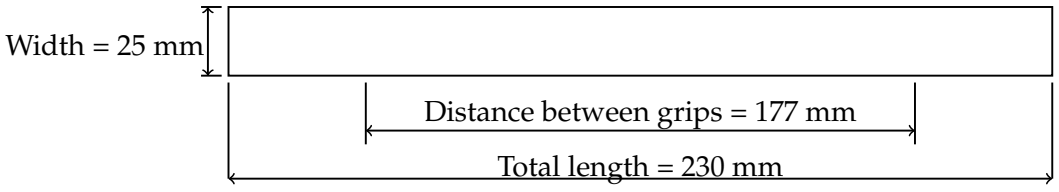

Figure B.1: Specimen geometry used for all uni-axial tensile testing of the paper, silicone and composite materials

Composite samples were cast with a full length paper strip embedded. The silicone fully covers the top and bottom surfaces of the paper, Figure B.2. The composite materials were tested according to the same procedure as was used for the silicone matrix samples. A two-part mould, manufactured using fusion deposition modelling 3D printing, was used to cast the composite material in. These moulds were designed with a split along their length to accommodate the paper layer in the middle and ensure a continuous distribution of uncured silicone prepolymer along the entire length of the sample, Figure B.3. The two halves fit together by sandwiching the paper layer between interlocking teeth. These interlocking teeth are spaced according to the desired crimp ratio. The paper layer is preconditioned with the required triangular pattern being folded prior to insertion into the mould. The updated mould that yielded better results is shown in Figure B.4.

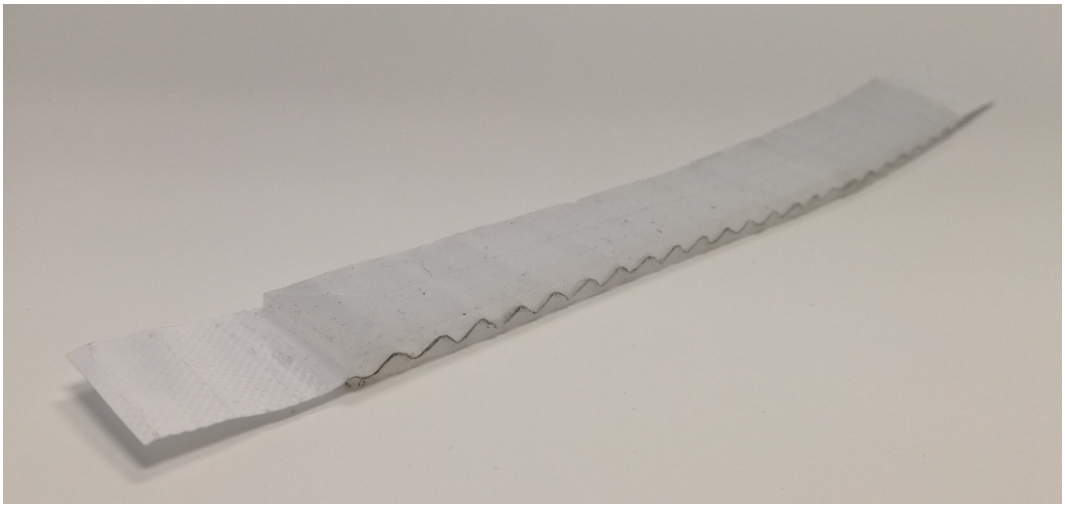

Figure B.2: Specimen of the bilinear material with crimp ratio of 0.2, showing the crimped paper layer as black, the silicone slab that adheres to the center section as well as the paper tabs that extend from the silicone slab

B.1.2 Physical Testing

Four bilinear composites of each crimp ratio were manufactured and tested. The experimental setup was similar to that used in Appendix A for the uniaxial tensile response of the silicone dumbbells. These tests were performed

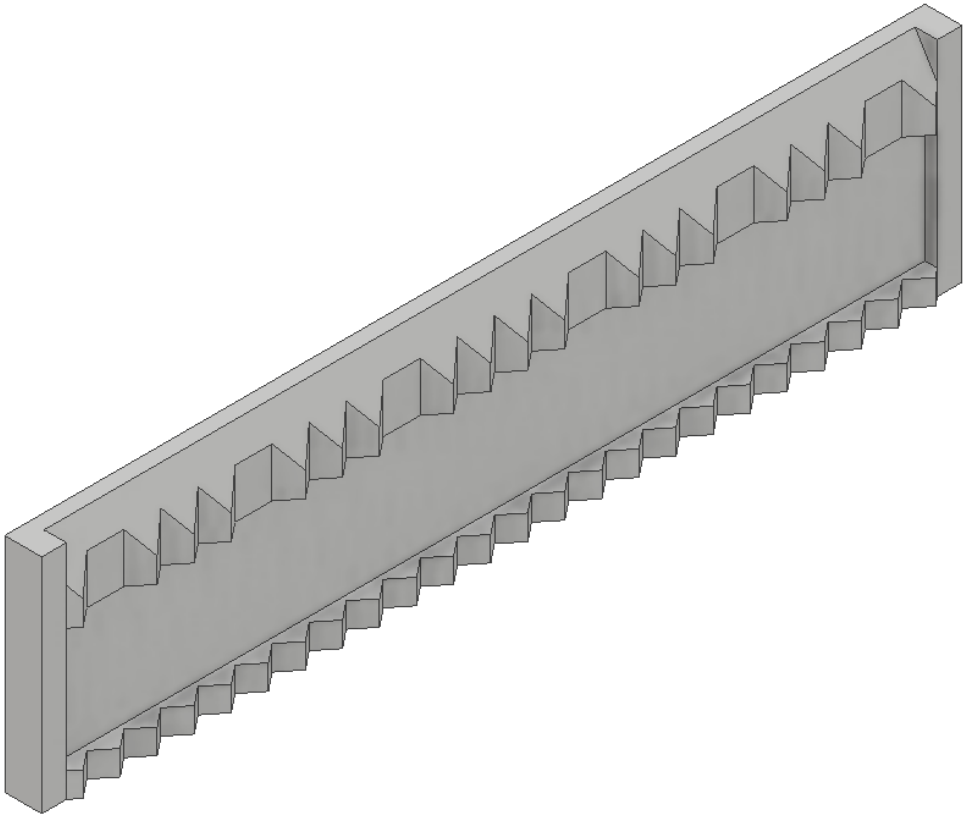

Figure B.3: One half of the original mould used showing the tapered edge leading into the region that clamps the crimped paper as well as the gaps used to pour the silicone through.

on an MTS Criterion tensile test device with a 500 N HBM (S2M) load cell. Strain was measured using digital image correlation (DIC) hardware of the strain master system from LaVision with the DaVis software package. Black paint was used to apply a contrasting speckle pattern to the surface of the sample. The samples were individually painted and immediately tested. This allowed for deformation to be measured whilst the paint was still wet, thereby mitigating the unwanted effect of paint cracking off. A speckle pattern that could be reproduced consistently was used. Additional LED lighting was required, but was positioned such that glare from the reflective silicone surface would not hinder the images of the recorded speckle. Four of the plain Purco 80 gsm white copy paper samples were cut and tested as per the ASTM D828-16 standard using a similar experimental setup as above.

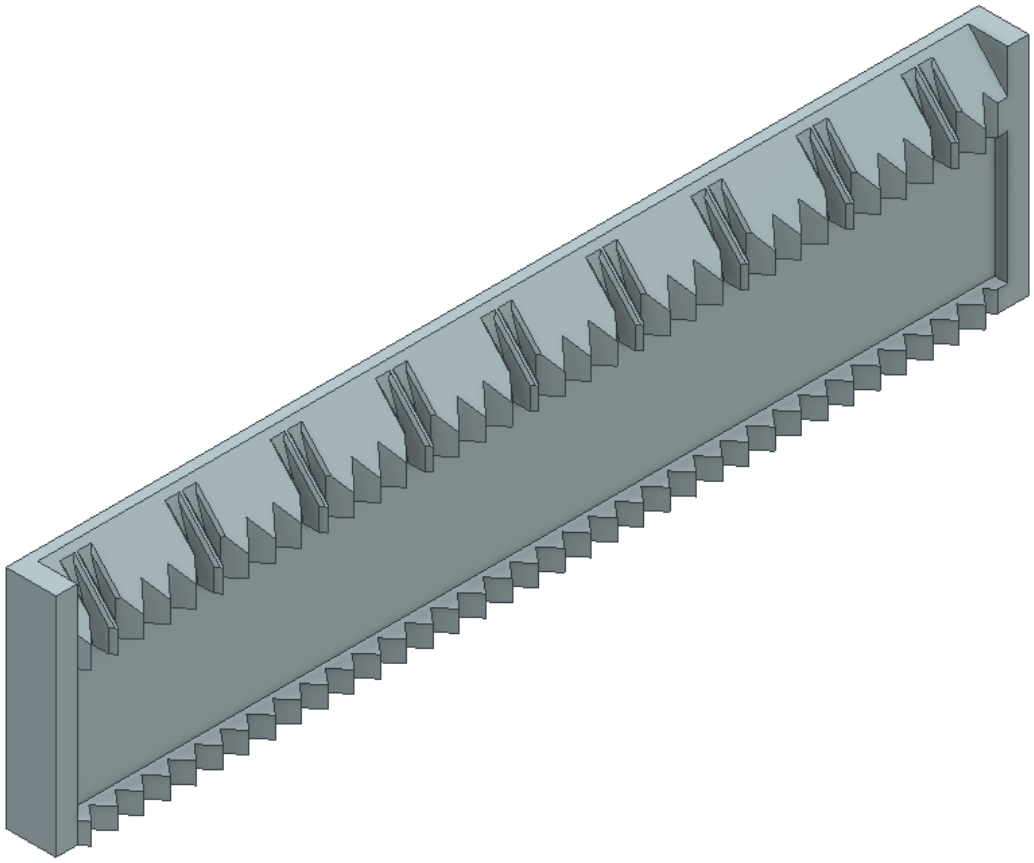

Figure B.4: One half of the updated mould used showing the tapered edge leading into the region that clamps the crimped paper as well as the small struts that offer better support to the paper layer

B.1.3 Ogden Parameters

The parameters for the three-term Ogden model of each crimp ratio are given in Table B.1, with all μ terms in N/mm^2 and all α terms dimensionless.

Table B.1: Ogden parameters for the three different bilinear materials

Crimp ratio	μ_1	α_1	μ_2	α_2	μ_3	α_3
0.2	20.32	2.24	5.48e-4	40.59	-19.08	2.38
0.25	5.20	15.68	1.18	0.20	-5.21	15.67
0.3	2.67	0.0224	1.013	0.052	6.233e-7	39.09

B.2 Manufacturing of Physical Actuators

The basic steps involved with manufacturing a bimodal actuator, with reference to Figure B.5 indicated in the square brackets, are as follow:

1. Thoroughly mix a total of 50 g of Mold Star 15 and degas it in the mixing cup using a vacuum chamber. Hold the vacuum until no air bubbles can be seen escaping from the pre-polymer.
2. Cast the main center section of the actuator from Mold Star 15. Apply mould release to all parts before slowly pouring the pre-polymer into the mould [A1 and A2].
3. Degas the entire mould in a vacuum chamber for 10 min. Slowly release the vacuum once done.
4. Top-up the mould until it is overfilled.
5. Cast the 1, 2, and 3 mm thin strips in the appropriate moulds.
6. Allow the various castings to cure at room temperature for the recommended cure time of 6 h.
7. Use a sharp cutting blade to slice off the cured, excess silicone from the main center section. This method mitigates the forming of a meniscus and thereby uneven thickness distribution [B].
8. Ensure that the thickness of the thin strips is within ± 0.05 mm of the required thickness. This value stems from the tolerance on the 3D printed moulds
9. Use Sil-Poxy to glue a 1 mm strip of Mold Star 15 to the underside of the main centre section to seal the open voids. Apply the Sil-Poxy as a thin, even layer to the Mold Star 15 strip [C].
10. Use Sil-Poxy to glue a 2 mm strip of Smooth-Sil to the top surface of the main center section. Apply it as a thin, even layer to the main center body [D].
11. Cut a 15 mm wide strip down the length of the pre-made bilinear composite material. Use a new cutting blade and run it along a steel ruler to ensure a smooth cutting surface [F].

12. Use Sil-Poxy to glue the bilinear composite material to the bottom of the main actuator section (On top of the Mold Star 15 strip) [G].

13. Insert a new medical syringe through the thick slab of silicone attached to the base unit until it has punctured the first void.

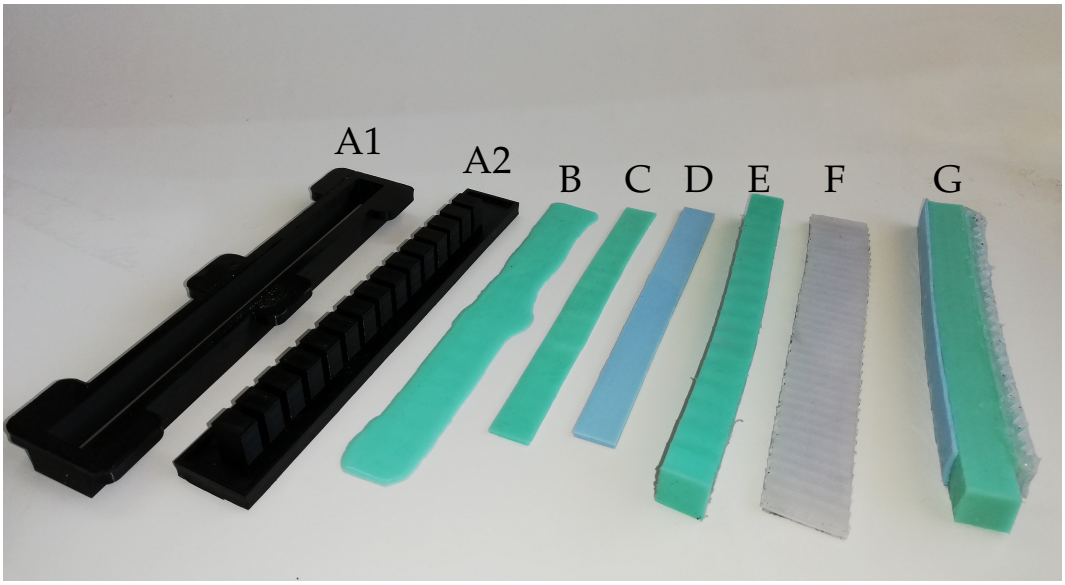

Figure B.5: Individual components for manufacturing a bimodal actuator.
A1 - Part 1 of the 3D printed mould
A2 - Part 2 of the 3D printed mould
B - Section of silicone that is sliced off due to overfilling the mould
C - 1 mm thick strip of Mold Star 15
D - 1 mm thick strip of Smooth-Sil
E - Mold Star 15 actuator as it is removed from the 3D printed moulds
F - Bilinear material as it is removed from the mould, before it is cut to size
G - Manufactured bimodal actuator

B.3 Experimental Setup of Bimodal Actuators

An outline of the testing procedure of the bimodal actuators is discussed and a supporting picture of the experimental setup provided in Figure B.6:

1. Attach paper with a printed chequerboard pattern to a steel cross-bar using adhesive tape. Ensure that the pattern is properly aligned vertically.
2. Place the base of the actuator into a 3D printed block to support it, Figure B.7a.
3. Clamp the support block with the actuator inside against the steel beam and align it so that it hangs down vertically. The initial position should be in line with the vertical line of the chequerboard pattern.
4. Attach a digital camera in portrait orientation to a tripod and position it so that the center of the actuator is in the center of the camera frame. The camera must be set to its highest resolution setting.
5. Take a reference photo of the initial, uninflated state.
6. Connect the air supply tube to the needle using a specially made aluminium adapter, Figure B.7b.
7. Connect the pressure transducer to the supply line.
8. Using a pneumatic pressure regulator; increase the pressure to 10 kPa and take a photo.
9. Gradually increase the pressure in increments of 5 kPa, taking photos of every state until the actuator ruptures.
10. Throughout testing ensure that the actuator is airtight and that there are no air leaks in the system.

Figure B.6: Photo of the experimental setup used for the bimodal actuator. In this figure the chequerboard pattern, air supply tube, surgical needle, G-clamp and the pressure sensor are all visible.

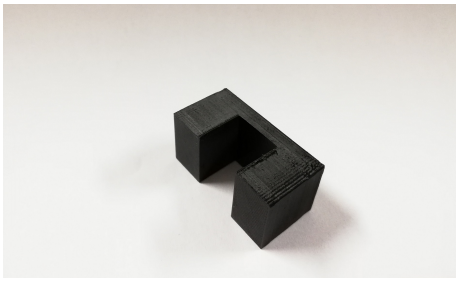

(a) 3D printed support block that attaches to the actuators' base

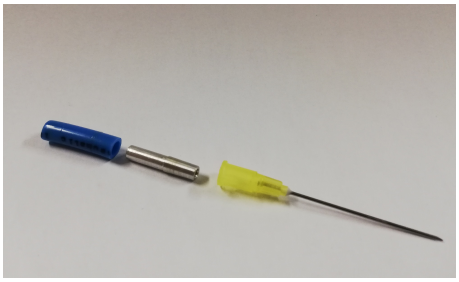

(b) Adapter from supply tube to needle

Figure B.7: Accessories used for testing the bimodal actuators

Appendix C

Siemens NX 12: Tips and Tricks

Siemens NX 12 has many built-in functions available that streamline work processes, but with sometimes difficult to find documentation, implementation can be hindered. This appendix covers some functionality that was beneficial to this project.

C.1 Exporting Specific Nodal Displacements

Python packages such as pyNastran can be used to interface with Nastran's input and output files. The drawback of this is that Nastran's `.op2` result files contain additional information creating a larger file. In most instances where post-processing of results is done, the majority of this information is not required. This then comes at the cost of importing large files into memory while the required information is extracted.

NX 12 allows that the output of selected nodes be exported as punch (`.pch`) files - a structured file with plain text formatting. The steps to perform this are explained:

1. In the `.fem` file, create a `Group` of the nodes for which the final output is desired. [`Home` $\Rightarrow$ `Utilities` $\Rightarrow$ `New Group`]

2. In the `.sim` file, edit the `Solution` and alter the `Output Requests` to the outputs, formatting and nodal groups which should be exported. [`Simulation Navigator` $\Rightarrow$ `Solution` $\Rightarrow$ `Case Control` $\Rightarrow$ `Output Requests` $\Rightarrow$ `Output Medium: Punch; Entity: Group`]

3. The `.pch` file is exported at successful completion of the simulation.

This file format lists nodes in chronological order starting at the first converged increment and finishes at the last converged increment where $T_{solution} = T_{end}$.

C.2 Mooney-Rivlin Coefficients in Matrix Form

Although the Ogden constitutive equations were used in the final results, the Mooney-Rivlin model was used during the initial phases of this research. Many FE analysis pre-processors list the coefficients in terms of their widely used names (C_{10}, C_{01}, etc.). NX requires that these coefficients be input in a 5x5 matrix, but does not provide any indication to the formatting thereof.

The coefficients as written to the data deck can be found in the NX 12 Nastran Quick Reference Guide. Through trial-and-error the correct coefficient names can be linked to the different coordinates in the following matrix:

$$\begin{bmatrix} 0 & C_{01} & C_{02} & C_{03} & 0 \\ C_{10} & C_{11} & C_{12} & 0 & 0 \\ C_{20} & C_{21} & 0 & 0 & 0 \\ C_{30} & 0 & 0 & 0 & 0 \\ 0 & 0 & 0 & 0 & 0 \end{bmatrix}$$

C.3 Pressure Dependent Material Property

For the design algorithm in Chapter 4 to work in a computationally efficient method, it was required that the material properties of the reduced-order model in Chapter 5 be linked to the internal pressure at the current solution time. NX 12 does not offer this functionality, but does provide a work-around by allowing a material to be temperature dependent. The program functionality that facilitates this and the steps required to make it work are provided here.

Setting up the model for a variable temperature loading:

1. Create a new `Formula Field, Independent` set to `time` and `Dependent` set to `temperature` with the `Expression` as $(\text{time}/(1[\text{sec}]))$
2. Create a new `Temperature Set, Initial/Stress Free Temperature` with `Default Temperature` as 0. Card Name `TEMP(INIT)`
3. Create a new `Temperature Set, Temperature Load` with `Default Temperature` as 0. Card Name `TEMP(LOAD)/DTEMP/TEMPD`
4. Within the last new set, create a `Temperature-Time Assigned`, select the filler material meshes and select `Specify Field` to be the initially created `Formula Field`

Defining the polynomial function:

Create a `Formula Field`, `temperature` will be preselected as the `Independent field` and `stress` will be the preselected `Dependent field`.

To change Eq. 5.2 from pressure-dependent coefficients to temperature-dependent, the P variable must be substituted for $P = \frac{T_{solution}}{T_{max}} \times P_{max}$ in $E = 0.0643 - 1.82P + 12.4P^2$ with pressure in MPa and E then also in MPa, where T_{max} refers to the maximum solution time (input as a pre-defined variable - typically 1 s in this work) and P_{max} the maximum applied pressure in the model. NX does however not allow that any number with a unit of celsius (C, in NX) be scaled. A work-around is to create a temperature difference (dC, in NX) and then dividing by another fictitious temperature difference. The `Expression` entry is then changed to the following mathematical expression:

$$\begin{aligned} & 0.0643[\text{MPa}] \\ & -1.82 \times ((\text{temperature} - 0[\text{C}])/(1[\text{dC}]) \times 0.045) \\ & +12.4 \times ((\text{temperature} - 0[\text{C}])/(1[\text{dC}]) \times 0.045)^2 \end{aligned} \tag{C.1}$$

C.4 Automated Geometry and Mesh Update

A powerful feature of NX 12 is the FE processor that is linked to a CAD engine within the same software. Changes to the physical geometry of a part therefore only require a mesh update and not a complete remesh. Linking this capability to an automated script that can run without user-input favours the use of certain tools over others. This section highlights these preferences where multiple CAD bodies are required – the process is simpler when only one solid part is analysed.

1. Create the solid CAD part in the Modelling application. As dimensions are added, name these using some descriptive term. Changing the values of these dimensions can be recorded in a Journal file which can easily be edited as part of a script. NX 12 allows dimensions to be linked to an external spreadsheet as well. The drawback however is that the procedure that updates the geometry after the spreadsheet has been changed, cannot be performed from a Journal file. This functionality was lost with the upgrade to NX 12.

2. When multiple parts are used where different meshes need to line up and be linked together, two different methods exist.

    a) Generally the more stable option is to manually ensure that meshes line up where after a tool that removes duplicate nodes can be used to sweep through all the parts and remove nodes within close proximity to each other. Depending on how the mesh was originally created, the association between the polygon geometry and the mesh can be lost using this approach. This lost association leads to problems later when loads and boundary conditions in the `.sim` file are applied to polygon surfaces. These loads are not transferred to the mesh, and the solution will continue with a warning and not an error. This can lead to incorrect results that are easily overlooked.

    b) The alternative method is to use Mesh Mating which is a single tool that ensures coincident meshes and duplicate node removal. If coincident meshes are not possible, rigid elements or multi-point constraints will be created to allow parts to be glued; the

introduction of these elements is not always desired. Trial-and-error showed the steps that deliver the most consistent results are when different polygon bodies are placed relative to each other as desired and Mesh Mating conditions applied to these. A hexahedral mesh can then be created and all the required loads and boundary conditions applied to the various polygon faces. Association between the polygon geometry and mesh is preserved, but experience showed that for large changes to certain dimensions, the numbering of the polygon bodies is changed, leading to errors.

3. A Journal can then be recorded where the dimensions of the polygon body are changed, the mesh updated in the `.fem` file and the model submitted in the `.sim` file. A Python script that edits this Journal with the required dimensions can be created and run.

Appendix D

Numerical Modelling Simplifications

The impact of the various numerical simplifications made throughout the research is investigated in this section.

D.1 Effect of Ignoring Connecting Voids

While constructing the 3D numerical models, the connection/passage between voids of adjacent units was ignored in order to simplify the geometry. The effect this has on the overall shape and deformation of the actuator is investigated here using the same random orientation vector as used in Chapter 5. Results are shown for a model where adjacent elements were removed from the mesh, creating a passage for air to flow, Figure D.1, and a model where the simplification is implemented. The outer nodes on the centreline of the actuator were exported and plotted for both instances, Figure D.2.

A noticeable difference is evident. To quantify this, the maximum Euclidean distance between similar nodes on the two models was calculated and found as 11.7 mm. The overall shape of the model remains intact and the 11.7 mm distance represents an error of 4.5 % and 6.5 % for the X and Y-displacements, respectively.

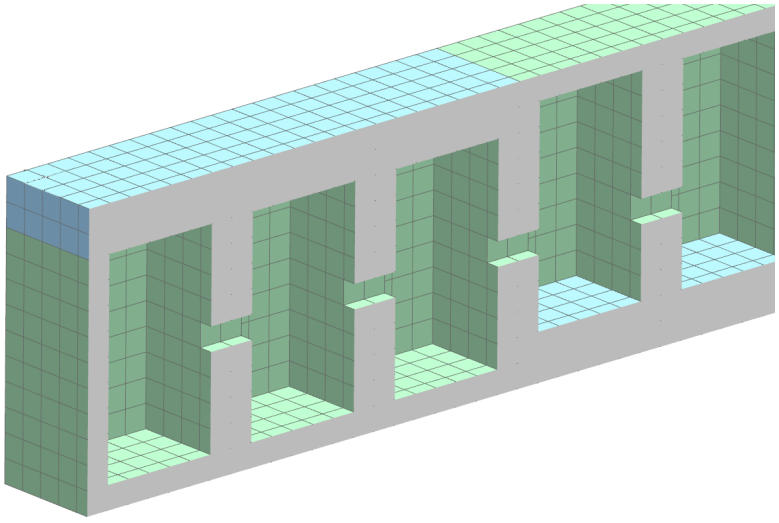

Figure D.1: Cross-sectional view of the actuator used to study the effect of removing the passages that connect adjacent voids

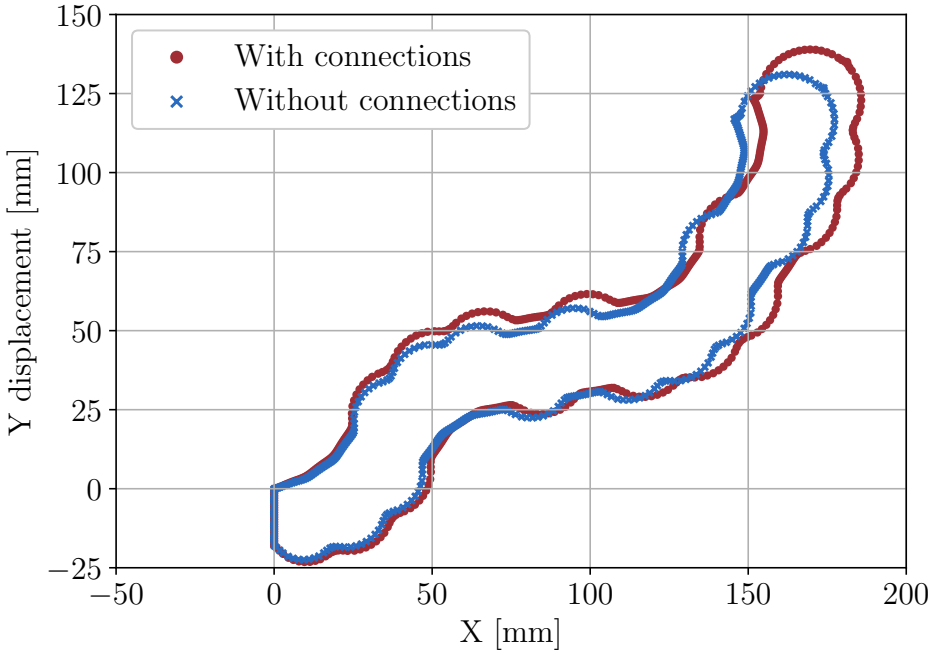

Figure D.2: Effect of modelling the connection passages between articulating units

D.2 Effect of Simplifying the Base Unit

The physical actuator required that a block of silicone be attached to the base of the actuator for two reasons; ensuring an air tight seal while inflating it; and creating a means to clamp it while testing. For computational savings and for streamlining the work process, this additional block was not modelled as part of the optimisation loop. The effect of this simplification on the overall deformation was investigated using the two different models. A model was constructed that incorporates this additional block and was compared to an actuator using the simplified method of modelling it, Figure D.3.

The actuator that includes the accurate base unit and boundary conditions has a stiffer response to a pressure loading. The maximum Euclidean distance between similar nodes on the two models was calculated and found as 12.8 mm. The overall shape of the model remains intact and the 12.8 mm distance represents an error of 5.8 % and 8.4 % for the X and Y-displacements, respectively.

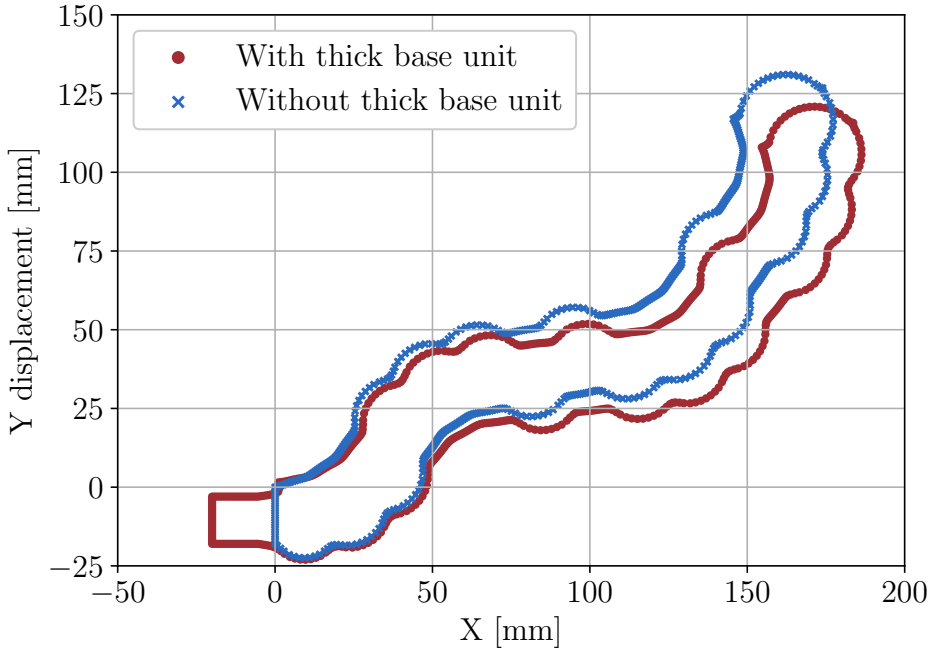

Figure D.3: Effect of ignoring the silicone slab on the base unit

D.3 Effect of Material Thermal Expansion

The actuators were manufactured and tested under similar environmental conditions. Nevertheless, the sensitivity of a small temperature fluctuation had to be determined. A 3D numerical model was created and subjected to a 10 °C temperature difference. The results before and after this temperature increase are shown in Figure D.4 for the same orientation vector used throughout this section. The maximum Euclidean distance between similar nodes on the two models was calculated and found as 2.08 mm. The overall shape of the model remains intact and the 2.08 mm distance represents an error of 0.4 % and 1.79 % for the X and Y-displacements, respectively. It must be noted that the 10 °C modelled is higher than the expected temperature swing for the working conditions used.

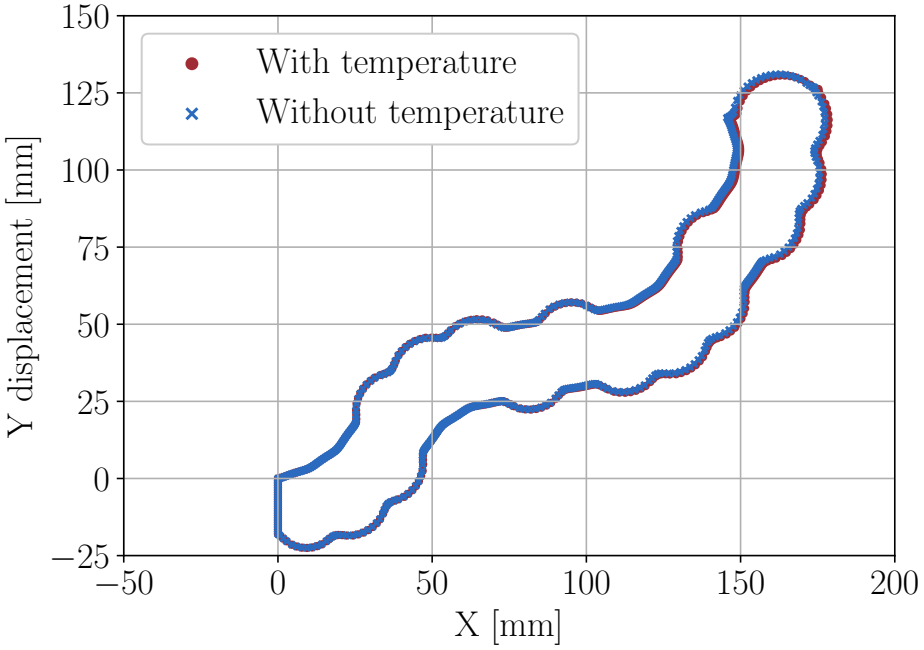

Figure D.4: Effect of a 10 °C temperature difference to an inflated actuator

D.4 Effect of Combining the Simplifications

A model was created where all three simplifications that were investigated separately, were added together in order to investigate the combined effect, Figure D.5. The maximum Euclidean distance between similar nodes on the two models was calculated and found as 13.85 mm. The overall shape of the model remains intact and the 13.85 mm distance represents an error of 9.52 % and 0.83 % for the X and Y-displacements, respectively. These simplifications superimpose to reduce the error in the Y-direction, but grow the error in the X-direction. The overall shape quantitatively matches that of the simplified method used.

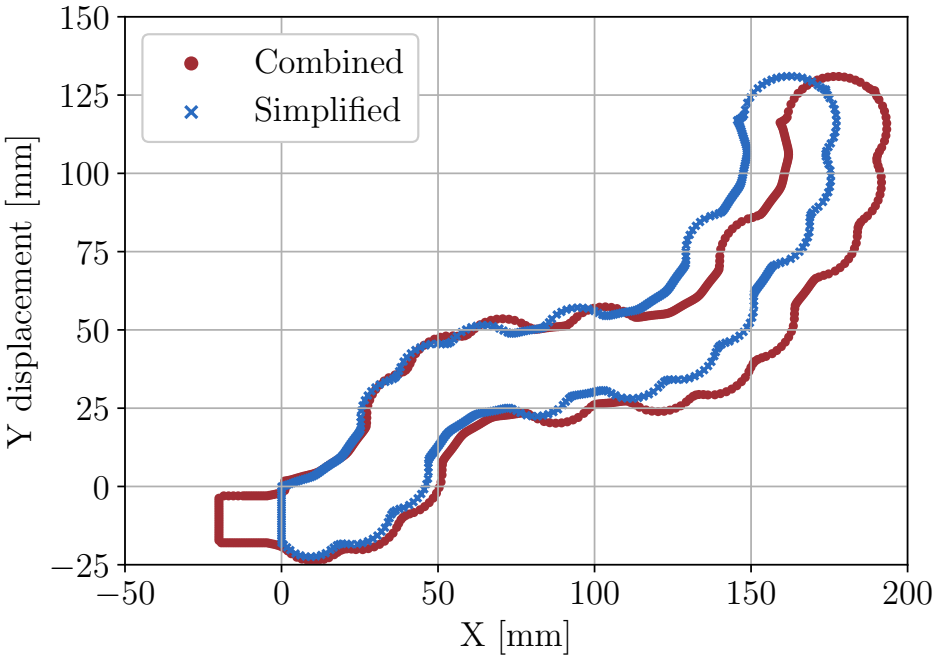

Figure D.5: Combined effect of numerical simplifications

Appendix E

Numerical Modelling Sensitivities

This appendix investigates the sensitivity of the numerical results to factors including tolerances in the 3D printed moulds and to load case simplifications while testing for the material properties. These factors are either too difficult or expensive to improve (using different technology 3D printers) or can erroneously be neglected without a complete understanding of the actual stress state of the part. Although similar technology (3D printers, finite element models, and soft materials testing) has been used in literature (Elsayed *et al.*, 2014; Alici *et al.*, 2017; Connolly *et al.*, 2015; Duriez and Duriez, 2013; Mohd Nordin *et al.*, 2013; Mosadegh *et al.*, 2014), no research has been found that investigates how a variation in these factors translates to the final product. Throughout the presented work an orientation vector, where all units are aligned in the same direction, is used. This configuration attempts to make the results more easily translatable to what has been used in literature.

E.1 Material Model Calibration

The experimental testing performed as part of a project is greatly dependent on the test equipment available as well as the loading states that are deemed important to characterise. This section shows the impact that different testing methods have on the final shape of an inflated actuator.

E.1.1 Experimental Data

Labs researching soft material related work will typically have access to a load frame with a set of grips to perform tensile testing along with a long travel extensometer for their strain measurements. Testing the compression behaviour of materials requires a different set of grips and a different method of measuring strain. It is therefore often overlooked. Soft pneumatic actuators (SPA), although inflated, were found to have a large compressive strain component in their deformed state. Material models that are only calibrated to tensile test data will need to be extrapolated to the compressive region when the FE analysis requires a relationship there.

Material models calibrated in MSC.Marc 2017.1 to tension-only data and to tension-compression data are shown in Figure E.1 for Mold Star 15, along with the experimental data points. Both these models predict the tensile response well, but the correlation degrades when extrapolated to the compressive strain region. The model calibrated using both loading states performs well over the tested strain range, but the model calibrated using only tension data extrapolates to an overly stiff compressive response.

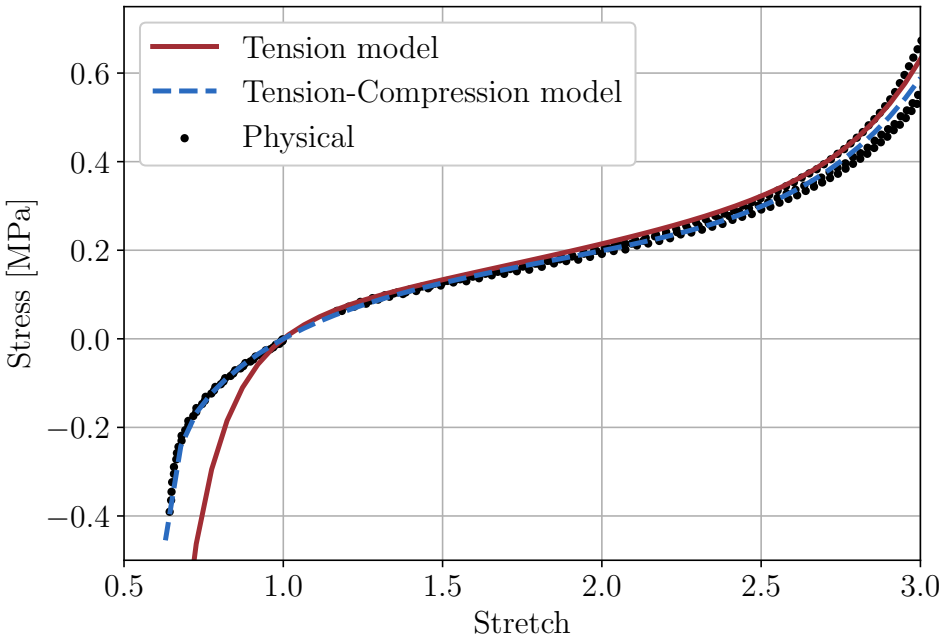

Figure E.1: Extrapolating material models of Mold Star 15 to strain regions outside of those used for calibration

The effect this has on the inflated actuator is pronounced, Figure E.2. In order for the model calibrated on tension data to match that of the more accurate actuator, the pressure must be increased from 45 kPa to around 85 kPa. Therefore great caution needs to be taken when calibrating hyper elastic material models for use in nonlinear simulations.

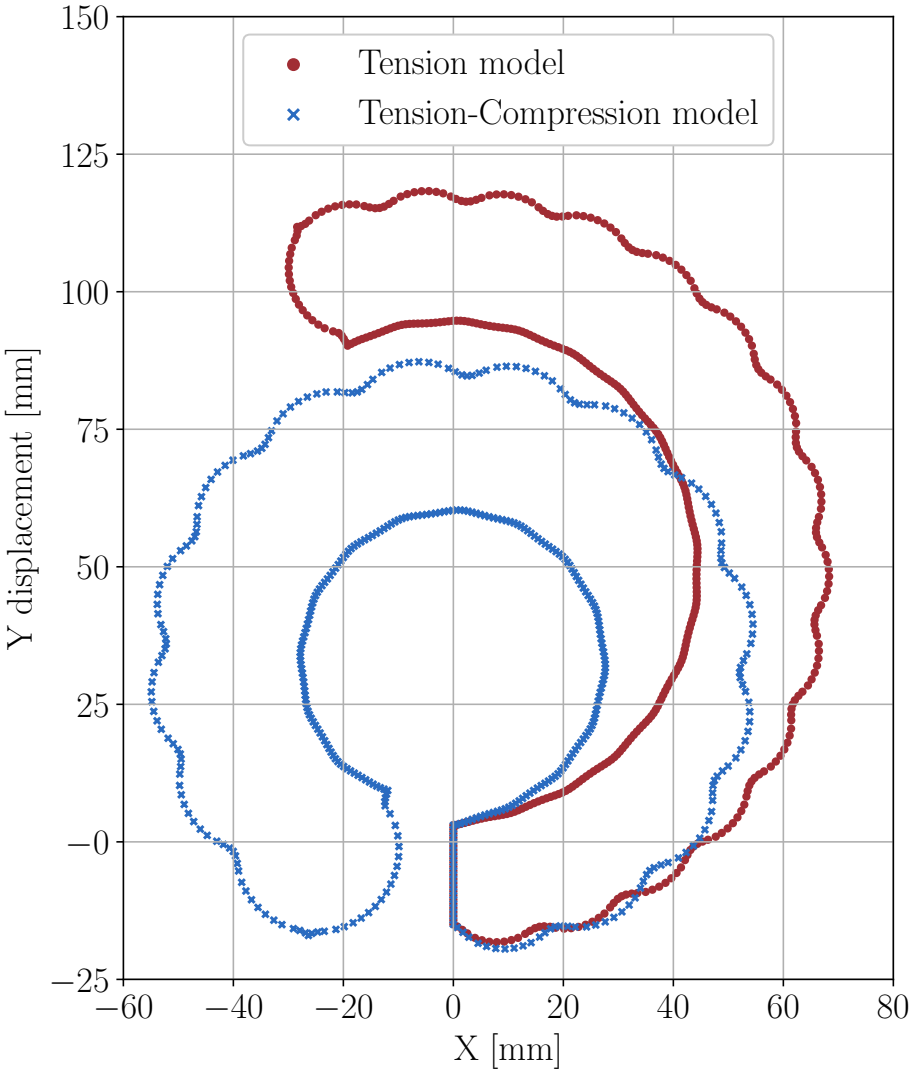

Figure E.2: Effect material model calibration has on the inflated shape of an actuator

E.1.2 Bulk Modulus

The bulk modulus was calculated using an appropriate method with the tools available to this research in Appendix A. More accurate methods of calculating this parameter however exist in literature, but the equipment is highly specialised and was not available. To this end, it is important to investigate the impact this difficult to determine parameter has on the inflated response of an actuator. The modulus was increased from the experimentally calculated value of 119 kPa to 5 % and 10 % of that value, Figure E.3.

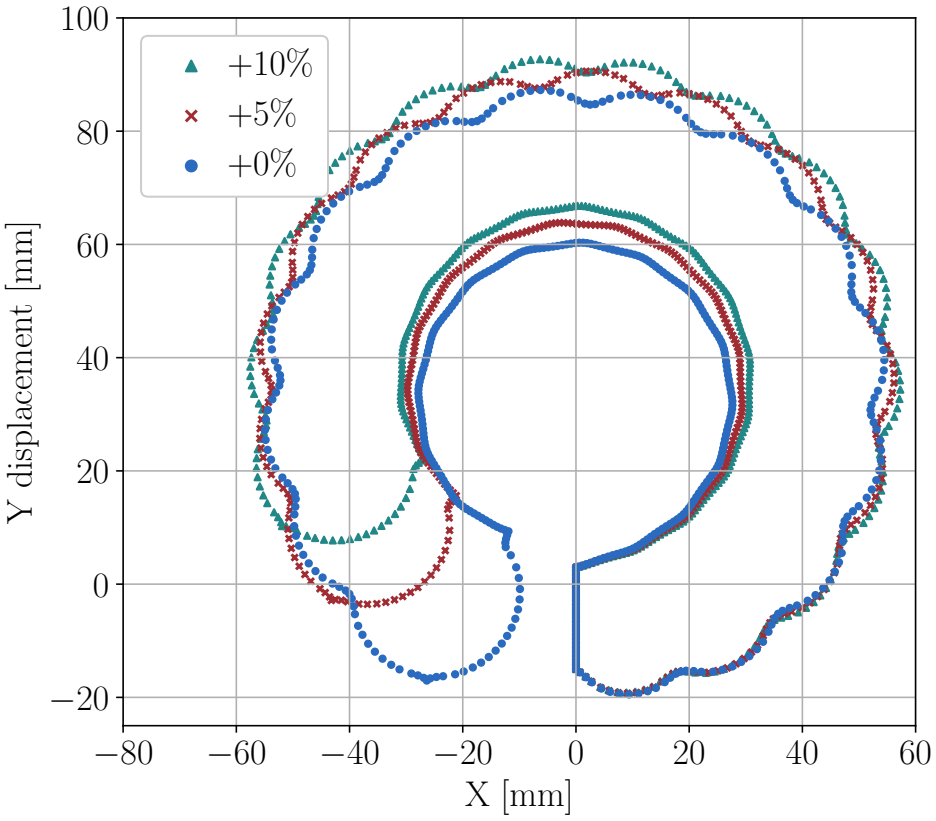

Figure E.3: Effect bulk modulus has on the inflated shape of an actuator

The results show a noticeable dependence on the bulk modulus. Further work would be required to gain a better understanding of this parameter and design a test device that can measure it more accurately. That work is

beyond the scope of this research, and as such the dependence on bulk modulus needs to be taken into account when viewing the correlation between numerical and physical results.

E.2 Manufacturing Tolerances

Amongst the different types of 3D printer technology available, fused deposition modelling (FDM) 3D printers are typically used for soft robotics research due to their lower cost. This lower cost however comes at the price of lower dimensional accuracy of which the effect on the manufactured actuators is unknown. The Wanhao Duplicator 6 3D printer used throughout this research has a quoted *positional precision* of 4 nm in Z and 12 nm in X, Y directions. This value is solely what the hardware and control system can achieve and does not translate to the printed part as it neglects the effect of warpage and shrinkage. Redwood (2019) presents the achievable *dimensional tolerance* of these FDM printers on manufactured parts as $\pm 0.2 - \pm 0.5$ mm.

How this tolerance affects the performance of the manufactured parts is investigated numerically. A fully parametrised CAD linked FE 3D model was created in Siemens NX 12 of which the dimensions can be changed as part of an automated script. This change in the CAD geometry relays to the FE analysis where the existing mesh can be updated accordingly. The results from the solution are exported as nodal displacements for the outer nodes along the center length of the actuator.

Only three of the geometrical variables constituting the CAD part were altered during this investigation: thickness of the two sides, thickness of the upper Mold Star layer, and thickness of the lower Smooth-Sil layer, Figure E.4. Tolerances on these variables were set to ± 0.1 mm of their designed values. A Python script was created that tests the two extremes of each variable independently and also randomly tests combinations of the variables for possible interactions. Each set of parameters is exported as a spreadsheet for further analysis, if required, before the simulation is completed. Self-contact was not enabled in the models. The sensitivity of the model, investigated using 30 different design input files, is presented in Figure E.5.

A large variation can be seen in the results when judging the angle that

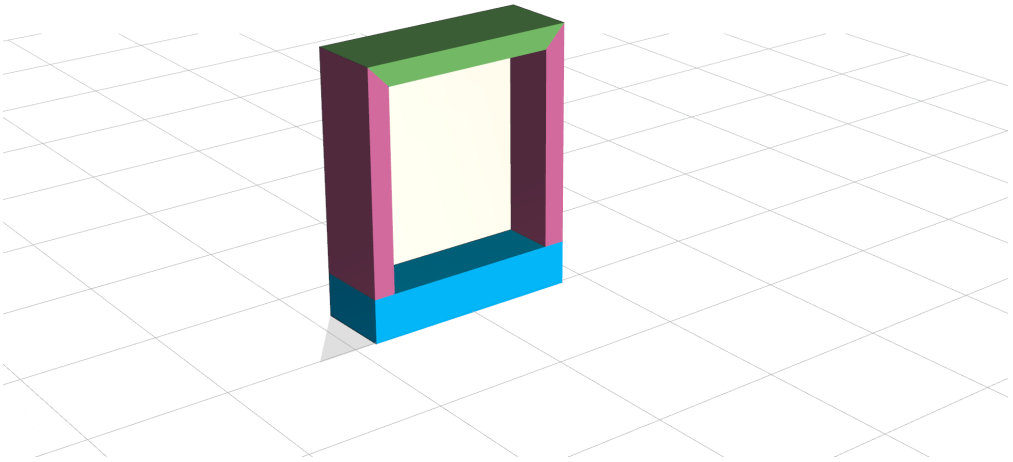

Figure E.4: Variables investigated during the sensitivity study were the thicknesses of the green, purple and blue sections of material. The articulating unit is shown here as a cross-sectional view along the width of the unit

Table E.1: Input parameters that translate to the minimum and maximum degrees of deformation as calculated during the sensitivity study

	Thickness measurement [mm]		
	Sides	Mold Star top	Smooth-Sil bottom
Minimum curl	1.578	1.597	2.910
Maximum curl	1.425	1.410	3.007

the actuator has curled. The input parameters resulting in the minimum and maximum curl angle were identified and are presented in Table E.1. These parameters show a strong connection between the thickness of the sides and the top surface of the actuator: thinner measurements lead to more deformation and vice-versa.

In contrast, the tighter tolerances (± 0.02 mm) possible with machined aluminium moulds were also investigated using 30 different simulations, Figure E.6. The tighter mould tolerances transfer to less possible variation in the manufactured actuators.

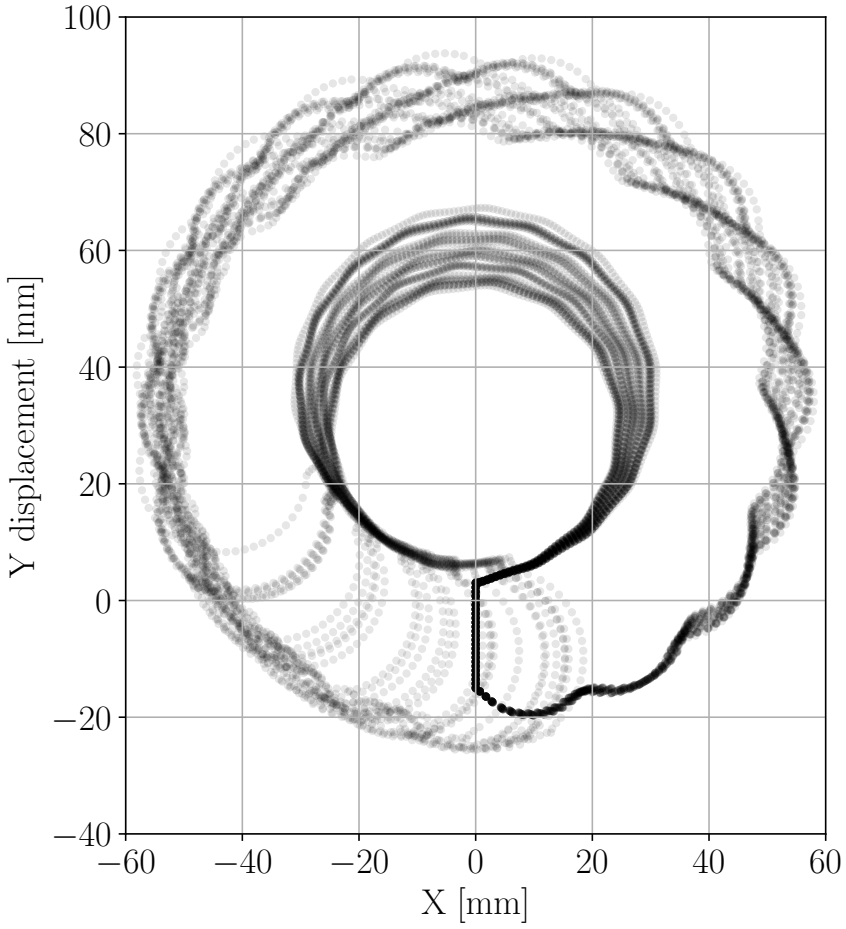

Figure E.5: Sensitivity of numerical model to a manufacturing tolerance of ± 0.1 mm

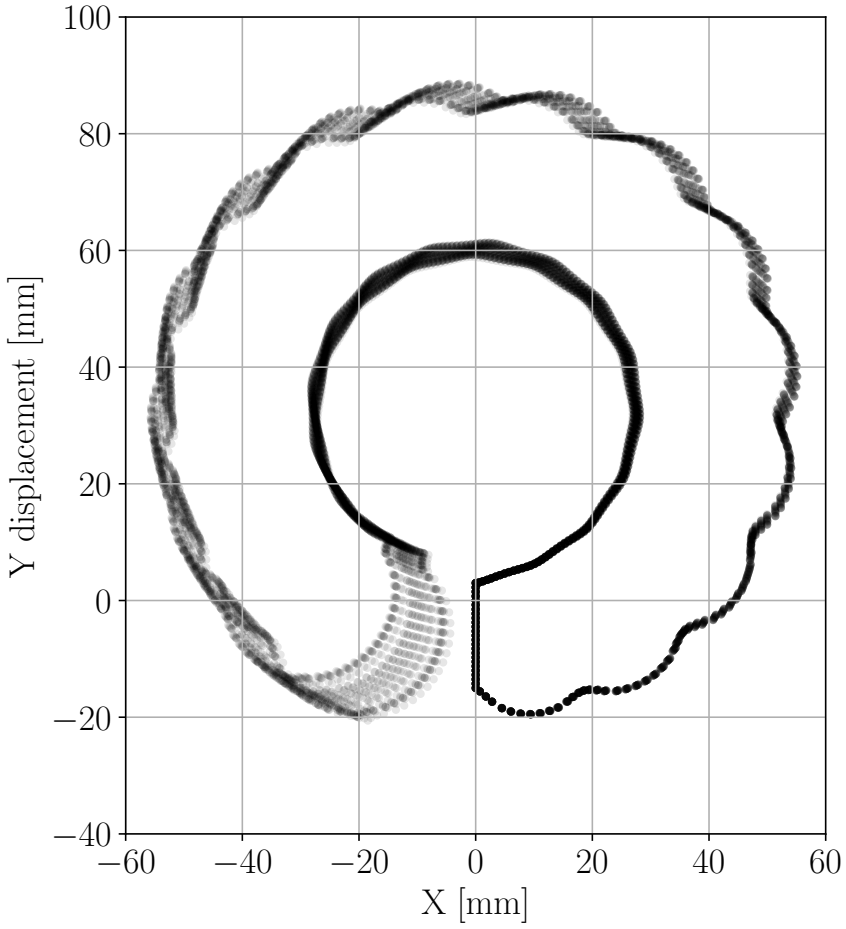

Figure E.6: Sensitivity of numerical model to a manufacturing tolerance of ± 0.02 mm

List of References

Agarwal, G., Besuchet, N., Audergon, B. and Paik, J. (2016). Stretchable Materials for Robust Soft Actuators towards Assistive Wearable Devices. *Scientific Reports*, vol. 6, no. 1, p. 34224. ISSN 2045-2322.

Alici, G., Canty, T., Mutlu, R., Hu, W. and Sencadas, V. (2017). Modeling and Experimental Evaluation of Bending Behavior of Soft Pneumatic Actuators Made of Discrete Actuation Chambers. *Soft Robotics*, vol. 00, no. 00, p. soro.2016.0052. ISSN 2169-5172.

ASTM (). Standard Test Method for Gel Time and Peak Exothermic Temperature of Reacting Thermosetting Resins. Standard, ASTM.

Back, T., Fogel, D.B. and Michalewicz, Z. (2000). *Evolutionary Computation 1 - Basic Algorithms and Operators*. Institute of Physics Publishing. ISBN 0750306645.

Bathe, K. (2014). *Finite Element Procedures - Second Edition*. Prentice Hall Inc, New Jersey.

Bergstrom, J. (2015). Mechanics of solid polymers. William Andrew Publishing. ISBN 978-0-323-31150-2.

Bishop-Moser, J. and Kota, S. (2015). Design and Modeling of Generalized Fiber-Reinforced Pneumatic Soft Actuators. *IEEE Transactions on Robotics*, vol. 31, no. 3, pp. 536–545. ISSN 15523098.

Bohnacker, H., Laub, J. and Gross, B. (2009). *Generative Gestaltung*. 1st Ed. Princeton Architectural Press.

Case, J.C., White, E.L. and Kramer, R.K. (2015). Soft Material Characterization for Robotic Applications. *Soft Robotics*, vol. 2, no. 2, pp. 80–87. ISSN 2169-5172.

Cheney, N., MacCurdy, R., Clune, J. and Lipson, H. (2014). Unshackling evolution. *ACM SIGEVOlution*, vol. 7, no. 1, pp. 11–23. ISSN 19318499.

Ching-Ping Chou and Hannaford, B. (1996). Measurement and modeling of McKibben pneumatic artificial muscles. *IEEE Transactions on Robotics and Automation*, vol. 12, no. 1, pp. 90–102. ISSN 1042296X.

Clune, J. and Lipson, H. (2011). Evolving 3D objects with a generative encoding inspired by developmental biology. *ACM SIGEVOlution*, vol. 5, no. 4, pp. 2–12. ISSN 19318499.

Connolly, F., Polygerinos, P., Walsh, C.J. and Bertoldi, K. (2015). Mechanical Programming of Soft Actuators by Varying Fiber Angle. *Soft Robotics*, vol. 2, no. 1, pp. 26–32. ISSN 2169-5172.

Connolly, F., Walsh, C.J. and Bertoldi, K. (2016). Automatic design of fiber-reinforced soft actuators for trajectory matching. *Proceedings of the National Academy of Sciences*, vol. 114, no. 1, p. 201615140. ISSN 0027-8424.

Cook, A.J. and Walker, S.J. (2016). Experimental research on tape spring supported space inflatable structures. *Acta Astronautica*, vol. 118, pp. 316–328. ISSN 00945765.

De Greef, A., Lambert, P. and Delchambre, A. (2009). Towards flexible medical instruments: Review of flexible fluidic actuators. *Precision Engineering*, vol. 33, no. 4, pp. 311–321. ISSN 01416359.

Deimel, R. and Brock, O. (2013). A compliant hand based on a novel pneumatic actuator. *Proceedings - IEEE International Conference on Robotics and Automation*, pp. 2047–2053. ISSN 10504729.

Doumit, M., Fahim, A. and Munro, M. (2009). Analytical modeling and experimental validation of the braided pneumatic muscle. *IEEE Transactions on Robotics*, vol. 25, no. 6, pp. 1282–1291. ISSN 15523098.

Duriez, C. and Duriez, C. (2013). Control of Elastic Soft Robots based on Real-Time Finite Element Method. pp. 3967–3972.

Ellis, D.R. (2017). *Mechanical characterisation for simplified response modelling of woven polypropylene*. Masters Thesis, Stellenbosch University.

Ellis, D.R., Venter, M.P. and Venter, G. (2018). Bilinear Response in Paper-Silicone Composite Material. In: *Eleventh South African Conference on Computational and Applied Mechanics*, September. Vanderbijlpark.

Ellis, D.R., Venter, M.P. and Venter, G. (2019). Computational Design for Inflated Shape of a Modular Soft Robotic Actuator. *2019 2nd IEEE International Conference on Soft Robotics (RoboSoft)*, pp. 1–6.

Elsayed, Y., Vincensi, A., Lekakou, C., Geng, T., Saaj, C.M., Ranzani, T., Cianchetti, M. and Menciassi, A. (2014). Finite Element Analysis and Design Optimization of a Pneumatically Actuating Silicone Module for Robotic Surgery Applications. *Soft Robotics*, vol. 1, no. 4, pp. 255–262. ISSN 2169-5172.

Faudzi, A.A.M., Razif, M.R.M., Nordin, I.N.A.M., Suzumori, K., Wakimoto, S. and Hirooka, D. (2012). Development of bending soft actuator with different braided angles. *IEEE/ASME International Conference on Advanced Intelligent Mechatronics, AIM*, pp. 1093–1098. ISSN 2159-6247.

Fortin, F.-A., De Rainville, F.-M., Gardner, M.-A., Parizeau, M. and Gagné, C. (2012 jul). DEAP: Evolutionary algorithms made easy. *Journal of Machine Learning Research*, vol. 13, pp. 2171–2175.

Füchslin, R.M., Dzyakanchuk, A., Flumini, D. and Hauser, H. (2013). Morphological computation and morphological control: Steps toward a formal theory and applications. *Artificial Life*, vol. 19, no. 1, pp. 9–34. ISSN 1064-5462.

Galloway, K.C., Polygerinos, P., Walsh, C.J. and Wood, R.J. (2013). Mechanically programmable bend radius for fiber-reinforced soft actuators. *IEEE International Conference on Advanced Robotics*.

Gauci, J. and Stanley, K.O. (2010). Indirect encoding of neural networks for scalable Go. In: *Proceedings of the 11th International Conference on Parallel Problem Solving From Nature*, pp. 354–363. ISBN 3642158439. ISSN 03029743.

Goldberg, D.E. (1989). *Genetic Algorithms in Search, Optimization and Machine Learning*. 1st edn. Addison-Wesley Longman Publishing Co., Inc., Boston, MA, USA. ISBN 0201157675.

Hiller, J. and Lipson, H. (2010). Evolving Amorphous Robots. *Artificial Life XII. Proceedings of the 12th International Conference on the Synthesis and Simulation of Living Systems*, pp. 717–724.

Hiller, J. and Lipson, H. (2012*a*). Automatic Design and Manufacture of Soft Robots. *IEEE Transactions on Robotics*, vol. 28, no. 2, pp. 457–466.

Hiller, J. and Lipson, H. (2012*b*). Dynamic Simulation of Soft Heterogeneous Objects. ISSN 2169-5172.

Iida, F. and Laschi, C. (2011). Soft robotics: Challenges and perspectives. *Procedia Computer Science*, vol. 7, pp. 99–102. ISSN 18770509.

Ilievski, F., Mazzeo, A.D., Shepherd, R.F., Chen, X. and Whitesides, G.M. (2011). Soft robotics for chemists. *Angewandte Chemie - International Edition*, vol. 50, no. 8, pp. 1890–1895. ISSN 14337851.

ISO (2011). ISO 37: Rubber, vulcanized or thermoplastic Determination of tensile stress-strain properties.

ISO (2017). ISO 7743: Rubber, vulcanized or thermoplastic Determination of compression stress-strain properties.

Johnston, I.D., McCluskey, D.K., Tan, C.K. and Tracey, M.C. (2014). Mechanical characterization of bulk Sylgard 184 for microfluidics and microengineering. *Journal of Micromechanics and Microengineering*, vol. 24, no. 3. ISSN 13616439.

Kim, S., Laschi, C. and Trimmer, B. (2013). Soft robotics: A bioinspired evolution in robotics. *Trends in Biotechnology*, vol. 31, no. 5, pp. 287–294. ISSN 01677799.

Kwok, S.W., Morin, S.A., Mosadegh, B., So, J.H., Shepherd, R.F., Martinez, R.V., Smith, B., Simeone, F.C., Stokes, A.A. and Whitesides, G.M. (2014). Magnetic assembly of soft robots with hard components. *Advanced Functional Materials*, vol. 24, no. 15, pp. 2180–2187. ISSN 16163028.

Lampani, L. and Gaudenzi, P. (2010). Numerical simulation of the behavior of inflatable structures for space. *Acta Astronautica*, vol. 67, no. 3-4, pp. 362–368. ISSN 00945765.

Landkammer, S., Winter, F., Schneider, D. and Hornfeck, R. (2016). Biomimetic Spider Leg Joints: A Review from Biomechanical Research to Compliant Robotic Actuators. *Robotics*, vol. 5, no. 3, pp. 1–15. ISSN 2218-6581.

Laschi, C. and Cianchetti, M. (2014). Soft robotics: new perspectives for robot bodyware and control. *Frontiers in Bioengineering and Biotechnology*, vol. 2, no. January, p. 3.

LaVision GmbH (2015). *StrainMaster Advanced Digital Image Correlation Systems for Optical Full Field Measurement of Material Strain, Displacement and Shape.* Göttingen, Germany.

Lecompte, D., Smits, A., Bossuyt, S., Sol, H., Vantomme, J., Van Hemelrijck, D. and Habraken, A.M. (2006). Quality assessment of speckle patterns for digital image correlation. *Optics and Lasers in Engineering*, vol. 44, no. 11, pp. 1132–1145.

Lee, C., Kim, M., Kim, Y.J., Hong, N., Ryu, S., Kim, H.J. and Kim, S. (2017). Soft robot review. *International Journal of Control, Automation and Systems*, vol. 15, no. 1, pp. 3–15. ISSN 20054092.

Liu, W. and Rahn, C.R. (2003). Fiber-Reinforced Membrane Models of McKibben Actuators. *Journal of Applied Mechanics*, vol. 70, no. 6, p. 853. ISSN 00218936.

Majidi, C. (2014). Soft Robotics : A Perspective Current Trends and Prospects for the Future. *Soft Robotics*, vol. 1, no. 1. ISSN 2169-5172.

Manti, M., Cacucciolo, V. and Cianchetti, M. (2016). Stiffening in soft robotics: A review of the state of the art. *IEEE Robotics and Automation Magazine*, vol. 23, no. 3, pp. 93–106. ISSN 10709932.

Marchese, A.D., Katzschmann, R.K. and Rus, D. (2015). A Recipe for Soft Fluidic Elastomer Robots. *Soft Robotics*, vol. 2, no. 1, pp. 7–25. ISSN 2169-5172.

Marchese, A.D., Onal, C.D. and Rus, D. (2014). Autonomous Soft Robotic Fish Capable of Escape Maneuvers Using Fluidic Elastomer Actuators. *Soft Robotics*, vol. 1, no. 1, pp. 75–87. ISSN 2169-5172.

Martinez, R.V., Branch, J.L., Fish, C.R., Jin, L., Shepherd, R.F., Nunes, R.M.D., Suo, Z. and Whitesides, G.M. (2013). Robotic tentacles with three-dimensional mobility based on flexible elastomers. *Advanced Materials*, vol. 25, no. 2, pp. 205–212. ISSN 09359648.

Martinez, R.V., Fish, C.R., Chen, X. and Whitesides, G.M. (2012). Elastomeric origami: Programmable paper-elastomer composites as pneumatic actuators. *Advanced Functional Materials*, vol. 22, no. 7, pp. 1376–1384. ISSN 1616301X.

Memarian, M., Gorbet, R. and Kulic, D. (2015). Modelling and experimental analysis of a novel design for soft pneumatic artificial muscles. *IEEE International Conference on Intelligent Robots and Systems*, pp. 1718–1724.

Meunier, L., Chagnon, G., Favier, D., Orgéas, L. and Vacher, P. (2008). Mechanical experimental characterisation and numerical modelling of an unfilled silicone rubber. *Polymer Testing*, vol. 27, no. 6, pp. 765–777. ISSN 01429418.

Mohd Nordin, I.N.A., Muhammad Razif, M.R., Faudzi, A.A.M., Natarajan, E., Iwata, K. and Suzumori, K. (2013). 3-D finite-element analysis of fiber-reinforced soft bending actuator for finger flexion. *IEEE/ASME International Conference on Advanced Intelligent Mechatronics: Mechatronics for Human Wellbeing*, pp. 128–133. ISSN 2159-6255;978-1-4673-5320-5.

Morin, S.A., Kwok, S.W., Lessing, J., Ting, J., Shepherd, R.F., Stokes, A.A. and Whitesides, G.M. (2014*a*). Elastomeric tiles for the fabrication of inflatable structures. *Advanced Functional Materials*, vol. 24, no. 35, pp. 5541–5549. ISSN 16163028.

Morin, S.A., Shepherd, R.F., Kwok, S.W., Stokes, A.A., Nemiroski, A. and Whitesides, G.M. (2012). Camouflage and Display for Soft Machines. *Science*, vol. 162, no. June, pp. 2–6.

Morin, S.A., Shevchenko, Y., Lessing, J., Kwok, S.W., Shepherd, R.F., Stokes, A.A. and Whitesides, G.M. (2014*b*). Using "click-e-Bricks" to Make 3D Elastomeric Structures. *Advanced Materials*, vol. 26, no. 34, pp. 5991–5999. ISSN 15214095.

Mosadegh, B., Polygerinos, P., Keplinger, C., Wennstedt, S., Shepherd, R.F., Gupta, U., Shim, J., Bertoldi, K., Walsh, C.J. and Whitesides, G.M. (2014). Pneumatic networks for soft robotics that actuate rapidly. *Advanced Functional Materials*, vol. 24, no. 15, pp. 2163–2170.

Moseley, P., Florez, J.M., Sonar, H.A., Agarwal, G., Curtin, W. and Paik, J. (2016). Modeling, Design, and Development of Soft Pneumatic Actuators with Finite Element Method. *Advanced Engineering Materials*, vol. 18, no. 6, pp. 978–988. ISSN 15272648.

MSC.Marc (2018*a*). *Marc 2018.0 - Volume A: Theory and User Information*. MSC Software Corporation.

MSC.Marc (2018*b*). *Marc 2018.0 - Volume B: Element Library*. MSC Software Corporation.

MSC.Marc (2018*c*). *Marc and Mentat 2018.0 - Release Guide*. MSC Software Corporation.

Mullins, L. (1969). Softening of rubber by deformation. *Rubber Chemistry and Technology*, vol. 42, no. 1, pp. 339–362.

Nishioka, Y., Uesu, M., Tsuboi, H. and Kawamura, S. (2012). Proposal of an extremely lightweight soft actuator using plastic films with a pleated structure. In: *International Conference on Mechatronics and Machine Vision in Practice*, pp. 474–479. University Auckland,New-Zealand, Aukland, New-Zealand Proposal. ISBN 9780473204853.

Ogden, R., Saccomandi, G. and Sgura, I. (2004). Fitting hyperelastic models to experimental data. *Computational Mechanics*, vol. 34, no. 6, pp. 484–502.

Ogden, R.W. (1972). Large Deformation Isotropic Elasticity-On the Correlation of Theory and Experiment for Incompressible Rubberlike Solids. *Proceedings of the Royal Society of London. A. Mathematical and Physical Sciences*, vol. 326, pp. 565–584. ISSN 1364-5021.

Onal, C.D., Chen, X., Whitesides, G.M. and Rus, D. (2011). Soft mobile robots with on-board chemical pressure generation. *International Symposium on Robotics Research*.

Onal, C.D. and Rus, D. (2012). A modular approach to soft robots. *Proceedings of the IEEE RAS and EMBS International Conference on Biomedical Robotics and Biomechatronics*, pp. 1038–1045. ISSN 21551774.

Overvelde, J.T.B., Kloek, T., D'haen, J.J.A. and Bertoldi, K. (2015). Amplifying the response of soft actuators by harnessing snap-through instabilities. *Proceedings of the National Academy of Sciences of the United States of America*, vol. 112, no. 35, pp. 10863–8. ISSN 1091-6490.

Paek, J., Cho, I. and Kim, J. (2015). Microrobotic tentacles with spiral bending capability based on shape-engineered elastomeric microtubes. *Scientific Reports*, vol. 5, no. March, p. 10768. ISSN 2045-2322.

Paez, L., Agarwal, G. and Paik, J. (2016). Design and Analysis of a Soft Pneumatic Actuator with Origami Shell Reinforcement. *Soft Robotics*, vol. 3, no. 3, pp. 109–119. ISSN 2169-5172.

Polygerinos, P., Lyne, S., Wang, Z., Nicolini, L.F., Mosadegh, B., Whitesides, G.M. and Walsh, C.J. (2013). Towards a soft pneumatic glove for hand rehabilitation. *IEEE International Conference on Intelligent Robots and Systems*, pp. 1512–1517. ISSN 21530858.

Polygerinos, P., Wang, Z., Overvelde, J.T.B., Galloway, K.C., Wood, R.J., Bertoldi, K. and Walsh, C.J. (2015). Modeling of Soft Fiber-Reinforced Bending Actuators. *IEEE Transactions on Robotics*, vol. 31, no. 3, pp. 778–789. ISSN 15523098.

Redwood, B. (2019). Dimensional accuracy of 3d printed parts. https://www.3dhubs.com/knowledge-base/dimensional-accuracy-3d-printed-parts. Accessed: 2019-07-14.

Rey, T., Chagnon, G., Cam, J.-b.L., Favier, D., Rey, T., Chagnon, G., Cam, J.-b.L., Favier, D., Rey, T., Chagnon, G., Cam, J.B.L. and Favier, D. (2014). Effects of temperature on the mechanical behavior of filled and unfilled silicone rubbers. *Polymer Testing*, vol. 32, no. 3, pp. 492 – 501.

Rieffel, J., Knox, D. and Smith, S. (2014). Growing and Evolving Soft Robots. *Artificial Life*, vol. 162, no. 20, pp. 143–162.

Rieffel, J., Saunders, F., Nadimpalli, S., Zhou, H., Hassoun, S., Rife, J. and Trimmer, B. (2009). Evolving soft robotic locomotion in PhysX. *Proceedings of the 11th annual conference companion on Genetic and evolutionary computation conference - GECCO '09*, vol. 11, no. June 2017, p. 2499.

Rivlin, R. and Saunders, D. (1951). Large Elastic Deformations of Isotropic Materials . VII . Experiments on the Deformation of Rubber. *Philosophical Transactions of the Royal Society of London*, vol. 243, no. 865, pp. 251–288.

Roche, E.T., Wohlfarth, R., Overvelde, J.T.B., Vasilyev, N.V., Pigula, F.A., Mooney, D.J., Bertoldi, K. and Walsh, C.J. (2014). A bioinspired soft actuated material. *Advanced Materials*, vol. 26, no. 8, pp. 1200–1206. ISSN 09359648.

Rus, D. and Tolley, M.T. (2015). Design, fabrication and control of soft robots. *Nature*, vol. 521, no. 7553, pp. 467–475. ISSN 0028-0836.

Seals Unlimited (2019). Decoding basic rubber hardness and durometer scales. https://www.sealsunlimited.com/seals.nsf/weblinks/AHBD-AA23P8?open. Accessed: 2019-06-12.

Shen, H. (2016). Meet the soft, cuddly robots of the future. *Nature*, vol. 530, no. 7588, pp. 24–26. ISSN 0028-0836.

Shepherd, R.F., Ilievski, F., Choi, W., Morin, S.A., Stokes, A.A., Mazzeo, A.D., Chen, X., Wang, M. and Whitesides, G.M. (2011). Multigait soft robot. *Proceedings of the National Academy of Sciences*, vol. 108, no. 51, pp. 20400–20403. ISSN 0027-8424.

Shepherd, R.F., Stokes, A.A., Freake, J., Barber, J., Snyder, P.W., Mazzeo, A.D., Cademartiri, L., Morin, S.A. and Whitesides, G.M. (2013). Using explosions to power a soft robot. *Angewandte Chemie - International Edition*, vol. 52, no. 10, pp. 2892–2896. ISSN 14337851.

Shintake, J., Rosset, S., Schubert, B., Floreano, D. and Shea, H. (2016). Versatile Soft Grippers with Intrinsic Electroadhesion Based on Multifunctional Polymer Actuators. *Advanced Materials*, vol. 28, no. 2, pp. 231–238. ISSN 15214095.

Siemens NX12 (2017). *NX Nastran 12 - Quick Refence Guide*. Siemens Product Lifecycle Management Software Inc.

Singh, G. and Krishnan, G. (2015). An isoperimetric formulation to predict deformation behavior of pneumatic fiber reinforced elastomeric actuators. In: *IEEE International Conference on Intelligent Robots and Systems*, pp. 1738–1743. ISBN 9781479999941. ISSN 21530866.

Slo-Jo (2019). Smooth-On. Brochure.
Available at: https://www.smooth-on.com/tb/files/SLO-JO_TB.pdf

Smooth-On (2019). Mold Making and Casting Materials. Website. Accessed: 2017-04-01.
Available at: https://www.smooth-on.com/

Sun, Y., Song, Y.S. and Paik, J. (2013). Characterization of silicone rubber based soft pneumatic actuators. *IEEE International Conference on Intelligent Robots and Systems*, pp. 4446–4453. ISSN 21530858.

Suzumori, K., Endo, S., Kanda, T., Kato, N. and Suzuki, H. (2007). A bending pneumatic rubber actuator realizing soft-bodied manta swimming robot. *IEEE International Conference on Robotics and Automation*, vol. 7, no. April, pp. 4975–4980. ISSN 10504729.

Tolley, M.T., Shepherd, R.F., Mosadegh, B., Galloway, K.C., Wehner, M., Karpelson, M., Wood, R.J. and Whitesides, G.M. (2014*a*). A Resilient, Untethered Soft Robot. *Soft Robotics*, vol. 1, no. 3, pp. 213–223. ISSN 2169-5172.

Tolley, M.T., Shepherd, R.F., Mosadegh, B., Galloway, K.C., Wehner, M., Karpelson, M., Wood, R.J. and Whitesides, G.M. (2014*b*). A Resilient, Untethered Soft Robot. *Soft Robotics*, vol. 1, no. 3, pp. 213–223. ISSN 2169-5172.

Trivedi, D., Rahn, C.D., Kier, W.M. and Walker, I.D. (2008). Soft robotics: Biological inspiration, state of the art, and future research. *Applied Bionics and Biomechanics*, vol. 5, no. 3, pp. 99–117. ISSN 1176-2322.

Vanderplaats Research &, Development Inc (). *DOT Users manual* .

Wakimoto, S., Suzumori, K. and Ogura, K. (2011). Miniature Pneumatic Curling Rubber Actuator Generating Bidirectional Motion with One Air-Supply Tube. *Advanced Robotics*, vol. 25, no. 9-10, pp. 1311–1330. ISSN 0169-1864.

Wang, Z., Chen, M.Z.Q. and Yi, J. (2015). Soft robotics for engineers. *HKIE Transactions*, vol. 22, no. 2, pp. 88–97. ISSN 1023-697X.

Yang, D., Mosadegh, B., Ainla, A., Lee, B., Khashai, F., Suo, Z., Bertoldi, K. and Whitesides, G.M. (2015). Buckling of Elastomeric Beams Enables Actuation of Soft Machines. *Advanced Materials*, vol. 27, no. 41, pp. 6323–6327. ISSN 15214095.

Yang, D., Verma, M.S., So, J.-H., Mosadegh, B., Keplinger, C., Lee, B., Khashai, F., Lossner, E., Suo, Z. and Whitesides, G.M. (2016). Buckling Pneumatic Linear Actuators Inspired by Muscle. *Advanced Materials Technologies*, vol. 1, no. 3, p. 1600055. ISSN 2365709X.

Yap, H.K., Lim, J.H., Nasrallah, F., Goh, J.C. and Yeow, R.C. (2015). A soft exoskeleton for hand assistive and rehabilitation application using pneumatic actuators with variable stiffness. *Proceedings - IEEE International Conference on Robotics and Automation*, , no. June, pp. 4967–4972. ISSN 10504729.

Yeoh, O.H. (1993). Some forms of the strain energy function for rubber. *Rubber Chemistry and technology*, vol. 66, no. 5, pp. 754–771.